



Terms and Conditions of Use of Digitised Theses from Trinity College Library Dublin

Copyright statement

All material supplied by Trinity College Library is protected by copyright (under the Copyright and Related Rights Act, 2000 as amended) and other relevant Intellectual Property Rights. By accessing and using a Digitised Thesis from Trinity College Library you acknowledge that all Intellectual Property Rights in any Works supplied are the sole and exclusive property of the copyright and/or other IPR holder. Specific copyright holders may not be explicitly identified. Use of materials from other sources within a thesis should not be construed as a claim over them.

A non-exclusive, non-transferable licence is hereby granted to those using or reproducing, in whole or in part, the material for valid purposes, providing the copyright owners are acknowledged using the normal conventions. Where specific permission to use material is required, this is identified and such permission must be sought from the copyright holder or agency cited.

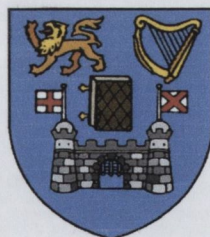
Liability statement

By using a Digitised Thesis, I accept that Trinity College Dublin bears no legal responsibility for the accuracy, legality or comprehensiveness of materials contained within the thesis, and that Trinity College Dublin accepts no liability for indirect, consequential, or incidental, damages or losses arising from use of the thesis for whatever reason. Information located in a thesis may be subject to specific use constraints, details of which may not be explicitly described. It is the responsibility of potential and actual users to be aware of such constraints and to abide by them. By making use of material from a digitised thesis, you accept these copyright and disclaimer provisions. Where it is brought to the attention of Trinity College Library that there may be a breach of copyright or other restraint, it is the policy to withdraw or take down access to a thesis while the issue is being resolved.

Access Agreement

By using a Digitised Thesis from Trinity College Library you are bound by the following Terms & Conditions. Please read them carefully.

I have read and I understand the following statement: All material supplied via a Digitised Thesis from Trinity College Library is protected by copyright and other intellectual property rights, and duplication or sale of all or part of any of a thesis is not permitted, except that material may be duplicated by you for your research use or for educational purposes in electronic or print form providing the copyright owners are acknowledged using the normal conventions. You must obtain permission for any other use. Electronic or print copies may not be offered, whether for sale or otherwise to anyone. This copy has been supplied on the understanding that it is copyright material and that no quotation from the thesis may be published without proper acknowledgement.



Synthesis and Properties of a Novel Carbon Nanotube-Polymer Thin Film Composite

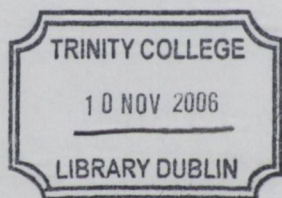
By

Emer Lahiff

A thesis submitted for the degree of
Doctor of Philosophy

Department of Physics,
Trinity College Dublin.

2006



THESIS

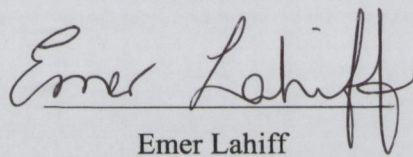
7984

Declaration

I declare that the work in this thesis has not been previously submitted as an exercise for a degree to this or any other university.

The work described herein is entirely my own, except for the assistance mentioned in the acknowledgements and the collaborative work mentioned in the list of publications.

I agree that Trinity College Library may lend or copy this thesis on request.


Emer Lahiff

Abstract

A novel method for carbon nanotube-polymer composite production is demonstrated in this thesis. The technique presented provides a way in which the position of nanotubes within a polymer matrix can be controlled. By controlling the position of nanotubes, we have a method of pre-determining the location of conduction channels through an insulating system. We can also avoid the need for nanotube dispersion and purification prior to composite formation.

To achieve this, we grow carbon nanotubes onto a substrate by chemical vapour deposition. Nanotube growth is activated by a catalyst material. By selectively patterning a catalyst onto a substrate we can control the position of nanotube arrays. We use soft lithography to deposit catalyst patterns. Soft lithography is a convenient, inexpensive process which can be done under atmospheric conditions. This contributes towards the efficiency of nanotube production. Manipulation of the patterning and CVD conditions enables control over properties such as tube diameter, alignment and density. There is relatively little amorphous carbon deposition during the process.

As-grown carbon nanotubes can be directly incorporated from substrates into a polymer matrix. A curable polymer is spin coated onto nanotube arrays. The viscous mixture intercalates between nanotubes. After curing, the composite can be peeled from the substrate. Nanotubes remain embedded in the polymer and detach easily from the substrate.

To demonstrate the technique, we used a silicone elastomer (Sylgard 184) matrix. We were able to produce freestanding flexible thin film composites. The thickness of the film could be controlled by varying the spin speed. The properties of the composite were characterised and it was observed that adding nanotubes transformed the insulating matrix into a conducting polymer. Surface conductivity increased by six orders of magnitude (10^6) and bulk conductivity increased by an impressive eight orders of magnitude (10^8). Mechanical enhancement was not quite so dramatic. We measured a Young's modulus increase by a factor of 2.1 ± 0.9 . However, we observed

no increase in strength. We attribute this to poor interfacial bonding between the nanotubes and the polymer matrix. This was supported by differential scanning calorimetry. Further research could be used to refine this process into a simple, controllable and economical technique of composite fabrication.

Acknowledgements

Most importantly I would like to thank Prof. Werner Blau who gave me the opportunity to study for a PhD. He has provided the necessary financial support and also ample opportunities for travel to both conferences and other research groups.

I would also like to thank Prof. Pulickel Ajayan for giving me the opportunity to spend the first fifteen months of my studies in Rensselaer Polytechnic Institute, New York. During my time in New York I was co-supervised by Prof. Chang Ryu who provided some invaluable chemistry knowledge. From his research group I would particularly like to thank Won Kim and Dr. Hyunsoo Chung for their help with GPC and NMR. I would also like to acknowledge Dr. Seamus Curran who helped focus my research.

I would like to thank Dr. Siegmur Roth for giving me the chance to visit the Max-Planck-Institute for Solid State Research, Stuttgart. Within Dr. Roth's group Martii Kaempgen was particularly helpful. Other helpful collaborators include Dr. Georg Duesberg (Infineon Technologies) and AunShih Teh (Prof. Bill Milne's research group, Cambridge University).

From within Trinity College, I would especially like to thank Dr. Jonathan Coleman for his help in answering queries that I have had along the way. I would also like to thank Rory Leahy for constructing the CVD system. I would like to thank Dr. Leslie Carpenter for all his useful advice and for correcting the first draft of my thesis. I would like to thank Dr. Andrew Minett, Dr. Manuel Ruether, Ronan Hodson, Adam Strevens and Yenny Hernandez for all their help. I would like to thank Dr. Kentaro Nakajima and Emma Kerr for their assistance with photolithography. I would like to thank everyone in the Centre for Microscopy Analysis (Trinity College), especially Neal, Mick and Dave from the workshop deserve a thank you for making and adapting parts for the CVD system. Also, John, Jemmer, Ken and Jeanette for all the administrative support they provide.

Table of Contents

Declaration.....	ii
Abstract.....	iii
Acknowledgements.....	v
Table of Contents.....	vi
List of Tables.....	x
List of Figures and Illustrations.....	xi

CHAPTER 1: INTRODUCTION

1.1 Background and Motivation.....	1
1.2 Carbon Nanotubes.....	3
1.3 Limiting Factors.....	3
1.4 Thesis Outline.....	5
1.5 References.....	7

CHAPTER 2: CARBON NANOTUBES AS A FILLER FOR POLYMER SYSTEMS

2.1 Polymers.....	8
2.1.1 Conductivity in Polymers.....	9
2.2 Conductive Fillers.....	10
2.3 Carbon Nanotubes: The Ideal Filler.....	12
2.3.1 Allotropes of Carbon.....	12
2.3.1.1 Fullerenes.....	13
2.3.2 Structure of CNTs.....	14
2.3.3 Electrical Properties of CNTs.....	15
2.3.4 Mechanical Properties of CNTs.....	17
2.3.5 Applications of CNTs.....	19
2.4 Carbon Nanotube Growth.....	20
2.4.1 Catalyst.....	26
2.4.2 Growth Mechanism.....	28
2.4.3 Catalyst Patterning.....	31
2.4.3.1 Soft Lithography.....	33
2.4.3.2 Soft Lithography Patterning for CNT Growth.....	34
2.5 Carbon Nanotube Composites.....	35
2.5.1 CNT Composite Production Mechanisms.....	36

2.5.2	CNT Functionalisation.....	39
2.5.3	Composite Properties.....	40
2.5.3.1	Mechanical Properties.....	40
2.5.3.2	Electrical Properties.....	42
2.5.4	Commercial Applications for CNT Composites.....	43
2.6	References.....	46

CHAPTER 3: SYNTHESIS OF A NOVEL CATALYST FOR THE GROWTH OF CARBON NANOTUBES

3.1	Introduction.....	53
3.2	Catalyst Synthesis.....	53
3.2.1	Styrene Purification.....	55
3.2.2	Vinylferrocene Purification.....	55
3.2.3	Tetrahydrofuran Purification.....	56
3.2.4	Polymerisation.....	56
3.2.5	Amount of Initiator Required.....	57
3.3	Catalyst Characterisation.....	58
3.3.1	Gel Permeation Chromatography.....	58
3.3.1.1	Catalyst Characterisation by GPC.....	59
3.3.1.2	Calculation of the Copolymer Blend Composition.....	60
3.3.2	Nuclear Magnetic Resonance.....	62
3.3.2.1	Catalyst Characterisation by NMR.....	65
3.3.2.2	Calculation of Styrene-to-Vinylferrocene Ratio.....	67
3.3.3	Thermal Gravimetric Analysis.....	68
3.3.3.1	Thermal Analysis of Synthesised Copolymer.....	69
3.3.4	Raman Spectroscopy.....	70
3.3.4.1	Raman Spectroscopy of Synthesised Copolymer.....	72
3.4	Conclusion.....	75
3.5	References.....	76

CHAPTER 4: CATALYST PATTERNING BY SOFT LITHOGRAPHY

4.1	Introduction.....	77
4.2	Generating a Master Template.....	77
4.2.1	Mask Design.....	77

4.2.2	Transferring the Pattern onto a Silicon Wafer.....	79
4.2.2.1	Etching the Master.....	79
4.2.3	Release Promoter.....	82
4.3	Casting stamps.....	84
4.3.1	Interferometry of Stamps and Masters.....	85
4.4	Patterning Substrates for Carbon Nanotube Growth.....	86
4.4.1	Images of Catalyst Micro-Patterns.....	87
4.4.2	Energy Dispersive X-Ray Spectroscopy.....	89
4.4.2.1	EDXS to Confirm the Presence of Iron at High Temperatures.....	91
4.5	Conclusion.....	92
4.6	References.....	93

CHAPTER 5: THE PRODUCTION OF NANOTUBE ARRAYS

5.1	Introduction.....	94
5.2	Chemical Vapour Deposition System.....	94
5.3	Process Optimisation.....	96
5.4	Carbon Nanotube Growth on Grid Patterns.....	101
5.5	Nanotube Growth using other CVD systems.....	105
5.6	Problems with Producing Large-Scale Arrays.....	110
5.7	Conclusions.....	112
5.8	References.....	113

CHAPTER 6: INCORPORATION OF NANOTUBE ARRAYS INTO A COMPOSITE

6.1	Introduction.....	115
6.2	The Silicone Elastomer Matrix.....	115
6.3	Composite Fabrication.....	116
6.3.1	Composite Thickness.....	117
6.4	The Composite Surface.....	118
6.4.1	Atomic Force Microscopy.....	118
6.4.2	Probing the Composite Surface.....	120
6.5	The Nanotube-Polymer Interface.....	122
6.6	Macroscopic Composite Images.....	124
6.7	Conclusions.....	125

6.8	References.....	126
-----	-----------------	-----

CHAPTER 7: PHYSICAL CHARACTERISATION OF COMPOSITES

7.1	Introduction.....	127
7.2	Composites Tested.....	127
7.3	Electrical Conductivity.....	130
7.4	Mechanical Reinforcement.....	141
7.5	Differential Scanning Calorimetry.....	146
7.5.1	DSC Analysis.....	147
7.6	Thermal Gravimetric Analysis.....	148
7.7	Conclusions.....	151
7.8	References.....	152

CHAPTER 8: CONCLUSIONS AND FUTURE WORK

8.1	Conclusions.....	153
8.2	Future Work.....	156
8.3	References.....	158

Appendix A:	Eulers Theorem.....	159
Appendix B:	Reference Raman Spectra.....	160
Appendix C:	Publications and Patent	161

List of Tables

Table 3.1: Composition of the synthesised copolymer blend.....	61
Table 4.1: Dimensions of grid patterns.....	78
Table 7.1: Table 1: Values of t , A , s and l used to convert conductance measurements to conductivity.....	136

List of Figures and Illustrations

Figure 2.1: A double bond consists of a σ -bond and a π -bond.....	10
Figure 2.2: The percolation threshold is determined by the geometry of the filler particles. The L/D numbers refer to the length-to-diameter (aspect) ratio.....	11
Figure 2.3: A carbon atom has the electron configuration $1s^2, 2s^2, 2p^2$. There are four valence electrons in the outer shell.....	12
Figure 2.4: Allotropes of carbon include graphite, diamond and fullerenes. Fullerenes exist both as Buckyballs and carbon nanotubes.....	13
Figure 2.5: The structure of a Buckminsterfullerene can be obtained by truncating an icosahedron.....	14
Figure 2.6: A single-walled carbon nanotube can be visualised as a rolled-up sheet of graphite capped by half a C_{60} molecule.....	15
Figure 2.7: Nanotubes possess an armchair, zig-zag or chiral structure depending on n , m and θ	16
Figure 2.8: The two leading theories on the mechanisms of carbon nanotube growth are the root- and tip-growth models.....	29
Figure 2.9: Schematic of how photolithography can be used to pattern a metal layer on silicon.....	31
Figure 3.1: A styrene monomer and a vinylferrocene monomer. These are the building blocks from which PS-PVF is made. The ferrocene component contains an iron core and can thus catalyse carbon nanotube growth.....	53
Figure 3.2: A styrene monomer reacts with sec-butyllithium initiator to form carbanions (δ^-) and metal gegenions (δ^+). This is the initiation stage of the anionic polymerisation reaction.....	54
Figure 3.3: Reaction scheme for the anionic synthesis of the copolymer poly(styrene-vinylferrocene). Monomers are first purified. They are then polymerised in THF using sec-butyllithium as the initiator.....	55
Figure 3.4: Vinylferrocene was added to the styrene carbanions to form the copolymer structure above.....	56
Figure 3.5: GPC spectrum of the synthesised PS-PVF copolymer	60
Figure 3.6: A NMR spectrum of poly(styrene-vinylferrocene)	66

Figure 3.7: The styrene molecule. Each hydrogen atom, numbered 1 to 4, is in a different environment. Hydrogen atoms in an identical environment are labelled with the same number.....	67
Figure 3.8: TGA curve for poly(styrene-vinylferrocene) copolymer blend compared with a curve for polystyrene homopolymer.....	69
Figure 3.9: Comparison of remaining PS homopolymer and PS-PVF copolymer at high temperatures.....	70
Figure 3.10: Energy level diagram for Raman scattering; (a) Stokes Raman scattering (b) anti-Stokes Raman scattering.....	71
Figure 3.11: Raman spectrum of poly(styrene-vinylferrocene) superimposed on a spectrum of polystyrene homopolymer. The intensities of the spectra were adjusted for comparative purposes.....	74
Figure 3.12: Closer inspection highlights differences between the two spectra.....	75
Figure 4.1: Grid patterns of width (d) and separation (L). The red outline represents the area enclosed by $(L+d)^2$	78
Figure 4.2: The etch rate can be controlled by varying RIE conditions. Etch depths were taken as the average measured from electron microscopy images.....	80
Figure 4.3: FESEM image of a grid pattern transferred onto a silicon master by photolithography. Lines are $5\mu\text{m}$ wide and separated by $10\mu\text{m}$ (A). Interferometry reveals the etch depth of the spacings between grids to be 590nm (B).....	81
Figure 4.4: FESEM image of a roughened surface produced when an O_2 plasma is used to remove post-RIE photoresist (A). The surface is much smoother if a H_2SO_4 : H_2O_2 mixture is used (B).....	81
Figure 4.5: The presence of O_2 in the plasma etch causes over-exposure of the silicon.....	82
Figure 4.6: The presence of $-\text{OH}$ surface groups causes silicon to be hydrophilic. Sylgard 184 forms an irreversible seal with the surface due to the formation of covalent bonds during curing.....	83
Figure 4.7: The contact angle (θ) of the silicon master increases after treatment with a release promoter. Measurements show no degradation of the release layer over 40 days. The image on the right shows θ to be the angle between the tangent to the droplet and the substrate surface.....	84

Figure 4.8: Interferometry images from a silicon master patterned with 2 μm gridlines separated by 10 μm hollows.....	85
Figure 4.9: Interferometry images of a stamp, cast from the above silicon master, with 2 μm hollows separated by 10 μm wide plateaus.....	86
Figure 4.10: Interferometry of an untreated hydrophilic silicon master after casting Sylgard 184. The elastomer does not release from the master and remains bonded to the surface.....	86
Figure 4.11: A diagram of the five-step process used to pattern a catalyst solution (orange) onto silicon oxide (purple). Here the patterning of parallel lines is illustrated.....	87
Figure 4.12: Silicon oxide substrates patterned by soft lithography. Catalyst particles are present within the patterns (darker regions) and absent elsewhere.....	88
Figure 4.13: The polymer catalyst patterned into gridlines 5 μm wide. Spacings are incremental from 10 μm , to 25 μm and 50 μm (left-to-right).....	89
Figure 4.14: EDXS line plot taken from an area within the boundaries of a gridline. Due to the small amount of iron present, the plot is easier to read as a log plot (inset).....	90
Figure 4.15: EDXS log plot taken from an area between gridlines. The spectrum verifies the presence of carbon, oxygen, silicon and the absence of iron.....	91
Figure 5.1: A photograph of the CVD system used for CNT growth (the apparatus was designed and assembled by Rory Leahy). The most important components are labelled from 1-7.....	95
Figure 5.2: A brass fitting is used to connect the quart tube to a stainless steel flange attached to the CVD system.....	95
Figure 5.3: Micro-patterned substrates for NT growth. Darker areas correspond to regions of high catalyst concentration and paler areas represent the silicon oxide substrate (A-C). After CVD, carbon nanotube growth occurred only on the micro-patterned areas of the substrate (D-F).....	97
Figure 5.4: The density of tube growth increases with catalyst concentration. Image A shows CNTs grown using 1wt% PS-PVF in toluene. Image B shows CNTs grown using 2wt% solution.....	99

Figure 5.5: Nanotube growth was more homogeneous when a poly(styrene-vinylferrocene) copolymer (A) was used instead of a poly(vinylferrocene) homopolymer (B). Insets show magnified images of the CNT arrays.....99

Figure 5.6: Nanotube diameter increases with temperature. At 700°C, average diameters are 20nm (A). At 800°C average diameters are 70nm (B). These values exclude the thickness of the gold coating. The diameter distribution is uniform at both temperatures.....100

Figure 5.7: After 30 minutes deposition time, an amorphous layer was observed to form over the surface of CNTs (A). A close-up side-profile shows CNTs formed under the amorphous layer (B).....101

Figure 5.8: Amorphous carbon deposits form where the acetylene partial pressure is too high.....101

Figure 5.9: Catalyst micro-patterns generated by soft lithography patterning (A and B). The width of the gridlines is 5µm and spacings are 50µm and 10µm. After CVD, CNTs were observed to grow selectively on the grid lines (C and D).....103

Figure 5.10: CNTs grown on grid patterns with 50µm (A-C) and 10µm (D-F) spacings. Magnification of the arrays shows the random entanglement of tubes within the dimensions of the patterns.....104

Figure 5.11: Average diameters for the MWNTs produced are 20 nm (not including the gold coating).....104

Figure 5.12: Aligned CNTs can be produced by drop casting the catalyst solution onto a silicon oxide template. These images were produced by flowing acetylene (200 sccm) for 20min.....105

Figure 5.13: CNTs grown from a 90 seconds burst of acetylene gas at at 750°C. MWNTs grow selectively on catalyst patterned areas of the substrate. FESEM images increase in magnification from left to right.....106

Figure 5.14: CNTs grown from on a PS-PVF patterned substrate at Infineon Technologies. CVD is done at 700°C using H₂/C₂H₂.....107

Figure 5.15: CNT arrays grown at the Max Planck Institute. Grids shown here have a 5µm separation. Figure A shows CNT arrays over an area ~4mm². This image is magnified in B. Figure C shows CNTs produced by 5 minutes ammonia pre-treatment followed by 2 minutes of acetylene. Figure D, shows results for 10 minutes of ammonia followed by 10 minutes acetylene.....108

Figure 5.16: Pattern edges become rounded as dimensions are reduced. Grid spacings are reduced from 10 to 5 μm (left to right). Images were taken using the SEM at the Max Planck Institute.....	109
Figure 5.17: CNTs grown on line and dot patterns	109.
Figure 5.18: Using a ferrocene/ xylene mixture (typically 10% ferrocene) excellent CNT alignment was achieved. The tubes grow on silicon oxide in preference to silicon. Magnification of FESEM images increases from left to right.....	110
Figure 5.19: The growth of patterned nanotubes arrays is not uniform over the entire substrate surface (A). Within patterned areas sometimes defects occur (B).....	111
Figure 5.20: Pattern defects can be caused by sagging between the pillars of an elastomer stamp (A). Discontinuities can also occur within the dimensions of the patterns (B).....	111
Figure 6.1: Silicone polymers consist of a silicon-oxygen backbone, as shown on the left. The structure of poly(dimethylsiloxane) is shown on the right.....	115
Figure 6.2: FESEM image of nanotubes grown on a SiO ₂ substrate (A). Tubes are subsequently integrated into a polymer matrix to produce nanotube-containing channels separated by pure Sylgard 184 (B). Schematic of a thin film composite with nanotubes lines 5 μm wide incorporated into a composite ~100 μm thick (C).....	117
Figure 6.3: Elastomer film thickness increases as spin speed decreases. These values were measured using a travelling microscope.....	118
Figure 6.4: Schematic of an AFM set-up.....	119
Figure 6.5: An AFM scan shows nanotubes protruding from the composite surface (A). An EFM scan across the same area shows the positions of conduction channels (B).....	121
Figure 6.6: An AFM scan taken across a polymer section of the composite (A). An EFM scan over the same area shows very few conduction channels (B).....	122
Figure 6.7: A FESEM image of nanotubes embedded within the elastomer matrix (A). Only the very tips of the tubes emerge from the surface. Figure B shows two protruding nanotubes covered in polymer this indicates good wetting.....	123
Figure 6.8: FESEM images of torn composite films show that nanotubes remain coated in polymer.....	123

Figure 6.9: Controlled nanotube arrays (A) are embedded in an elastomer thin film (B). This produces a flexible composite (C).....124

Figure 7.1: A PS-PVF catalyst layer is deposited by spin coating. The film thickness changes dramatically as the concentration of the catalyst solution is increased. The spin speed has less effect on film thickness.....128

Figure 7.2: FESEM image of entangled NTs grown from a catalyst thin film spin cast onto a silicon oxide substrate. The inset shows a free standing composite film containing a similar CNT network embedded in Sylgard 184.....129

Figure 7.3: Diagram of the two-point probe set-up. V represents the voltmeter and A is the ammeter. This set-up is only suitable for samples which have a resistance much greater than the contact resistance, R_1 plus R_2130

Figure 7.4: A schematic of gold contacts evaporated onto a composite thin film (in black). The bulk conductivity of the sample can be measured by connecting one wire to the base electrode and a second wire to one of the top electrodes. Surface conductivity can also be measured by connecting wires across any two adjacent top electrodes.....132

Figure 7.5: A typical series of I-V plots obtained across the bulk of a composite thin film. The slope of the linear region of the graph gives a bulk conductance of 2.7×10^{-5} S. Conductance values are stable over seven measurements as the voltage range is gradually expanded to between -20 and 20V.....134

Figure 7.6: A typical series of I-V plots obtained across the surface of a composite thin film. Surface conductance is 3.7×10^{-6} S and is stable over ten measurements as the voltage range is expanded to between -60 and 60V.....134

Figure 7.7: The surface conductivity is measured using an I-V plot obtained by connecting two adjacent surface electrodes. It is assumed that electrons follow path 1. However, the sample thickness is of the same order of the electrode separation and the possibility that electrons follow path 2 has to be considered.....137

Figure 7.8: Conductance values are stable for a minimum of eleven measurements.....138

Figure 7.9: I-V plot obtained between two surface electrodes for a Sylgard 184 thin film sample. Prior to smoothing, the plot showed a lot of noise peaks.....138

Figure 7.10: I-V plot obtained across the bulk of a Sylgard 184 thin film sample. Prior to smoothing the plot showed a lot of noise peaks.....139

Figure 7.11: The average surface conductivity for a Sylgard 184 thin film was measured over three samples.....	139
Figure 7.12: The average bulk conductivity for a Sylgard 184 thin film was measured over three samples.....	140
Figure 7.13: A comparison of σ - ϵ curves obtained for Sylgard 184 versus a composite. The Young's modulus is seen to increase as nanotubes are incorporated into the elastomer matrix. The increase shown here is from 188 kPa to 369 kPa...	142
Figure 7.14: Young's modulus values were calculated for a number of samples to obtain an average. Error bars reflect fluctuations in cross-section area measurements.....	143
Figure 7.15: Average elongation at break measured from stress-strain plots.....	144
Figure 7.16: Average toughness values are obtained from the integral of stress-strain plots.....	144
Figure 7.17: Average strength values are obtained from the stress at sample fracture on stress-strain plots.....	145
Figure 7.18: Elastomer properties are taken to be unity and relative values for the composite are adjusted accordingly.....	146
Figure 7.19: A typical DSC plot of heat flow against temperature. Peaks correspond to the glass transition and melt peak. The dip corresponds to the crystallisation temperature.....	146
Figure 7.20: DSC curves showing the amorphous nature of both the silicone elastomer and the NT composite. The glass transition temperatures are -122.6°C ($\Delta C_p = 0.257 \text{ J/gK}$) and -123.8°C ($\Delta C_p = 0.281 \text{ J/gK}$) respectively.....	148
Figure 7.21: TGA plot of Sylgard 184 compared with a nanotube-containing composite.....	149
Figure 7.22: A TGA plot of Sylgard 184 shown with its derivative, and a TGA plot of the composite also shown with its derivative.....	149
Figure 7.23: An inverted plot of the curve obtained from subtracting the elastomer derivative peaks from the composite derivative peaks. The second graph shows the same data plotted on a log scale for clarity.....	150
Figure 7.24: Derivative of a TGA plot obtained for carbon nanotubes.....	151

Chapter 1: Introduction

1.1 Background and Motivation

Naturally occurring polymers have been around for many centuries and include proteins, natural rubber and silk. The diversity of these three examples gives an indication of the vast range of functions polymers can perform. A polymer is a long molecular chain composed of a number of linked repeating units. They therefore have high molecular weights. Over the centuries, naturally occurring polymers have been adapted to suit the needs of mankind. In 1909, the first completely synthetic polymer, called Bakelite, was developed [1]. Today there are many thousands of synthetic and natural polymers commercially available. They are more commonly referred to as plastics by consumers.

Polymers have many advantages over traditional materials (such as wood). They are lightweight and resistant to corrosion. This is due to the low density and chemical stability of polymers. In addition, materials are easy to process and can be moulded into complicated shapes. This reduces the amount of human input involved in manufacturing. As an example, prior to the invention of Bakelite wood was the material used for radio casings. Casings therefore had to be hand crafted increasing the time and cost of manufacture. When Bakelite was introduced casings could be machine processed and cast as one single unit. This resulted in the mass production of affordable radios. Polymers have also been used as a substitute for wood in applications such as children's toys. They are used as a replacement for concrete in pipes and, as an alternative to natural fibres in textiles. Other applications for polymers include window frames, mobile phone covers and insulation for electrical cables. Polymers are used for many diverse purposes. It is therefore an added advantage that properties such as strength and elasticity can be tailored to suit specific applications.

An important property of polymers is that they are insulating. The bonding in most polymers is such that all valence electrons are consumed by covalent bonds. As a result, there are no electrons free to conduct electricity. The insulating nature of polymers is an advantage for a wide range of applications. However, it restricts their use to situations where the conduction of electricity is not required.

Certain polymers, called conjugated polymers, have a bonding configuration whereby single and double bonds alternate along the polymer backbone. The π -electrons in a conjugated polymer are delocalised and can be used to conduct electricity. Conjugated polymers are made conductive by doping. This was discovered by Alan Heeger, Alan MacDiarmid and Hideki Shirakawa in 1977. All three were awarded the Nobel Prize in 2000 for their discovery of intrinsically conductive polymers. Unlike metals, conducting polymers have a low density, are easily moulded and are transparent to visible light. This opens up the possibility for cheap flexible electronics. Their capability as light emitting diodes and photovoltaics has been already been demonstrated [2-5].

A second way to make polymers conduct electricity is to add filler particles, thus creating a composite. A composite is any material made from two or more discrete substances. The components of a composite are generally referred to as the filler and the matrix. Composite materials display a blend of properties from these separate components. The matrix is frequently a polymer resin that binds filler particles (or fibres) together. Examples of commercially available composites are fibreglass-reinforced plastics and carbon fibre-reinforced plastics. Fibreglass-reinforced plastics are used in applications where high strength and corrosion resistance are required. For example, they are used in boat hulls. Carbon fibre-reinforced plastics combine high strength and stiffness with low weight. They are used in aircraft, spacecraft and high performance cars. Carbon fibres are also electrically and thermally conductive. Therefore, they can be used to impart conductivity to a polymer composite. Other conductive fillers such as metal particles can also be incorporated into polymers. One advantage composites have over inherently conductive polymers is that the filler simultaneously provides mechanical strength along with conductivity to the polymer. Composites are also more stable and robust than conductive polymers.

Carbon based materials make good fillers due to their low density and cost. They are also generally inert and compatible with most polymer systems. An example of a commonly used filler material is carbon black. It can be used to increase the abrasion resistance of rubber tyres and also for antistatic shielding applications. Carbon black particles are approximately spherical. They therefore have a low aspect (length-to-diameter) ratio.

Carbon fibres have a higher aspect ratio than carbon black and hence are a more efficient filler material. Carbon fibres can be introduced to a polymer host by mixing. They can also

be drawn into carbon fibre threads, which are woven into cloth and combined with a polymer. Carbon fibre composites can be used in applications where static charges cannot be tolerated. With higher carbon loadings, they can also be used to shield equipment from electromagnetic interference. Composites offer exceptional strength-to-weight ratio and can be moulded to fit complicated shapes. They have found applications ranging from formula-one cars to aeroplanes and bicycles. The high cost of carbon fibre fabric is offset by a reduced weight and consequently, a decrease in fuel consumption.

1.2 Carbon Nanotubes

Carbon nanotubes have an even higher aspect ratio than carbon fibres. They were discovered by Sumio Iijima in 1991 and are potentially the ultimate polymer reinforcement material [6]. The structure of a carbon nanotube is similar to a rolled-up sheet of graphene. The angle at which the tube is rolled-up determines whether the tubes are semiconducting or metallic. Over the past fourteen years there has been extensive research done in the field of carbon nanotubes (CNTs). The huge interest in these unique structures is due to their remarkable properties.

CNTs exhibit high mechanical strength along with excellent electrical and thermal conductivity [7-10]. They also have the advantage of being a low-density material with the ability to regain their original shape after compression. These properties suggest a whole host of potential applications including quantum wires and scanning probe microscopy tips to name but two [11-12]. Successful incorporation of CNTs into polymer matrices could result in applications such as flat panel displays, sensors, flexible electronic devices, and actuators [13-18].

1.3 Limiting Factors

The use of carbon nanotubes in commercial applications was originally limited by their high cost. Production methods have been steadily improving and as a result the cost has been steadily decreasing. Purified single-walled carbon nanotubes are currently available from Thomas Swan for \$360/g. Multi-walled nanotubes are cheaper and can be purchased (at 95% purity) from NanoLab for \$110/g. These prices decrease for bulk orders. As the demand for carbon nanotubes increases the cost is expected to fall. The number of

companies commercially selling carbon nanotubes is rising. Their main customers are currently researchers but this is expected to gradually shift towards industry.

The growth mechanism of nanotubes is not yet fully understood. This makes it impossible to specifically fabricate either semiconducting or metallic nanotubes. Existing production techniques result in a mixture of both being produced. For applications such as quantum wires and transistors, the conductive nature of the tubes is critical. For polymer reinforcement however, it is not of fundamental importance. While remarkable advances are being made in the area of production, it still remains a challenge to reproducibly grow bulk quantities of carbon nanotubes.

As carbon nanotubes are being produced, other carbonaceous impurities form along side them. Therefore, as-grown CNTs generally need to be purified. Purification is often a lengthy process during which a large percentage of tubes can be lost. By controlling variables such as the hydrocarbon flow rate during CNT synthesis it is possible to minimise the amount of amorphous carbon deposited. Again a small amount of amorphous carbon deposits will not prevent CNTs acting as a reinforcement for polymer systems. It may however, limit the level of reinforcement achieved.

Due to current problems associated with the controlled production of pure carbon nanotubes, one of their most realisable applications is in polymer composites. The level of reinforcement obtained depends on the interaction between the polymer matrix and the nanotubes. It also depends on the quality of the nanotube filler used and how well the tubes are dispersed within the matrix. Fortunately, a level of reinforcement can be obtained even with poor quality nanotubes. This means that tube quality is not necessarily a limiting factor in composite production. Dispersion of the nanotubes within the matrix is however an issue which must be addressed. CNTs tend to bundle together as they grow. This is due to Van der Waals forces between the tubes. Bundling reduces the surface area and aspect ratio of the CNTs and the bundles must be separated. This is not a simple task. Possible solutions include sonication and the use of a surfactant [19].

Many research groups have addressed the issue of nanotube-composite production. Remarkable improvements in both the strength and conductivity of the polymer have been reported [20]. The majority of composite production techniques involve mixing the CNTs into the polymer. This technique allows nanotubes to agglomerate together and also

prevents the positioning of nanotubes into pre-determined locations within the matrix. Positioning of CNTs is important for applications such as flat screens and flexible electronics.

In this Thesis a simple, economic method of CNT-polymer composite production will be explained in detail. Using this technique, nanotubes are well dispersed within the polymer matrix. The technique also allows the position of CNTs to be pre-determined. The mechanical and electrical properties of the composite will also be discussed.

1.4 Thesis Outline

During this thesis a novel method of carbon nanotube-polymer composite production will be presented. Using this technique the position, density and morphology of CNTs within a thin film polymer matrix can be controlled. Results demonstrating the electrical and mechanical enhancement of the polymer system when CNTs are embedded will also be presented.

Following this introductory chapter, the fundamental properties of carbon nanotubes are described in Chapter 2. This includes a full description of their structure, mechanical and electrical properties. Methods of CNT synthesis and their growth mechanism are then reviewed. State-of-the-art CNT-composite production techniques are also discussed. Finally, some commercial applications for these reinforced composites are explored.

Chapter 3 describes the synthesis of an unusual catalyst material called poly(styrene-vinylferrocene). This copolymer contains an iron core which is active during the growth of CNTs. The catalyst was characterised in detail to determine its composition, iron content and thermal stability.

Chapter 4 describes the use of soft lithography to pattern the catalyst material onto silicon oxide substrates. Soft lithography is a printing technique which employs the use of an elastomer stamp. We explain how to generate these stamps and demonstrate some possible patterns. We also show that catalyst particles are confined to within the dimensions of patterns features and absent elsewhere from substrate surfaces.

Chapter 5 focuses on carbon nanotube synthesis by chemical vapour deposition. We show how arrays of nanotubes can be grown onto substrates patterned with the catalyst poly(styrene-vinylferrocene). Control over the position, diameter and density of nanotubes is also demonstrated.

Chapter 6 describes the subsequent incorporation of as-grown CNT arrays into a polymer matrix. The location of nanotubes within the matrix is pre-determined and depends on the geometry of the catalyst pattern used. This provides a method of selectively positioning carbon nanotubes conduction channels through a polymer matrix.

In chapter 7 we focus on the characterisation of these polymer-nanotube composites. A dramatic improvement of the order 10^8 was recorded for the bulk conductivity and 10^6 for the surface conductivity. This shows that by incorporating carbon nanotubes an insulating matrix can be transformed into a conducting polymer. The mechanical reinforcement is not quite so impressive and we measure Young's modulus to increase by a factor of two.

Finally in Chapter 8, we review the main findings of this thesis and suggest a future direction for the work.

1.5 References

- [1] Leo H. Baekeland US patent 942,809, 12 July 1909 – Condensation Product and Method of Making Same.
- [2] JH Burroughs et al, *Nature*, 347, 539, 1990
- [3] AR Brown et al, *Appl. Phys. Lett.* 61, 2793, 1992
- [4] PL Burn et al, *Nature*, 356, 47, 1992
- [5] M Granstro, MK Petritsch, AC Arias, A Lux, MR Andersson, RH Friend, *Nature*, 395, 257, 1998
- [6] S Iijima, *Nature*, 354, 56, 1991
- [7] MMJ Treacy, TW Ebbesen, JM Gibson, *Nature*, 381, 678, 1996.
- [8] JWG Wildoer, LC Venema, AG Rinzler, RE Smalley, C Dekker, *Nature*, 391, 59, 1998
- [9] TW Odom, JL Huang, P Kim, CM Lieber, *Nature*, 391, 62, 1998.
- [10] MJ Biercuk, MC Llaguno, M Radosavljevic, JK Hyun, AT Johnson, *Appl. Phys. Lett.*, 80, 2767, 2002
- [11] SJ Tans, MH Devoret, H Dai, A Thess, RE Smalley, LJ Geerligs, C Dekker, *Nature*, 386, 474, 1997
- [12] H Dai, JH Hafner, AG Rinzler, DT Colbert, RE Smalley, *Nature*, 384, 147, 1996
- [13] S Fan, MG Chapline, NR Franklin, TW Tombler, AM Cassell, H Dai, *Science*, 283, 512, 1999.
- [14] WA de Heer, A Chatelain, D Ugarte, *Science*, 270, 1179, 1995.
- [15] Q Zhou, JR Wood, HD Wagner, *Appl. Phys. Lett.*, 78, 1748, 2001.
- [16] J Kong, N Franklin, C Zhou, MG Chapline, S Peng, K Cho, H Dai, *Science*, 287, 622, 2000.
- [17] M Kaempgen, GS Duesberg, S Roth, *Appl. Surface Sci.*, 252, 425, 2005.
- [18] RH Baughman, C Cui, AA Zakhidov, Z Iqbal, JN Barisci, GM Spinks, GG Wallace, A Mazzoldi, D De Rossi, AG Rinzler, O Jaschinski, S Roth, M Kertesz, *Science*, 284, 1340, 1999.
- [19] JM Bonard, T Stora, JP Salvetat, F Maier, T Stöckli, C Duschl, L Forró, WA de Heer, A Châtelain, *Adv. Mater.* 9(10), 827, 1997
- [20] AB Dalton, S Collins, E Munoz, JM Razal, VH Ebron, JP Ferraris, JN Coleman, BG Kim, RH Baughman, *Nature*, 423, 703, 2003.

Chapter 2: Background

In this chapter we explain why we are interested in reinforced polymers. We introduce some polymer background and explain why carbon nanotubes are potentially the ultimate filler for polymer systems. The properties and synthesis of carbon nanotubes are described in detail. We also review different methods of incorporating nanotubes into a polymer system. This increases the conductivity of the system while simultaneously providing increased mechanical strength. Finally, we discuss commercial interest in carbon nanotube reinforced composites.

2.1 Polymers

The word polymer is derived from the Greek words poly (many) and meros (part). A polymer consists of large molecular chains of repeating units. The smallest repeating unit of a polymer is called a monomer, again coming from Greek where mono means one. Polymerisation causes monomers to chemically bond together and form a polymer sequence. Copolymers can result where more than one type of monomer is present in the polymer chain.

Naturally occurring polymers have been around for many centuries and include proteins, nucleic acids, natural rubber and silk. Eventually some natural polymers were adapted to suit commercial needs. For example natural rubber (isoprene) is very responsive to heat. This causes it to be viscous in the summer but hard and brittle in winter. In 1839 Charles Goodyear realised that by cross-linking it with sulphur, it became more elastic and heat stable [1]. This treatment, called vulcanisation, facilitated a whole host of applications for rubber. The inevitable progression to synthetic polymers came in 1909 with the development of Bakelite [2]. Bakelite is a thermosetting plastic resistant to heat, moisture and most chemicals. It found many commercial uses including telephone fixtures and billiard balls. The first synthetic *fibres* spun from a molten polymer was developed by Dr. Wallace Carothers as an alternative to silk [3]. It was called Nylon and was introduced to the public in 1938. Nylon was initially used to make bristles for toothbrushes but more famously to make ladies stockings in 1940. Nylon polymers are commonly known as polyamides due to the recurring -CONH- group.

Today there are thousands of different plastics available. They can be economically produced on a large scale and are used for every application imaginable from food containers to airplane seats. Polymers possess a host of attractive qualities including durability, stability and mouldability. They are lightweight, non-porous, chemically stable materials.

Polymers are categorised as either thermosets or thermoplastics. A thermoplastic can be remoulded after heating. A thermoset cannot be remoulded due to the formation of chemical bonds and cross-linking within the polymer during processing. Polymers can be further classified as amorphous or crystalline depending on the degree of order amongst the polymer chains. No polymer is 100% crystalline. The characteristics of a polymer depend on physical properties such as branching and tacticity. Branching and tacticity affect the entanglement of polymer chains due to steric hindrance. The more entangled the polymer chain, the higher the melt temperature and the lower the percentage crystallinity. The characteristics of a polymer also depend on chemical properties such as the type and polarity of side groups. Side groups affect molecular interactions within a polymer and therefore influence the melting point and strength. For example, in Kevlar hydrogen bonding is responsible for its high tensile strength and melting point. Other possible types of interactions include dipole-dipole and Van der Waals, which are generally weaker.

The main advantage of polymers is the ease with which they can be processed. There are five main polymer-processing techniques. These are injection moulding, compression moulding, transfer moulding, blow moulding and extrusion. The process used depends on the shape of the part to be produced. For example injection moulding involves melting a polymer resin (usually in pellet form) and forcing it into a mould. The pressurised polymer is then held in the mould until it cools and solidifies in the shape of the mould. Airplane parts and combs are just two of the goods produced this way.

2.1.1 Conductivity in polymers

Polymers have proven to be invaluable materials for mankind. However, they are limited by their insulating nature. Valence electrons are all used up in covalent bonds. Electrons are therefore localised and not free to conduct electricity. In 1977 Alan Heeger, Alan, MacDiarmid and Hideki Shirakawa discovered that when polyacetylene was exposed to bromine vapours, its conductivity rose by seven orders of magnitude [4]. Polyacetylene is a

π -conjugated polymer meaning there are alternating single and double bonds along the polymer backbone. Single bonds consist of overlapping orbitals along the internuclear axis, called a σ -bond. Double bonds consist of a σ -bond and also a parallel π -bond. The π -bond is a result of overlapping orbitals directed perpendicular to the internuclear axis (figure 1).

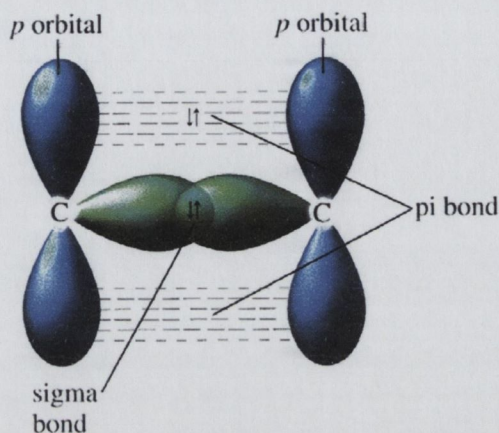


Figure 1: A double bond consists of a σ -bond and a π -bond.

In a conjugated polymer the π -electrons can become delocalised and shared along the polymer chain, enabling them to conduct electricity. Conjugated polymers can be considered as one-dimensional semiconductors. When polyacetylene is exposed to bromine vapours the bromine atoms can take π -electrons from the polymer leaving a hole behind on the polymer chain. The polymer can then conduct in the metallic region. Polyacetylene however is not stable in air and hence unsuitable for commercial applications. More stable intrinsically conducting polymers include poly(aniline), poly(phenylenevinylene) and poly(pyrrole). Delocalised bonds in these examples are due mainly to the presence of aromatic rings. Conducting polymers are extremely useful as they combine the electrical properties of a metal with the low density and processability of a polymer. Conducting polymers can be solution processed and can be used as transparent conductors. Potential applications include light emitting diodes, photovoltaics and printable electronics [5-7].

2.2 Conductive Fillers

Another way to make a polymer conduct is to add a conductive filler. Suitable filler particles include silver, nickel, platinum, gold, palladium and carbon. Above a certain loading filler particles form an interconnecting three-dimensional network. This provides a conduction pathway through the polymer. The onset of conductivity is a sharp transition

known as percolation. The volume fraction required for percolation depends on the conductivity and more importantly, the shape of the filler material [8]. Spherical particles require a high loading, whereas fibres link up more efficiently and reach percolation at much lower levels (figure 2).

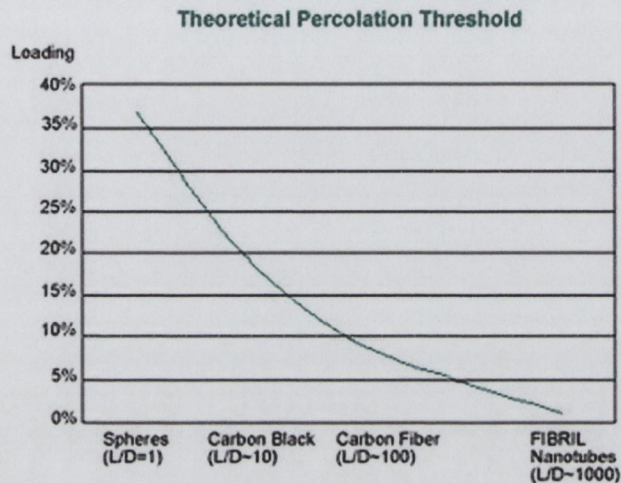


Figure 2: The percolation threshold is determined by the geometry of the filler particles. The L/D numbers refer to the length-to-diameter (aspect) ratio, and percolation can be predicted as $\sim 0.7 \langle D \rangle / \langle L \rangle$ [8]. (Graph from www.fibrils.com)

One of the main advantages of polymers is the ease with which they can be processed. Filler particles increase the viscosity of a polymer melt, making it more difficult to mould. To minimise this effect it is preferable to use small filler particles at a low loading. Carbon fillers are popular for many applications. This is due to the natural abundance and low cost of carbon. Carbon is also a low density material and acts as a lightweight filler. Different carbon geometries have been used to reinforce polymers. These include carbon black (which is approximately spherical), carbon fibres and more recently carbon nanotubes. Of the three, carbon nanotubes have by far the highest aspect ratio. This high aspect ratio combined with their high electrical conductivity makes carbon nanotubes the most efficient conductive filler available.

2.3 Carbon nanotubes: The ideal filler

2.3.1 Allotropes of carbon

Carbon is the sixth most abundant element in the universe. There are nearly ten million known carbon compounds and an entire branch of chemistry, known as organic chemistry, is devoted to their study. The carbon atom has an atomic number of six and electrons adopt the configuration $1s^2, 2s^2, 2p^2$ (figure 3). This bonding structure leaves four electrons in the valence (outer) shell. Carbon does not exist as isolated atoms and the valence electrons bond with other carbon atoms to produce stable molecules. Different types of bonds can form (sp , sp^2 and sp^3) resulting in the formation of carbon allotropes. These allotropes include polydiacetylene, graphite, diamond and fullerenes (figure 4). In polydiacetylene, sp hybridisation occurs as the s orbital mixes with one p orbital. This results in a linear bond where the remaining two electrons lie in p -orbitals perpendicular to the sp bond. In graphite, sp^2 hybridisation occurs. The s orbital mixes with two p orbitals and three valence electrons are equally distributed in a trigonal planar structure. The remaining electron lies in a p orbital perpendicular to the bonding plane. In diamond, sp^3 hybridisation occurs. The s orbital mixes with three p orbitals to form sp^3 hybridization. The four valence electrons are thus equally distributed among the sp^3 orbitals in a tetrahedral structure.

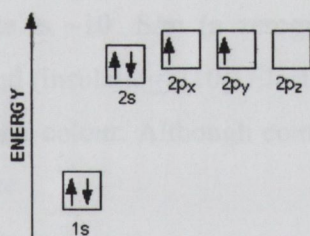


Figure 3: A carbon atom has the electron configuration $1s^2, 2s^2, 2p^2$. There are four valence electrons in the outer shell.

The properties of the various carbon forms differ dramatically and are determined by the hybridization of the atoms. Diamond is the hardest material known to man. This rigidity is due to the interlocking network of sp^3 covalent bonds. Each carbon atom is σ -bonded to four other carbon atoms with a bond length of 1.54 Å. Bond angles are all 109° . Diamond is a poor electrical conductor due to the absence of delocalised π -electrons. Electrons are all held tightly within σ -bonds between carbon atoms. These electrons do not absorb visible light and diamond appears transparent to the human eye.

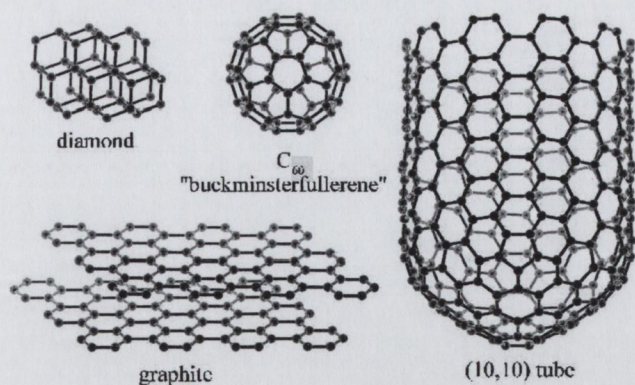


Figure 4: Allotropes of carbon include graphite, diamond and fullerenes. Fullerenes exist both as Buckyballs and carbon nanotubes.

Unlike diamond, graphite is soft and a good electrical conductor. Graphite consists of parallel sheets of hexagonal arrays of carbon atoms. The sheets are held together by weak Van der Waals forces, which are responsible for the soft and lubricating nature of graphite. Carbon atoms within the sheets exhibit sp^2 hybridization and form σ - bonds with three neighbouring atoms. The distance between atoms is 1.42 Å, which is shorter than for diamond. Carbon bonding within the layers is therefore stronger than in diamond. The π -orbital electrons (perpendicular to the graphite plane) are delocalized across the hexagonal sheets of carbon. They are therefore free to conduct electricity. In-plane conductivity for graphite is $\sim 10^5$ S/m (a zerogap semiconductor) [9]. This compares to $\sim 10^{-11}$ S/m for diamond (insulating) [10]. Electrons within the π -bonds interact with light to give graphite its black colour. Although commonly called lead, the material used in pencils is actually graphite.

Amorphous carbon is another possible form of carbon. It consists of distorted sp^3 and sp^2 bonds and hence, displays only short-range order. Amorphous carbon shows deviations of the interatomic distances, and/or interbonding angles, with respect to the graphite lattice as well as to the diamond lattice.

2.3.1.1 Fullerenes

Until 1985 the only known allotropes of carbon were diamond and graphite. Then, a hollow cage molecule was discovered by R.F. Curl, H.W. Kroto and R.E. Smalley [11]. The structure, containing sixty carbon atoms (C_{60}), was originally discovered in soot

produced from the laser ablation of graphite. The sixty atoms form a truncated icosahedron, which has the same vertices as a soccer ball (figure 5). Carbon atoms are located at each vertex of the hexagons and pentagons in the structure. C_{60} was given the name Buckminsterfullerene (or Buckyball) after the American architect R. Buckminster Fuller who designed the geodesic dome. This famous dome was constructed in the shape of a truncated icosahedron, the same as the structure of C_{60} . The 1996 Nobel Prize in Chemistry was awarded for the discovery of C_{60} .

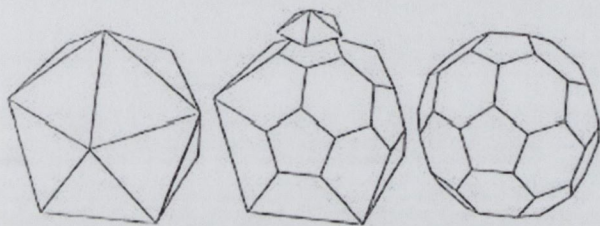


Figure 5: The structure of a Buckminsterfullerene can be obtained by truncating an icosahedron.

The buckyball can undergo many transformations, which will map the molecule onto itself. All symmetry operations must leave the center of mass of the molecule unchanged. Therefore, all rotation axes and symmetry planes must pass through the center of mass. Combining all rotations, reflections and inversions of the fullerene gives a total of 120 symmetry operations, making C_{60} the most symmetric molecule that exists.

Additional hexagons can be added to the C_{60} structure to produce molecules like C_{70} , C_{76} and C_{84} . As hexagons are added, the molecule begins to lose its round shape and becomes elongated until it eventually forms a cylindrical caged structure more commonly known as the carbon nanotube. Euler's theorem dictates that all fullerenes contain 12 pentagons independent of the number of carbon atoms present in the molecule (Appendix A). In a CNT the pentagons are located in the vicinity of the tip where they cause positive curvature and result in tube closure.

2.3.2 Structure of carbon nanotubes

Carbon nanotubes (CNTs) were discovered in 1991 by Sumio Iijima at NEC Corp., Japan [12]. They are an allotrope of carbon comprised of graphene sheets rolled up into a cylinder (figure 6). The elastic energy expended by rolling up the sheets, is compensated

for by the elimination of dangling bonds. These bonds, at the edges of graphene sheets, correspond to high-energy states and are incorporated into a seamless cylinder. Toward the tip, pentagonal cells in the graphene causes the nanotube to taper inwards and close. Both single-walled and multi-walled nanotubes have been observed. Multi-walled nanotubes (MWNTs) have a larger diameter and consist of a number of concentric single-walled tubes (SWNTs). The diameter for SWNTs is less than 2nm. Diameters for MWNTs range from 2-100 nm, depending on the number of shells present. The first carbon nanotubes observed were MWNTs. It wasn't until 1993 that the first SWNTs were discovered [13]. Carbon nanotubes are typically microns long but, tubes up to 4cm in length have been reported [14]. Combined with their narrow diameter, this leads to a high aspect ratio. As a result CNTs can be approximated to one-dimensional structures [15].

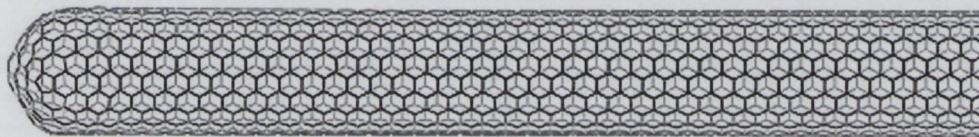


Figure 6: A single-walled carbon nanotube can be visualised as a rolled-up sheet of graphite capped by half a C_{60} molecule.

2.3.3 Electrical properties of carbon nanotubes

The electrical properties of a CNT are determined by its helicity and diameter [16]. If a CNT is imagined as a rolled-up graphene sheet, the helicity of the tube depends on the angle at which it is rolled-up. The helicity of a specific tube is described by its chiral vector [15]. The chiral vector (C_h) of an unrolled graphene sheet is defined as $n\mathbf{a}_1 + m\mathbf{a}_2$, where \mathbf{a}_1 and \mathbf{a}_2 are unit vectors of the hexagonal lattice and, n and m are integers (figure 7). The direction of C_h is perpendicular to the axis of the nanotube. The chiral angle (θ), is the angle between vectors C_h and \mathbf{a}_1 . Where θ is 0° (occurs when $m=0$), nanotubes have a zig-zag structure. Where θ is 30° (occurs when $m=n$), nanotubes have an armchair structure. For all other values of θ ($0^\circ < \theta < 30^\circ$) the tubes are chiral. The n , m and θ values for a particular CNT, determine the electronic behaviour of the tube. If $n - m$ is a multiple of 3 the tube is metallic otherwise, the tube is semiconducting [15]. This stipulates that one-third of all tubes are metallic (armchair structures) and the remaining two-thirds are semiconducting (zig-zag and chiral structures).

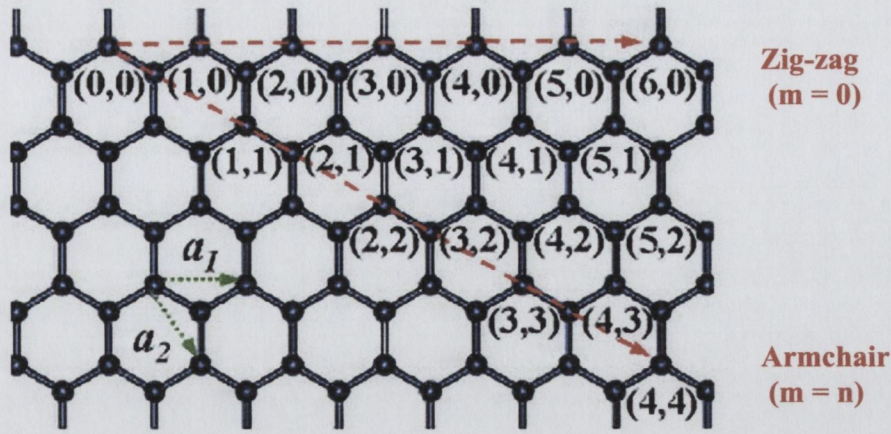


Figure 7: Nanotubes possess an armchair, zig-zag or chiral structure depending on n , m and θ .

Metallic CNTs have zero bandgap. The energy gap (E_g) for semiconducting tubes is a function of the tube diameter (d) and varies as $1/d$. Its value also depends on the carbon-carbon tight bonding overlap energy ($\gamma_0 = 2.7$ eV) and the nearest neighbour carbon-carbon distance ($a_{c-c} = 0.14$ nm). The energy can be calculated according to equation 1.

$$E_g = 2\gamma_0 a_{c-c} / d \quad \text{Equation 1 [15].}$$

The bandgap for a semiconducting nanotube is of the order 0.5 eV. The tube diameter can be measured using techniques such as scanning probe microscopy. It can also be calculated using the integers m and n from the chiral vector according to equation 2 (where a is the lattice constant 0.246nm).

$$d = a / \pi (n^2 + nm + m^2)^{1/2} \quad \text{Equation 2 [17].}$$

Carbon nanotubes are produced as a mixture of both semiconducting and metallic structures. Their conduction mechanism is similar to that for graphite, where delocalised π -orbital electrons are responsible for charge transport. The conductivity of an *isolated* MWNT, attached to bismuth contacts, was measured to be $\sim 10^5$ S/m [18]. This is similar to the value for graphite [9]. The value for CNTs should increase for defectless tubes where ballistic conduction is theoretically possible. Ballistic conduction occurs where the distance travelled by the electrons along the tube is less than their mean free path. Therefore, in a ballistic conductor electrons pass through the tube without scattering.

Measurements on SWNTs have revealed ballistic conduction behaviour. Javey et al studied palladium-contacted long SWNT devices and observed close to ballistic transport [19]. For tube lengths below 300nm, they attribute any extra resistance to acoustic phonons which can be made disappear at low temperatures. They noticed a resistance increase with tube length and suggest this is due to defect scattering, bending and chemical inhomogeneity along the tube. The quasi-ballistic conduction behaviour of CNTs means that very little heat is dissipated as current passes through them [18]. This means that high current densities can be tolerated without destruction of the tube. Extremely high stable current densities of more than 10^9 A/m² have been measured [20]. This is approximately 1000 times the current carrying capacity of copper [21]. This property is desirable if CNTs are to be used as electrical components.

Transport properties in electronic devices are expected to change considerably as the size of the device approaches molecular dimensions. Electric field induced displacement (electromigration) becomes a problem. Displacement is a result of momentum exchanges between moving electrons under the influence of an applied field. This leads to voids and short-circuits above critical current densities. CNTs have a high resistance to electromigration as the sp² bonds are more stable than small metallic structures [20]. In fact high current densities have been passed through CNTs over a period of two weeks without introducing defects to the tubes [20]. Electron scattering occurs in copper interconnects for dimensions below 100nm. This occurs at grain boundaries. Scattering means that that bulk conductivities for copper are not realised at molecular length scales.

2.3.4 Mechanical properties of carbon nanotubes

Carbon nanotubes are an extremely high strength material. The high elastic modulus of graphite sheets means CNTs may be stiffer and stronger than any known material [22]. This is due to strong covalent bonding between carbon atoms.

The average Young's (elastic) modulus for SWNTs was reported to be 1002 GPa (1 TPa) which, as expected, is similar to that for in-plane graphite [23]. The Young's modulus for MWNTs is slightly less and has been measured to lie between 270 and 950 GPa [24]. These values were measured using a 'nanostressing stage' located within a SEM. The nanotube is held at both ends by AFM cantilevers and stretched. The elongation of the tube

is plotted against the force applied. These values can be used to produce a stress-strain curve.

The Young's modulus is dependent on the number of defects in the CNT structure and the tube diameter. A second technique used to measure Young's modulus involves depositing CNTs onto a porous substrate. Some of the tubes will inevitably position themselves as 'bridges' across the pores. Atomic force microscopy (AFM) can then be used to apply a force midway along the suspended tubes' length. The deflection of the AFM tip is measured as a function of the force applied. This technique was used to measure the Young's modulus for arc-discharge tubes (640-1220 GPa) and for catalytically grown tubes (10-50 GPa) [25]. Arc-discharge produces crystalline CNTs. The catalytic process results in less-ordered tubes containing a larger number of defects. It is therefore obvious that the elastic properties of CNTs are influenced by the extent of structural defects and disorder. The elastic properties are also influenced by tube diameter, where smaller diameters correspond to a higher Young's modulus [26].

The breaking (tensile) strength of nanotubes is also linked to the extent of structural defects. Defects weaken the covalent bonding along the tube walls, which is responsible for their strength. The average tensile strength for a SWNT was measured to be 30 GPa [23]. This compares to a range of values from 11 to 63 GPa obtained for MWNTs [24]. These values were measured using a 'nanostressing stage', as described above. For MWNTs it was observed that the tubes broke in the outermost layer. This indicates that the outer shell carries the mechanical load.

CNTs are very resilient flexible structures. Individual MWNTs were shown to bend through large angles using a 'Nanomanipulator' AFM [22]. Bending was observed to be reversible. On the macroscopic scale, fibres of oriented SWNTs (up to 100 μm wide) were also shown to bend without breaking. In fact it is possible to bend the fibres through 360° and tie a knot without causing them to break [27]. The Young's modulus for these macroscopic fibres is substantially less than for individual SWNTs (9-15 GPa) [27]. This is to be expected as fibres consist of a number of individual SWNTs all aligned along the same direction, but not bonded to each other. Inter-nanotube areas represent weakened points where slippage can occur. A lower value for the Young's modulus is also due to the presence of amorphous carbon mixed in with the tubes.

The flexibility of CNTs allows them to buckle elastically under pressure. CNTs are therefore very energy absorbant (tough) and do not fracture easily [22]. Their hollow structure also allows them to be compressed. Once the stress has been removed, they can restore their original shape. This makes them suitable for shock absorption.

2.3.5 Applications

The excellent electrical and mechanical properties of CNTs make them suitable candidates for a wide variety of macro- and micro-applications. One of the most potentially lucrative applications for CNT is as field emitters. CNT arrays could be used as electron guns to illuminate a phosphor screen, thereby enabling flat-panel displays [28-34]. Traditional electron guns (cathode ray tubes) are based on thermionic emission and are bulky. CNT field emitters occupy negligible space and can be used to emit electrons efficiently in the presence of a relatively small applied voltage. Field emitters operate by the tunneling of electrons from a material into a vacuum in the presence of an electric field. The electrons do not have sufficient energy to go over the potential barrier. Therefore, a high electric field effectively thins the vacuum barrier and facilitates electron tunneling. Sharp tips create field enhancement, since the electric field is proportional to the inverse square of the tip radius ($1/r^2$). However, CNT field emitters produce a conical beam due to the radial direction of the electric field at the emitter surface. The uniformity of the field emission can be improved by creating an array of field emitters. Field emission properties are dependent on emitter densities. This is due to screening effects by neighboring emitter tips [36]. In 2002 Applied Nanotech Inc. (now Xintek, Inc.) demonstrated a 14inch diagonal CNT display. They are confident that flat-panel CNT displays will dominate the market and take over from plasma displays and liquid crystal displays. CNT field emitters could also be used for lighting elements [35].

CNTs can be used as compact sensor devices where chemisorption of different gases causes a change in conductivity [37-38]. CNT sensors display good sensitivity (due to their high surface area) and rapid response times. Adsorption of gas molecules however could irreversibly change CNT conductivity. An alternative technique was developed which works on the principle that all gases have different breakdown electric fields. CNT arrays are used to generate high electric fields at low voltages. This lowers the breakdown voltage of gases to be detected [39].

Nanotubes can also be used as actuators, converting electrical energy into mechanical energy. Actuation can be demonstrated by applying a bias voltage to Buckypaper in a salt solution. This causes a displacement of the Buckypaper [40]. In fact, SWNT sheets were shown to generate higher stresses than natural muscle [41]. Nanotubes could therefore be a suitable material to use in the production of artificial muscles.

A wide variety of other potential applications for CNTs include quantum wires [42], transistors [43] and interconnects [44]. However, their most realisable application is as a filler material for polymer systems. The incorporation of nanotubes provides simultaneous mechanical and electrical reinforcement to a polymer host. Super-tough composites have been reported with breaking energies higher than for Kevlar [45]. These nanotubes-polymer composites could be used in applications such as electronic textiles and bulletproof vests.

2.4 Carbon nanotube growth

For carbon nanotubes to be commercially viable, they need to be available in large quantities at affordable prices. In 1992 it was reported, for the first time, that nanotubes could be produced in macroscopic quantities [46]. Prior to 1992, there was much speculation regarding the possible properties of CNTs. The production of gram quantities provided sufficient amounts of nanotubes for experimentation and characterisation, bringing their potential closer to realisation. However, the challenge still remains to manufacture nanotubes on an industrial scale. For many applications it is also necessary to control the chirality, yield and number of defects present within the tubes. To achieve this level of control requires an understanding of the growth mechanism. There has been some research on this topic without any definitive solution emerging. The principal theories are the root- and tip-growth models which will be discussed later.

Since 1992, there have been many advances in the production of CNTs. Today there are essentially three CNT synthesis techniques. These are arc discharge, laser ablation and chemical vapour deposition (CVD). Using these techniques both single- and multi-walled carbon nanotubes can be produced. Over recent years CNTs have been generated with an increasing level of control over properties such as length, density and alignment. The diameter of a CNT is a little more difficult to control. However, significant progress is also being made in this area.

The arc discharge method, initially developed for C_{60} synthesis, was adapted by Ajayan and Ebbesen for carbon nanotube production [46]. During this process, a voltage is applied between two graphitic rods to create a plasma (or arc discharge). One of the graphite rods acts as a stationary anode and the other as a moveable cathode (or vice versa). As the cathode sublimates, multi-walled nanotubes are deposited onto the anode. The voltage drop across the electrodes can be maintained at a constant value by control over the anode-to-cathode distance. Adding a catalyst powder such as iron or cobalt to the graphitic rod of the cathode results in the formation of SWNTs. The synthesised product forms as an outer cylindrical shell of pyrolytic graphite with an inner core of soot containing nanotubes. This product has to be purified to extract the nanotubes. This can be achieved simply by sonication [46]. Enhanced purification can also be achieved by sonication followed by dispersion in poly(m-phenylenevinylene-co-2,5-dioctyloxy-p-phenylenevinylene), PmPV [47]. Arc discharge is carried out under an inert atmosphere such as helium. The helium pressure and current flow can be optimised to increase the yield and purity of nanotubes. In 2002 Cadek et al reported a yield of 24mg/min soot containing 48% nanotubes at 500 Torr of helium and a current density of 195 A/cm² [47]. Arc discharge is a valuable technique for the production of well graphitised carbon nanotubes. Negative aspects include the necessity for post production purification and the inability to grow CNTs in-situ onto a substrate. Arc-discharge is suitable for producing CNTs for limited research use and is not amenable for large scale production.

The laser ablation method was also adapted from a method used to produce C_{60} . It results in a more homogeneous product than arc discharge [48]. A pure graphite target rod is placed in the high temperature zone of a furnace. The system is pumped down to <10 mTorr and the temperature is increased to 1200°C. The target is then vaporized using a Nd:YAG laser under an argon atmosphere. The laser beam is focused onto the target where it rasters across the graphite surface. The argon flow transports the nanotubes produced downstream where they accumulate on a water-cooled copper collector. At lower synthesis temperatures, the yield and purity of the nanotubes was found to decrease [49]. The formation of tubes can be optimised by varying the carbon precursor and incorporating a metal catalyst into the target material. For example, using 5% nickel and cobalt catalyst powder mixed in with a C_{60} target, single-walled nanotubes were produced at temperatures as low as 400°C [48]. The same experiment performed substituting graphite for C_{60} results

in almost no SWNT formation. Laser ablation results in high quality tubes but, like arc discharge, it is not amenable for large-scale production.

Chemical vapour deposition (CVD) is considered to be the most promising technique for controlled nanotube growth while also being suitable for industrial scale-up. CVD generally operates at a lower temperature (600-1100°C) than either arc discharge or laser ablation. The process involves the catalytic decomposition of a hydrocarbon source into carbon radicals. These carbon radicals nucleate on a catalyst surface and restructure to form carbon nanotubes. Catalyst particles can either be introduced in the gas phase or patterned onto a substrate. Substrate patterning allows carbon nanotubes to be selectively positioned onto a wafer during growth. Therefore CVD can be used to fabricate electronic devices, such as interconnects and field emitters, which require nanotubes to be present in specific locations [50,29].

Properties such as the length, density and alignment of tubes can be controlled to a large extent using CVD. The length of fabricated carbon nanotubes scales with the growth time [51]. It has been reported by Pan et al that nanotubes 2mm long were grown after 48 hours deposition time. This was achieved by the decomposition of acetylene over an iron gel catalyst at 600°C. They believe that tube length could be further increased with longer growth time [52]. Therefore, by tailoring the process time either long or short tubes can be synthesised as required. Nanotube density can also be adjusted, as it is a function of the number of catalyst nucleation sites. Tu et al reported control over the catalyst site density using pulse-current electrochemical deposition. In their experiments, they placed a chromium working-electrode (along with a gold counter-electrode) in a nickel solution. By adjusting the current, duration and electrolyte concentration, the density and size of nickel nanoparticles could be altered in a range from 10^5 to 10^8 cm⁻² [53]. An alternative method for density control was described by Lastella et al. As their catalyst material they use a copolymer containing an organometallic block. The copolymer used is poly(styrene-ferrocenylethylmethylsilane). A thin film of this catalyst material will phase separate out into ordered nanodomains. After heating, the hydrocarbons vaporize leaving only iron nanoparticles remaining. These particles are uniformly dispersed and can be used to nucleate CNT growth. The block ratio and molecular weight of the copolymer catalyst determines the iron particle (and subsequent CNT) size and dispersion [54]. Nanotube alignment is another property which can be controlled. Alignment can occur either due to van der Waals interactions between the nanotubes where they are in close proximity to one

another [55] or, it can be induced by applying an external electric field [56,57]. Zhang et al demonstrated the growth of single-walled nanotubes across trenches. They show that in the absence of an electric field SWNTs display no preferred orientation and are suspended in random directions across the trenches. When an electric field is applied the CNTs align in the direction of the field [56].

Control over diameter is also important. This is especially true for electrical applications as the diameter of a CNT is linked to its bandgap. Increasing control over the tube diameter should allow control over the electronic nature of the tube and therefore enable semiconducting or metallic tubes to be selectively grown. Although it is not presently possible to grow CNTs with a pre-determined diameter and chirality, it is possible to obtain limited control over tube diameter. This is done by varying the size of the catalyst particles. It has been reported that the diameter increases with catalyst particle size but that this does not scale 1:1 using thermal CVD [58]. Therefore, it appears that chirality depends on more than the catalyst particle size. Other factors such as temperature, structure of the catalyst nanoparticles and the nature of the interface between the catalyst and its support substrate, may also play a role. It seems that the chirality of nanotubes depends also on the method by which they are produced. Dai et al have done some pioneering work in this area. They report that thermal CVD has no preference towards any particular chirality. Approximately 62% of tubes produced by this method are semiconducting [59]. This value ties in with predictions that one-third of nanotubes are metallic and the remaining two-thirds are semiconducting (section 2.3.3). HiPco[®] tubes also show no preference in chirality and 61% are reported to be semiconducting [60]. Laser ablation has a preference for metallic tubes (70%) [60]. While PECVD has a preference for semiconducting tubes (90%) [60]. It is not yet understood why this occurs. It seems that temperature and the presence of a plasma may be factors in determining chirality.

There are different variations of the CVD process. All are based on the same principle of hydrocarbon decomposition to form CNTs. The decomposition of these hydrocarbons is an endothermic process requiring a source of activation energy. This energy can be supplied either thermally or by a plasma. The resulting processes are called either thermal CVD or plasma-enhanced CVD.

Plasma-enhanced chemical vapour deposition (PECVD) is emerging as the most popular method for CNT synthesis. Using PECVD it is possible to control the vertical alignment of

CNT arrays. A plasma chamber contains two electrode plates. The substrate wafer is placed on one of the electrodes and a bias is applied. This leads to a breakdown of the feed gas, creating a plasma. The hydrocarbon feed gas is diluted with argon, hydrogen or ammonia to prevent the formation of excessive amounts of carbon radicals which can lead to the deposition of amorphous carbon [61]. Ren et al reported CNTs grown by PECVD on nickel-coated glass substrates. This was achieved below 666°C making the process suitable for flat panel displays [62]. The alignment control in PECVD is due to the bias applied across the electrodes. This results in the generation of an electric field with electric field lines pointing from the anode surface to the cathode surface. The high polarizability of nanotubes will cause alignment along the field direction. A dipole moment (**P**) is induced by the electric field (**E**) and depends on the polarizability tensor of the CNT (α) according to equation 3.

$$\mathbf{P} = \alpha\mathbf{E}$$

Equation 3.

The α -value has a much higher value along the tube axis than perpendicular to it causing CNTs to preferentially align parallel to the field [56]. Bower et al demonstrated that nanotubes always grow perpendicular to the substrate surface in PECVD. This occurs because of the perpendicular nature of a self-induced local field near the surface of the substrate. They were able to demonstrate nanotubes grown radially outwards from a variety of contoured surfaces [63]. In the same paper, Bower et al also showed that CNTs could be made to have a curled section followed by a straight section. They achieved this by switching on and off the applied electric field during growth [63]. This level of control makes PECVD an extremely attractive nanotube production method.

Another popular technique is the high pressure carbon monoxide (HiPco[®]) process. The activation energy for this CVD method is supplied thermally. An iron pentacarbonyl, Fe(CO)₅, catalyst is introduced along with carbon monoxide, CO, in the vapour phase. The Fe(CO)₅ thermally decomposes to produce iron catalyst particles. The CO pyrolyzes into carbon radicals on the surface of the iron where they reorganize to form carbon nanotubes. Increasing both temperature and pressure was shown to increase the SWNT yield [64]. Optimum temperatures are in the region of 900-1100°C and pressures can be upwards of 30 atmospheres [65]. Increasing the pressure speeds up the CO disproportionation rate and accelerates SWNT growth. The heating rate was found to be key. Slow heating allows iron particles to agglomerate into clusters before reaching the nanotubes growth temperature

[64]. Due to their large diameter, iron clusters will not nucleate nanotube growth but rather become overcoated with carbon. Carbon monoxide is used in preference to other hydrocarbon precursors, because CO disproportionation is much slower. This results in SWNTs which are essentially free of amorphous carbon. Many hydrocarbons have a tendency to decompose readily on any surface heated above 600-700°C which can often lead to the deposition of amorphous carbon deposits along with carbon nanotubes. HiPco[®] SWNT production at a rate of 10.8g per day has been reported [65]. This production technique is a continuous flow rather than a batch process and is suitable for scale-up. In fact in 2000 Dr. Richard E. Smalley and other researchers at Rice University (Texas) launched a company called Carbon Nanotechnologies Incorporated (CNI). CNI commercially supplies HiPco[®] nanotubes and also hold patents for a number of nanotube related technologies. CNI claims 700 customers worldwide including academic research centres and a variety of small and large companies. HiPco[®] nanotubes are ideal for bulk applications such as composite production where a mass of nanotubes can be mixed in with a polymer host. They are less suitable for applications such as electronics where nanotubes need to be positioned onto substrate wafers. PECVD is a more suitable method for these applications.

Another thermal CVD technique for bulk production is the decomposition of acetylene over a non-porous CaCO₃ supported catalyst. This is done at 720°C in a flow reactor. The presence of a catalyst support helps prevent the formation of carbonaceous by-products as there are no pores to trap residual carbon. Dilute nitric acid can be used to remove catalyst and support from the product. Possible yields of 100g/day have been reported for this technique [66].

Another variation of thermal CVD which has received a lot of attention is the ferrocene/xylene method. This allows for in-situ aligned growth. A ferrocene/xylene mixture is preheated and introduced in the vapour phase into a tube furnace. Nanotubes can be grown onto pre-patterned silicon oxide substrates. The position of nanotubes can be specified as they grow preferentially on silicon oxide rather than silicon. Using this method enables controlled three-dimensional growth over large area wafers [51]. Ferrocene/xylene grown nanotubes are aligned due to overcrowding and van der Waals forces. Nanotubes can be produced under atmospheric pressure at temperatures below 700°C. Increasing the xylene pressure causes amorphous carbon to be formed [67].

The ability to tailor the morphology of nanotubes grown using CVD, both plasma and thermal, makes it an ideal method for growing precise nanotube architectures. This level of control is not possible using either the arc discharge or laser ablation methods. The main disadvantage of CVD is that tubes tend to be poorly graphitised. The low temperature of production is accompanied by a reduction in crystallinity.

During our research thermal CVD was used as the method for carbon nanotube production. Nanotube arrays were required to be grown in-situ onto substrates. Therefore, of the three synthesis techniques mentioned above only CVD is suitable. We use thermal CVD in preference to plasma CVD as we do not require our CNTs to be aligned in one particular direction.

2.4.1 Catalyst

Catalyst particles play an essential role in the formation of carbon nanotubes. The most effective catalysts used for CNT growth are those based on the transition metals iron, cobalt and nickel. Iron, cobalt and nickel are active in a variety of configurations. They can be deposited onto substrates in their elemental form as thin metal films [58,62]. They can also be deposited in the liquid phase by dissolving metal salts and organometallics in solution. Metal salts which have resulted in the successful growth of carbon nanotubes include nitrates and chlorides, for example FeCl_3 and $\text{Fe}(\text{NO}_3)_3$ [68-71]. Examples of organometallics include phthalocyanines and the protein ferritin [72-73]. Vapour phase (floating) catalysts can also be used and are introduced along with the carbon source rather than patterned onto a substrate. These include metallocenes such as ferrocene, cobaltocene and nickelocene [67,74,75].

Bimetallic catalysts, such as cobalt-molybdenum, are sometimes used to control the concentration of the active catalyst element [76]. The active catalyst (cobalt) controls the hydrocarbon decomposition rate and its concentration is therefore critical. Metals such as molybdenum can be used to dilute the catalyst. This inhibits amorphous carbon decomposition and helps increase the production and quality of CNTs.

At high temperatures, catalyst particles have a tendency to migrate towards each other and form metal clusters. The diameter of these clusters can often be too large to nucleate CNT growth. Therefore, catalyst dispersion is an important issue and it has been approached in a

number of different ways. Bonard et al demonstrate that the adjunction of $\text{Al}(\text{NO}_3)_3 \cdot 9\text{H}_2\text{O}$ to ferritin molecules prevents the coalescence of iron nanoparticles as the ferritin decomposes at high temperatures. This results in monodisperse CNT growth when the compound is exposed to acetylene at 720°C [73]. Polymers can also be used to guide the formation of stable monodisperse metal nanoparticles. Polymers in solution adsorb onto the metal particles. The steric repulsion between polymer chains surrounding the metal will shield the van der Waals interactions between particles and prevent their agglomeration. Tannenbaum et al report a study on stabilizing iron nanoparticles. In their experiments, iron pentacarbonyl was mixed with a polymer, heated and decomposed into iron oxide. The strength of interaction between the iron and the polymer depends on the polymer used. For example polystyrene, PS, has a weak interaction compared to poly(methyl-methacrylate), PMMA, which has a much stronger interaction. Particle size decreases with increasing affinity and particle sizes of 67nm are reported in PS compared to 10nm in PMMA. The polydispersity of iron particles formed using this method is low at approximately 2-4nm [77].

Block copolymers have also been used to prevent agglomeration and control the size of catalyst particles. For example FeCl_3 salts have been used in combination with polystyrene-block-poly(2-vinyl-pyridine) [78,79]. Block copolymers can also be used as catalysts where an iron, cobalt or nickel centre is a constituent of the polymer. For our experiments we synthesize a block copolymer catalyst. The copolymer is poly(styrene-vinylferrocene) where iron is contained within the ferrocene block. To the best of our knowledge only one other group has attempted to use a copolymer where the catalyst material is actually embedded into the polymer [54]. Lastella et al use the polymer poly(styrene-b-ethylmethylferrocenylsilane). Their work was published subsequent to our own [80].

Under certain conditions, a catalyst material can also act as the carbon source. For example, iron phthalocyanine molecules, $\text{FeC}_{32}\text{N}_8\text{H}_{16}$, contain both metal and carbon source [81]. This material produced CNTs after pyrolysis under argon and hydrogen at temperatures above 800°C . Iron pentacarbonyl FeCO_5 has also been successfully used as both catalyst and carbon source to produce CNTs [82].

It has also been shown that CNTs can grow in the absence of a catalyst. Catalyst free growth on silicon carbide was achieved at temperatures above 1500°C. The high temperature involved restricts the implementation of this process [83].

2.4.2 Growth mechanism

To obtain control over the properties of carbon nanotubes produced it is essential to understand their growth mechanism. Our focus is on CVD synthesis of CNTs. Production by this method involves the decomposition of a hydrocarbon precursor into carbon vapour. Ordered carbon is then produced by diffusion, and subsequent precipitation, of this vapour through catalyst particles. This ordered carbon evolves into CNTs either by a tip- or root-growth mechanism.

One of the advantages of CVD synthesis is that the catalyst can be patterned onto a substrate for in-situ growth. At high temperatures catalyst particles tend to migrate towards each other and form globular clusters. Where the geometry of the cluster is suitable to catalyse CNT growth, the hydrocarbon molecules will decompose at the cluster surface [84]. The carbon vapours produced deposit on one half of the catalyst surface where they diffuse into the catalyst forming a solid solution. The supersaturated metal then precipitates solute in the form of ordered carbon at the opposite side of the catalyst. The migration of the dissolved carbon across the catalyst particle is due to a concentration gradient [85-86]. The precipitated carbon is graphitic in nature and oriented perpendicular to the catalyst surface. As more carbon is precipitated, cylindrical tubes form to eliminate dangling bonds and form a more energetically stable structure. Carbon does not precipitate at the apex of the catalyst particle resulting in the hollow structure of CNTs [85]. Graphitic structures only form in close proximity to the catalyst particles [85].

Growth can proceed from the precipitation stage in one of two ways. The first way is that tubes form upwards from the catalyst which remains attached to the substrate. The other alternative is that metal particles detach from the substrate and move at the tip of the growing fibre. These are the two growth models which are most commonly referred to in literature. They are known as the root- and tip-growth models [85,87,88]. For CNT growth to proceed, the catalyst particle must be exposed to carbon vapours so that further carbon atoms can be incorporated. For the root growth model, the catalyst can be accessed at the

sides. For the tip growth model, the catalyst can be accessed at the sides and also at the top of the particle (Figure 8).

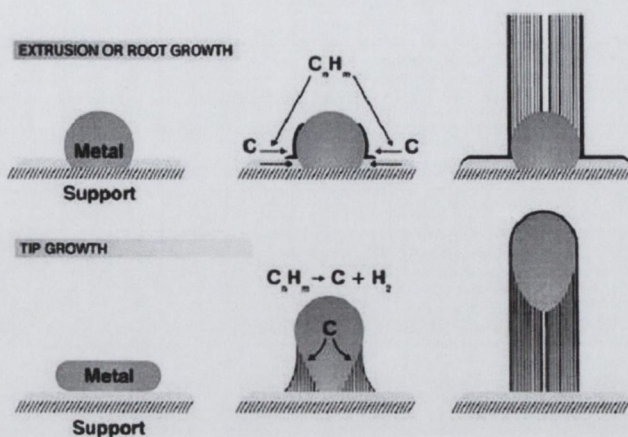


Figure 8: The two leading theories on the mechanisms of carbon nanotube growth are the root- and tip-growth models.

An alternative theory for the root growth model, suggests that pentagons form early on in the growth process. This facilitates curvature of the sp^2 bonded carbon precipitated from the catalyst. A dome (or cap) structure therefore forms early on in the growth process [89]. A weak adhesion between the dome and the catalyst enables the arched graphene sheet to float on the curved particle surface [90]. The catalyst particle hinders closure and stabilizes dangling bonds.

Without direct observation of the process it is difficult to ascertain the exact growth mechanism. It has been shown using transmission electron microscopy that both root- and tip-growth do occur [84,87]. It appears that the growth mechanism depends on the strength of the catalyst-substrate interaction. Where there is strong adhesion, it would appear that root growth dominates. Song et al report that PECVD prefers tip-growth. They suggest that the plasma roughens the substrate surface and causes catalyst particles to become isolated. This decreases the adhesion force between the catalyst and the substrate. They report that the exact same substrate used in thermal CVD results in root-growth due to stronger catalyst interactions [87].

CNT growth ceases when the catalyst particles become encapsulated by graphene layers. Thus effectively cutting the carbon supply. For successful CNT growth, it is essential that the reaction be restricted to the catalyst surface. This can be controlled by the choice of

carbon precursor, carbon feed rate, pressure and temperature [85]. The decomposition rate of the carbon source is critical so that all carbon radicals have time to diffuse through the catalyst and form nanotubes. Where reaction occurs away from the catalyst surface, deposits of amorphous carbon form.

The catalyst particle size also plays a critical role in CNT growth. Above a critical diameter, CNTs will not form. When the catalyst size is too large, it exceeds the diffusion length of the carbon atoms and CNTs do not form [91]. At higher temperatures, carbon atoms have a higher mobility and hence a longer diffusion length [84]. Slightly larger catalyst particles can therefore be used to grow nanotubes. Presumably there is also a lower limit for the catalyst size. As the diameter continues to decrease, the tube curvature increases which imposes more strain on the graphene sheets. At a certain point the strain energy for the resulting CNT must become too large [91].

A conclusive model for the mechanism of carbon nanotube growth has not yet been reported. This is partly due to inconsistent experimental data and also due to the difficulties associated with directly observing CNT growth. In an attempt to monitor in-situ CNT growth, Geohegan et al demonstrated how time-resolved reflectivity could be used to measure the length of CNTs during growth. They show that growth rates vary depending on catalyst preparation, time and temperature. They measured the highest growth rate at 730°C and observed no growth below 565°C [92]. In 2004, CNT growth was directly observed for the first time. Helveg et al used time resolved in-situ transmission electron microscopy. Interestingly they see that the catalyst nanocluster changes shape during growth. This appears to assist the alignment of graphene layers into tubes. The catalyst becomes elongated up to a critical point and then contracts back to a spherical shape. They propose that the increase in surface energy required for elongation is sustained by the energy gain when binding the graphitic fibre to the catalyst surface [93]. Shape fluctuations are energetically unfavourable for large particles thus offering another explanation as to why large particles are ineffective catalysts [94].

The experimental conditions (such as temperature and electric field) under which CNTs can be successfully grown vary greatly. It is therefore likely that more than one growth mechanism is in operation. Until these growth mechanisms are deciphered, there is no way to predict the effect that experimental parameters have on the structure of resulting CNTs. Therefore, it is currently impossible to precisely and repeatedly tailor CNT growth.

2.4.3 Catalyst Patterning

The ability to transfer a pattern onto a substrate is essential for numerous applications. The most obvious being in the semiconductor industry where silicon wafers are etched to produce integrated circuits. Moore's law drives feature sizes to be smaller and smaller each year. However as the minimum feature size decreases, the cost of equipment escalates. Industry is continually seeking techniques which can pattern high resolution nanoscale arrangements at affordable prices.

Substrate patterning is also an important step in growing ordered arrays of carbon nanotubes. The positions of the CNTs are determined by the location of catalyst particles. The catalyst can be deposited in a variety of designs using a number of different techniques. Successfully used patterning techniques include photolithography and electron beam deposition [95-96].

Photolithography is also known as optical lithography. The substrate is covered with a photoresist layer and exposed to UV light through a chrome-patterned quartz mask. The exposed resist degrades (if positive photoresist is used) and can be washed away. The unexposed resist remains. Reactive ion etching or wet etching can then be used to etch the exposed regions of the substrate. When etching is complete, the remaining resist is removed and a patterned substrate is revealed (figure 9). Any pattern that can be transferred onto a chrome-on-quartz mask can be used. The resolution of this technique is limited by the wavelength of UV light and process parameters.

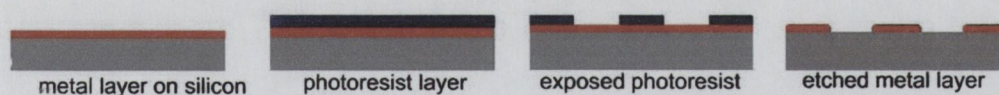


Figure 9: Schematic of how photolithography can be used to pattern a metal layer on silicon.

E-beam lithography is a similar technique except electrons (rather than light) are used to draw a pattern in an e-beam resist. Higher resolution is possible as electrons have a smaller wavelength than light. There is no need for a mask but patterning is slower as the pattern must be "drawn" over the entire substrate.

Recent advancements such as deep ultra-violet (DUV) have made it possible to reduce the minimum feature size of photolithography to the nanolithography region. In fact Intel produce the Pentium® M Processor which employs 90nm process technology using 248nm DUV. In 2004 they announced a 65nm technology with a 35nm transistor gate length. This is etched using 193nm DUV lithography [97]. They are currently extending their capabilities toward the extreme ultra-violet (EUV) region where the wavelength of light is a mere 13.5nm. EUV lithography is positioned for commercial deployment in 2009. Intel is aiming to reach 32nm processing by then.

Other thriving nanolithography patterning techniques include scanning probe lithographies and nanoimprint lithography. Scanning probe lithographies (SPL) use an atomic force microscopy (AFM) tip to transfer nano-patterns onto a substrate. An AFM tip can effectively be used as a “pen” where it is dipped into “ink” and used to write a pattern onto a substrate [98]. This particular technique, called Dip-Pen-Nanolithography (DPNTM), was developed by Prof. Chad Mirkin’s research group. The dimensions of the AFM tip are such that patterning on the molecular scale is possible, the scanning speed however is very low. To increase the efficiency, many probe arrays can be used in parallel to simultaneously write aligned patterns. The technique is seen as an alternative to e-beam lithography and has been commercialised by NanoInk, Inc..

Nanoimprint lithography (NIL) is based on research done by Prof. Chou’s group [99]. A mould is pressed into a thin resist layer (such as PMMA) on a substrate. The resist is heated above its glass transition temperature and deforms to take the shape of the mould. The mould can be then removed and the resist is etched to transfer the pattern onto the substrate below. This process is expected to have sub-10nm resolution. The moulds for NIL are made by conventional lithography. These moulds are durable and can be used for mass production. NIL is a fast low-cost patterning technique. The technology has been commercialised by Nanonex. A similar technique is Step and Flash Imprint Lithography (S-FILTM). An imprint resin is deposited onto a substrate and contacted with a transparent mould. The resin adopts the pattern of the mould and is polymerised by exposure to UV. The mould is then removed to reveal a replica of the pattern. The technology was developed by Grant Willson and S.V. Sreenivasan and has been commercialised by Molecular Imprints.

2.4.3.1 Soft lithography

Soft lithography is an example of another fast low-cost patterning technique. This technique uses an elastomer stamp to print materials onto a substrate [100]. The process was first developed in 1993 when Kumar and Whitesides reported that an elastomer stamp inked with alkanethiol could be used to pattern self-assembled monolayers onto a gold surface [101]. Soft lithography is a versatile process and can be used to deposit many different materials onto a variety of substrates. The material is first dissolved in solution. Then a moulded elastomer stamp is used to print the solution onto a substrate. The shape and dimensions of the molded elastomer can be easily modified for a variety of patterns. This simple process is seen as a more economical alternative to optical lithography.

Soft lithography has many advantages over conventional patterning techniques in that it can be done under atmospheric conditions. This makes it more convenient and cost effective. Many other processes require clean room conditions and often low pressures. Soft lithography is an additive process and therefore reduces the amount of material wasted. Also, due to the flexible nature of the elastomer stamp, soft lithography can be used to print onto non-planar substrates. These surfaces are difficult and often impossible to pattern by other techniques.

Stamps for soft lithography are generally made from silicone elastomers such as poly(dimethylsiloxane), PDMS. The elasticity and low surface energy of siloxanes allows them to release easily from surfaces. Stamps therefore conform and seal reversibly against a substrate. Areas greater than 50cm^2 can be patterned in a single impression [100]. Silicones are durable, chemically inert and generally compatible with liquid-phase catalysts. Their elastic behaviour allows them to regain shape even after significant strain. However, for replication of features below 500nm, a harder material must be used for the stamp. Michel et al report feature sizes of down to 50nm using a material with Young's modulus of 9.7 MPa (versus a modulus of 3 MPa for PDMS) [102].

The aspect ratio of features moulded into the elastomer stamp is important and must lie within a certain range. Where printing posts are too slender, they can stick together and fall under their own weight. Where posts are shallow, sagging of the recesses separating posts can occur and cause unwanted contact with the substrate. Soft lithography therefore is not suitable for patterning widely separated features. Both these scenarios (of slender and

shallow posts) cause a distortion of the intended pattern. The stamping process can be modified to minimise these concerns. This is achieved by adding a rigid back plate to the elastomer. A pressure supply attached to the back plate allows localized controlled contact between the stamp and the substrate. This technique, called wave-printing, ensures proper conformal contact without the risk of sagging [103]. The back plate also enables multilayer alignment. High resolution can be problematic with elastomers as they are prone to distortion. This generally limits fabrication to single-layer structures. Rigid back plates help eliminate lateral distortions. Wave-printing has been used to demonstrate large area polymer electronics [104].

The term soft lithography covers all processes which pattern substrates using an elastomer stamp or mould. A number of processes exist. These include soft embossing, microcontact printing, microtransfer moulding and micromoulding in capillaries. For example, if we wish to pattern a polymer onto a substrate. Using soft embossing, the polymer film would be applied to the substrate, contacted with the stamp and then heated to make film soft. The set-up would then be cooled under pressure allowing the polymer freeze into position. The stamp can then be removed leaving a patterned polymer behind. Microcontact printing involves depositing the polymer solution onto the stamp. The solvent is allowed to evaporate and then the stamp is printed onto the substrate. For microtransfer moulding, a prepolymer is poured into the stamp. The excess is removed and the stamp is then placed on the substrate. The stamp/mould is removed after the prepolymer has cured. Finally, micromoulding in capillaries involves contacting the substrate with the stamp. A drop of prepolymer placed at one end of stamp and fills channels by capillary action. The prepolymer is left to cure and then the stamp is removed.

The particular type of soft lithography used depends on the properties of the material to be patterned and also, on the geometry of the pattern required. Any material can be patterned using soft lithography providing that it can be made into solution. It also must be compatible with the elastomer used to make the stamp.

2.4.3.2 Soft lithography patterning for CNT growth

Soft lithography is a convenient, quick and economic patterning technique. As such, it is ideal for patterning catalyst materials onto substrates for CNT growth. The most effective catalysts for CNT growth are iron, cobalt and nickel. These can be deposited as thin metal

films or as metal compounds. Metal films are deposited using techniques such as sputtering. Sputtering unfortunately does not limit the deposition of metal to the substrate surface alone and results in wasted material. Metal catalysts are also active when used in formations such as salts and organometallics. These materials can be made into solution and patterned onto substrates by soft lithography. This is a much more efficient technique for growing controlled CNT arrays.

Kind et al report the successful growth of CNT arrays using an iron salt, $\text{Fe}(\text{NO}_3)_3 \cdot 9\text{H}_2\text{O}$, dissolved in ethanol. The solution was patterned onto substrates by microcontact printing using a PDMS stamp. CVD resulted in the selective growth of CNTs onto line patterns. More uniform growth was obtained using an ethanol solvent rather than a water solvent. This is because ethanol has a higher vapour pressure and evaporates without leaving drying traces. The density of nanotubes grown can be controlled by varying the concentration of the iron solution [105]. At certain concentrations, CNTs will grow aligned perpendicular to the surface. Above a critical concentration however, only amorphous carbon is deposited [106]. Control over CNT density is key for applications such as field emission where there is an optimum inter-emitter distance. Other salts such as $\text{FeCl}_3 \cdot 6\text{H}_2\text{O}$ have also been used to catalyse CNT growth. Cassell et al report the growth of suspended SWNT bridges. The iron salt catalyst was deposited on the surface of silica towers using a PDMS stamp. CNTs were then grown by CVD using methane [107].

2.5 Carbon nanotube composites

A composite material is one made up of two or more distinct components. The characteristics of the individual components combine to produce a material with enhanced properties. A vast number of composites have been generated by combining materials such as metals, ceramics and polymers together. One of the most commonly used composite materials is glass-reinforced plastic where fine fibres of glass are used to reinforce polymers. Frequently used polymers are polyester and epoxy. The resulting composite is more commonly known as 'fibreglass'. Fibreglass has a high strength-to-weight ratio, is heat stable and resistant to corrosion. Applications include car bumpers, aircraft components and boat hulls. For certain applications, carbon fibres have been used to replace glass fibres as a polymer filler.

Carbon-fibre-reinforced plastic is a strong, light and very expensive composite material. Factors such as fibre alignment and choice of matrix will affect the properties of the resulting composite. It is also important to eliminate air pockets as these will degrade the strength of the material. The high cost of carbon fibers is compensated for by the material's excellent strength-to-weight ratio. This can result in lower fuel consumption where composites are used in the aeronautical and automotive industries. Large sections of Formula One cars are made from carbon fibre composites, where the reduction in the weight of the car is worth the expense. Carbon fibres have also been used to reinforce graphite in a material called reinforced-carbon-carbon. This is suitable for high-temperature applications and is used as part of the space shuttle frame.

Carbon fibres are structurally analogous to rolled up graphene sheets. Fibres are typically microns wide with an aspect ratio in the region of 100. An entire carbon fibre is made from one continuous graphene sheet which has dangling bonds at the edges. Carbon nanotubes can also be envisioned as rolled up graphene sheets. However, nanotubes roll up to form a seamless cylinder and eliminate dangling bonds. Concentric cylinders (multi-walled tubes) may form but each one can be imagined as made from a separate graphene sheet. The diameter of carbon nanotubes is typically less than 30nm. This results in a high aspect ratio which regularly exceeds 1,000. Their high aspect ratio makes carbon nanotubes potentially the ultimate reinforcement for polymer composites [45].

2.5.1 CNT composite production mechanisms

The potential applications for carbon nanotubes have been well publicised. One of their most attainable applications is as a filler for polymer systems. Polymers are limited by their insulating nature. Adding a conductive filler can open up a whole host of new uses for polymers. Due to their unique structure, the most efficient filler material is carbon nanotubes. CNTs can be up to 100 times stronger than certain types of steel at only one-sixth the weight [24,108]. They also have a higher current carrying capacity than copper [21]. Resulting composites could combine the desirable properties of a polymer with the advantages of having high strength and conductivity supplied by the CNTs.

There are many ways to incorporate carbon nanotubes into a polymer matrix. The first polymer-nanotube composite was made by mechanical mixing [109]. Other techniques such as solvent-based methods and in-situ polymerisation were subsequently developed

[111,115]. Composite films can be made by spin coating, or drop casting, CNT-polymer solutions [113]. Polymer-nanotube yarns can also be produced where a nanotube solution collapses into a fibre on contact with a coagulant [45].

The first polymer-nanotube composite was made by Ajayan et al in 1994 [109]. Purified arc-discharge nanotubes were randomly dispersed in an epoxy resin by mechanical mixing. Cured composites were then sliced into thin films using a diamond knife. This induced alignment of nanotubes along the cutting direction. Sandler et al later used the same technique. A dispersed nanotube solution was mixed with an epoxy resin, the solvent evaporated and hardener was added. Despite constant stirring at each stage of the process, they reported that a number of nanotubes remained entangled. The composite produced therefore has a non-uniform consistency which means that properties such as strength and conductivity are not optimal. Nevertheless, a conductivity of 10^{-2} S/m was measured for volume fractions as low as 0.1 vol.%, indicating that further increases should be possible with better nanotube dispersion [110].

An alternative way to produce composites is by the solution-based method where nanotubes and polymer are dissolved in solution. For example, MWNT powder and poly(m-phenylenevinylene-co-2,5-dioctoxy-p-phenylenevinylene) were mixed together in toluene and sonicated. The solvent can then be evaporated. The electrical conductivity of the composite increased dramatically by eight orders of magnitude. Good wetting of the CNTs by the polymer was observed due to the ability of the coiled polymer to wrap around the nanotubes [111]. The use of a helical polymer enables the separation of CNTs from other phases present in as-produced CNT powder. The polymer coils wrap around the tubes and holds them in suspension while other impurities settle, and can be decanted away. Therefore as the composite is made, the CNTs are simultaneously purified. Suspensions of polymer wrapped CNTs are stable over an indefinite period of time. Polymers which are unable to wrap around nanotubes cannot hold them in suspension. In this case all carbon material settles out of solution [112].

The solvent fraction of a polymer-nanotube solution can be evaporated to produce a composite powder. Alternatively, the solution can be drop cast, or spin coated, to produce a thin film composite. Using the solution-based method, the weight percent of nanotubes in these composites is easily controlled. However, aggregation of CNT bundles is an issue where polymer chains are unable to wrap around individual tubes to disperse them. The

nanotubes will preferentially bundle due to the high polarizability of π -electrons which make them subject to large van der Waal forces. Bundling reduces the properties of the tubes and also make for non-uniform composites. Careful mixing of the solutions is essential so that polymers can coat the nanotubes and stabilize against flocculation. Dispersion can also be achieved by sonication or by the use of a surfactant which acts as a coupling agent and introduces steric repulsive forces. Thin films containing evenly dispersed nanotubes have been cast from polymers such as poly(vinyl alcohol) [113].

More ordered composites can be made by soaking a CNT sheet (Buckypaper) in a polymer solution. The intercalated polymer enhances load transfer between nanotubes and an increase in the Young's modulus and tensile strength occur. Buckypaper was prepared by filtration of SWNTs in water and Triton X-100. This was annealed and then soaked in a polymer solution. A variety of polymers such as poly(styrene), poly(vinyl alcohol) and poly(vinyl pyrrolidone) can be used [114].

As an alternative method to solution processing, composites can be made by in-situ polymerisation where a monomer is added to a CNT solution and subsequently polymerised. For example aniline was added to a sonicated MWNT solution followed by an oxidant to polymerise the monomer [115,116]. Where straight MWNTs are present during aniline polymerisation, a planar polyaniline (PAN) conformation forms as a coating on the CNTs. This composite is a soluble powder which can be further processed. Dissolving the composite powder in PAN means that the aligned bundles are distributed to form randomly oriented 3-dimensional networks. The composite has increased thermal stability and electrical conductivity increases nine orders of magnitude [117].

Composites can also be made in the form of fibres. These fibres can then be woven into textiles. Baughman et al produced several-hundred-metre-long CNT composite fibres which had a higher toughness than spider silk [45]. Spider silks ability to absorb mechanical energy without breaking is attributed to flexible amorphous regions located between rigid crystalline proteins. The composite fibres produced have patches of amorphous polyvinyl alcohol between SWNTs. Strengths were measured to be 1.8GPa [118].

The same group also report an innovative method to synthesise strong transparent metre-long CNT sheets. This was achieved by drawing MWNTs from the sidewall of an as-

grown array. MWNT sheets can easily adhere to elastomer films to form a bilayer composite which can be bent in any direction without degrading electrical conductivity [119].

2.5.2 Nanotube Functionalisation

Stress transfer from a polymer matrix to a filler material occurs at the interface between the two materials. Therefore, the strength of the interaction between the components of the composite is important. The bonding between nanotubes and their polymer host can be enhanced by functionalising the nanotube surface to allow for covalent bonding. Functionalisation can also act to help dispersion and increase entanglement between tubes and polymer chains. Excessive functionalities will however disrupt the crystallinity of the CNT structure.

CNTs can be functionalised by refluxing in acid [120]. The carboxylic acid side groups can be incorporated into the tube walls at defect sites. One possible route is then for oxidised tubes to bond to an epoxide side group. Epoxide groups open under an acid or alkali environment. They can then attach onto the CNTs. One group used poly(dimethylsiloxane) polymer with an epoxide side group [121]. Functionalisation based on acid treatments however are not ideal as partial destruction of the graphene tube walls occurs. This reduces the mechanical strength and electrical conductivity of the tubes. An increase in percolation ensues and more CNTs are required for reinforcement.

One way to address this issue is to attach an anionic initiator onto CNT walls. An initiator, such as *sec*-butyllithium, can be added in calculated amounts to a solution of nanotubes. Monomers added to this solution will attach onto the initiator to form carbanions. These carbanions then initiate anionic polymerisation. Viswanathan et al grafted polystyrene onto HiPcoTM SWNTs by anionic polymerisation [122]. Using this technique, it is possible to limit the extent of functionalisation that occurs. They report ~10% polystyrene grafted onto the tubes. A shift in the glass transition temperature of the composite verified the close interaction between the polymer and the nanotubes. In the absence of bonding a shift would not have been observed.

A similar approach was reported by Blake et al where butyllithium functionalised MWNTs were reacted with chlorinated polypropylene [123]. This resulted in covalent bonding

between the tubes and the polymer. They report a higher level of polymer grafted onto the tubes (31%). Analysis of the composite showed a Young's modulus increase by a factor of three. This indicates efficient dispersion and a good level of interfacial stress transfer.

Fluorinated SWNTs have also been fabricated where polymers such as poly(ethylene oxide) were added onto the functionality. This resulted in mechanical enhancement of the polymer due to covalent linkage between the tubes and the matrix. The side-wall fluorination did not degrade the properties of the nanotubes. Fluorination also acted to increase the dispersion of tubes in the polymer [124].

2.5.3 Composite Properties

The unusual structure of carbon nanotubes leads to a host of remarkable composite properties. The π -bonding along the sidewalls allows for excellent electrical conduction while strong carbon-carbon bonds are responsible for mechanical robustness. Their high aspect ratio suggests that percolation in a composite may be achieved at low loading levels. High strength combined with a low weight suggests that they may be the ultimate reinforcement for polymer materials [45].

2.5.3.1 Mechanical Properties

Their low density makes nanotubes ideal for mechanical reinforcement of lightweight systems. The density of MWNTs has been reported as 2.6 g/cm^3 which means that they become airborne very easily [125]. SWNTs have an even lower density. This makes them difficult to contain and work with. However, when incorporated into a polymer matrix the motion of the tubes is restricted and the composite is easy to handle and manipulate.

Mechanical strength enhancement is due to load transfer from the polymer matrix to the embedded tubes [126]. This occurs at the interface between the two materials. The large surface area-to-volume ratio of the nanotubes increases the interfacial area available for contact with the polymer matrix. This enables greater stress transfer to occur. The strength of the interface depends on the interaction between the polymer and nanotubes. Some polymers coil around nanotubes to form intimate contact. Others form a wetting layer or a crystalline shell around the tube to enhance interfacial stress transfer. However, the strongest interface appears to be created by functionalisation. The Young's modulus of

polymers is on average seen to double, or at most triple, when CNTs are added to the matrix [123]. However, the average Young's modulus for SWNTs is 1 TPa, or slightly less for MWNTs [23,24]. This would suggest that the potential for nanotube reinforcement of polymers has not yet been realised.

Nanotubes embedded in a polymer can absorb energy applied to the matrix increasing the toughness of the composite [45]. CNTs elastically and reversibly buckle under stress making them very energy absorbant. Composites therefore should be able to absorb energy and sustain large loads. Composites are further improved by the ability of nanotubes to bridge any cracks that appear in the in matrix.

The level of reinforcement attained depends on the aspect ratio of the nanotubes. Thinner longer tubes are more efficient as they form an interconnecting 3-dimensional scaffold structure more easily. This acts to stiffen the polymer. It has been reported that short, discontinuous fibres showed no appreciable load transfer because of low aspect ratio [127]. It is more difficult for short tubes to arrange into a scaffold support structure.

The level of reinforcement also depends on the crystallinity of the polymer host. Carbon nanotubes are thought to nucleate crystallisation in semi-crystalline polymers. As a crystalline polymer shell forms around the nanotubes, greater stress transfer can occur due to a better interaction between the two components. For example, nanotubes were used to reinforce two polymers, polyvinyl alcohol and poly(9-vinyl carbazole). Polyvinyl alcohol, PVA, is a semi-crystalline polymer (14% crystallinity). When 1wt% nanotubes were added to PVA, the crystallinity increased to 27% and good stress transfer was observed. Poly(9-vinyl carbazole), PVK, on the other hand is amorphous. As a result poor stress transfer was observed. This is despite the coiled nature of PVK sidechains, indicating that polymer wrapping does not play a crucial role in mechanical reinforcement [128]. A similar result was reported for polyacrylonitrile, PAN. Crystallinity in PAN can be induced. This was observed when SWNTs were added to the polymer [129].

The separation stress required to pull nanotubes out of a polymer matrix was measured in a nanopullout experiment. This involved heating a thermoplastic polymer (polyethylene-butene) to soften and pushing a CNT into the surface using AFM. The tube must be inserted perpendicular to the polymer surface and must only be inserted to a specific embedded length. The set-up is then cooled and the CNT is pulled out from the matrix. The

force required to separate the CNT from solid polymer can then be calculated. Separation stress was found to be remarkably high indicating good adhesion between tubes and polymer. Interfacial strengths were reported between 10 and 100 MPa depending on whether bonding is covalent or not. Properties of the polymer immediately surrounding the tubes is stronger than in bulk [130]. Hence good dispersion is key for uniform reinforcement throughout the entire composite.

2.5.3.2 Electrical Properties

When incorporated into a polymer system, CNTs provide conduction channels through the insulating matrix. Their large aspect ratio enables them to form 3-dimensional interconnecting structures at a low loading level. This results in a continuous conductive pathway for charge flow. This critical loading level is called percolation. Below the percolation threshold, conductivity through the polymer remains poor. This threshold decreases as the aspect ratio of the filler particles increases [131]. This is important as low loading levels allow the intrinsic properties of the matrix to be retained. It has been reported that when the CNT volume fraction exceeds 10wt%, the viscosity of the composite is too large for processing [132].

A quantity of nanotubes contains both metallic and semiconducting tubes. The conductivity of individual tubes is 10^5 S/m, which lies in the pseudometallic region [18]. The conductivity of most polymers lies in the region of 10^{-10} S/m but can vary depending on purity, conformation and defect concentration. The conductivity of a binary composite comprising of nanotubes dispersed in a polymer depends on a number of factors. These include the volume fraction of nanotubes, the properties of the individual nanotubes, the intimacy of contact at the polymer-nanotube interface, the dispersion of the tubes, and the structure of the polymer host material.

Adding CNTs to poly(m-phenylenevinylene-co-2,5-dioctoxy-p-phenylenevinylene), PmPV, caused an increase in conductivity ten orders of magnitude. Percolation was found to occur between 7 and 11wt.%. PmPV is a coiled polymer and wraps around CNTs to hold them in solution. The solution can then be spin coated onto a substrate to produce a thin film composite. Replacing PmPV with the linear polymer polymethylmethacrylate did not produce the same result, as the polymer is unable to hold the tubes in suspension [133]. The structure of the polymer is therefore important in composite formation. It has also

been reported in literature that PmPV may not be the best matrix (lower percolation thresholds have been observed). PmPV coats CNTs with a thick polymer layer resulting in poor electrical contact, thus hindering intertube conduction [131].

Composite fibres tougher than spider silk were made from SWNTs and poly(vinyl alcohol), PVA [45]. The conductivity of these fibres was reported to lie between 0.01 and 2.5 S/cm (1-250 S/m). Replacing PVA with an ionic conductor called polyethyleneimine, PEI, resulted in an electrical conductivity one hundred times greater than that for the SWNT/PVA composite fibres. In this instance, PEI serves as the intertube binding agent. Amines interact well with nanotubes via physisorption onto tube walls. Conductivity values were measured to lie between 10 and 30 S/cm using HiPco[®] SWNTs. This value increased to between 100 and 200 S/cm when SWNTs produced by laser ablation were used [132]. Perhaps this can be explained in terms of CNT chirality. It is known that HiPco[®] tubes are mainly semiconducting (61%) [60]. Tubes produced by laser ablation are primarily metallic (70%) [60]. A bulk sample of nanotubes produced by laser ablation would therefore be expected to display a higher conductivity.

It is clear that nanotubes can be used to change the electronic nature of polymers. Electrical conductivity can be increased several orders of magnitude. Due to their insulating nature, polymer are associated with electrostatic charge build-up, the addition of nanotubes allows this charge to be dissipated. In addition to providing enhanced mechanical strength and electrical conductivity to polymers, carbon nanotubes are also thermally conductive. Nanotubes allow for heat dissipation thus helping to prevent over-heating and possible degradation of a polymer [134]. Carbon nanotubes also have good chemical resistance making composites durable and resistant to environmental corrosion. Therefore, there are many benefits to be gained from adding nanotubes to a polymer system.

2.5.4 Commercial applications for nanotube composites

Carbon nanotubes have vast potential due to their extremely high strength and superior conductivity. Possibly their most promising application is as a component in composite materials where these properties can be translated to a polymer host. An added benefit of CNTs is their high aspect ratio. This facilitates reinforcement at low loading levels. The advantage of using a low filler loading is that the viscosity and subsequent processability of the composite will be unaffected by reinforcement. CNTs have the potential to

revolutionise the polymer industry and every major polymer company in the world is now paying attention to their potential impact.

Some research centres have produced impressive reinforcement of polymers using nanotubes. Composite fibres have been reported which can be woven into textiles. This opens up the possibility of clothing that could store electrical energy. These fibres could also be used for synthetic muscle [135]. Fibre sensors and bulletproof vests are other applications. Carbon nanotubes were used to reinforce Zylon fibres, poly(p-phenylene-benzobisoxazole), PBO. Zylon is the strongest polymer available (it is twice as strong as Kevlar). Adding 10% HiPco SWNTs to the as synthesised PBO polymer results in a tensile strength increase of 50%. The tensile strength of commercial Zylon is 5.8 GPa meaning that (with a 50% strength increase) composite fibres with strength above 8GPa are theoretically possible [136].

The first commercial nanotube product sold was a polymer composite which incorporated CNTs as a conductive filler. This product was sold by Hyperion Catalysis. Hyperion was founded in 1982 to develop novel forms and morphologies of carbon. In the 1990's they pioneered the production of FIBRIL™ nanotubes (MWNTs) in multiton quantities. These CVD grown MWNTs are entangled but can be separated by proprietary techniques. Distribution of FIBRIL™ nanotubes was curtailed by the fact that those using the tubes for research were not free to independently pursue patents (this clause expired in 2004) [137]. Hyperion incorporate FIBRIL™ nanotubes into a variety of polymers hosts and the resulting composites are sold commercially. Conductivities of 0.01 to 0.1 S/cm have been reported for 5% loading [137]. This is well above the requirement for electrostatic discharge materials. These composites are bought primarily for use in automotive and electronic industries where they are used for electrostatic charge dissipation. Static charging in automobile fuel systems can lead to explosions. Conductive composites can be used to eliminate this risk. Small amounts of nanotubes can also be incorporated into plastic components to be electrostatically painted. This eliminates the need for a conductive primer and the efficiency of electrostatic painting can be increased 2-3 times [138]. The low loading levels required means that the surface finish of the plastic component is not compromised.

Zyvex is another company which have been active in the commercialisation of CNTs. They have developed a surface treatment (NanoSolve™) for carbon nanotubes to enhance

their interaction with a polymer host material. The treatment can be tailored to produce excellent dispersion in a variety of polymers and solvents [139]. The good dispersion enabled by NanoSolve™ results in a lower percolation threshold. Percolation occurs at a loading of 0.045% in polystyrene, where conductivity increases ten orders of magnitude [140]. Using this technology, composites can be made for applications such as conductive paints, conductive adhesives, electromagnetic interface shielding and electrostatic discharge applications [140].

Another company involved in commercialising carbon nanotubes composites is Eikos. They are interested in the production of flexible transparent conductive films (Invisicon™) focusing primarily on applications in the displays market. Applications for this technology include touch screens and flexible electronics. Eikos expects that the market for conductive films will reach \$4 billion by 2006.

Applications for CNTs are currently limited by their high cost, the difficulties associated with purification and the lack of precise control over the properties (such as chirality) of tubes produced. Composite applications are limited by the tendency of tubes to agglomerate together and form bundles. Dispersing CNTs within a polymer enables percolation to be reached at a much lower loading level. The quantity of tubes required for reinforcement is thus reduced. With low CNT loadings, composites could become affordable as commercial products. The amount of CNTs required for reinforcement also decreases as the quality of the tubes increases. Another significant issue is the strength of the polymer-CNT interface. When all these issues have been resolved it is expected that composites based on CNTs will bring about the most significant change to the textile industry since the introduction of synthetic fibres in the 1930's. The exponential increase in CNT patents filed in recent years reflects the level of commercial interest [137].

2.6 References

- [1] Charles Goodyear US patent 3633, 15 June 1844 – Improvement in India-Rubber Fabrics
- [2] Leo H. Baekeland US patent 942,809, 12 July 1909 – Condensation Product and Method of Making Same.
- [3] Wallace H. Carothers US patent 2,071,250, 16 February 1937 – Linear Condensation Polymers
- [4] H. Shirakawa, E.J. Lewis, A.G. MacDiarmid, C.K. Chiang, A.J. Heeger, *J. Chem. Soc. Chem. Commun.* 579, 1977.
- [5] Burroughs J H et al, *Nature*, 347, 539, 1990
- [6] Burn P L et al, *Nature*, 356, 47, 1992
- [7] M. Granstrom, K. Petritsch, A. C. Arias, A. Lux, M. R. Andersson, R. H. Friend, *Nature*, 395, 257, 1998
- [8] I Balberg, *Phys. Rev. B*, 31 (6), 4053, 1985
- [9] HD Young, RA Freedman, *University Physics*, 9th Ed., (Addison Wesley), 1996, p. 804
- [10] Kaye and Laby, *Table of Physical and Chemical Constants*, 16th Ed., 1995
- [11] HW Kroto, JR Heath, SC O'Brien, RF Curl, RE Smalley, *Nature*, 318, 162, 1985
- [12] S Iijima, *Nature*, 354, 56, 1991
- [13] S Iijima, T Ichihashi, *Nature*, 363, 603, 1993. D. S. Bethune, C. H. Kiang, M. S. de Vries, G. Gorman, R. Savoy, J. Vazquez, R. Bevers, *Nature*, 363, 605, 1993.
- [14] LX Zheng, MJ O'Connell, SK Doorn, XZ Liao, YH Zhao, *Nature Materials*, 3, 673, 2004
- [15] JWG Wilder, LC Venema, AG Rinzler, RE Smalley, C Dekker, *Nature*, 391, 59, 1998
- [16] TW Odom, JL Huang, P Kim, CM Lieber, *Nature*, 391, 62, 1998
- [17] LC Venema, V Meunier, Ph Lambin, C Dekker, *Phys. Rev. B*, 61(4), 2991, 2000
- [18] AY Kasumov, II Khodos, PM Ajayan, C Colliex, *Europhys. Lett.*, 34(6), 429, 1996
- [19] A Javey, J Guo, Q Wang, M Lundstrom, H Dai, *Nature*, 424, 654, 2003
- [20] BQ Wei, R Vajtai, PM Ajayan, *Appl. Phys. Lett.*, 79(8), 1172, 2001
- [21] ET Thostenson, Z Ren, TS Chou, *Comp. Sci. Technol.*, 61, 1899, 2001
- [22] MR Falvo, GJ Clary, RM Taylor, V Chi, FP Brooks et al, *Nature*, 389, 582, 1997
- [23] MF Yu, BS Files, S Arepalli, RS Ruoff, *Phys. Rev. Lett.*, 84(24), 5552, 2000
- [24] MF Yu, O Lourie, MJ Dyer, K Moloni, TF Kelly, RS Ruoff, *Science*, 287, 637, 2000
- [25] JP Salvetat, AJ Kulik, JM Bonard, G Andrew, D Briggs et al, *Adv. Mater.*, 11(2), 161, 1999

- [26] JP Salvetat, JM Bonard, NH Thomson, AJ Kulik, L Forro, W Benoit, L Zuppiroli, *Appl. Phys. A*, 69, 255, 1999
- [27] B Vigolo, A Penicaud, C Coulon, C Sauder, R Pailler, *Science*, 290, 1331, 2000
- [28] WB Choi, DS Chung, JH Kang, HY Kim, YW Jin et al, *Appl. Phys. Lett.*, 75(20), 3129, 1999
- [29] S Fan, MG Chapline, NR Franklin, TW Tomblor, AM Cassell, H Dai, *Science*, 283, 512, 1999
- [30] JM Bonard, JP Salvetat, T Stockli, WA de Heer, L Forro, A Chatelain, *Appl. Phys. Lett.*, 73 (7), 918, 1998
- [31] WA de Heer, A Chatelain, D Ugarte, *Science*, 270, 1179, 1995
- [32] RC Smith, DC Cox, SRP Silva, *Appl. Phys. Lett.*, 87, 103112, 2005
- [33] CHP Poa, SJ Henley, GY Chen, AADT Adikaari, CE Giusca et al, *J. Appl. Phys.*, 97, 114308, 2005
- [34] PC Smith, JD Carey, CHP Poa, DC Cox, SRP Silva, *J. Appl. Phys.*, 95(6), 3153, 2004
- [35] H Murakami, M Hirakawa, C Tanaka, H Yamakawa, *Appl. Phys. Lett.*, 76(13), 1776, 2000
- [36] JM Bonard, N Weiss, H Kind, T Stockli, L Forro, K Kern, A Chatelain, *Adv. Mater.*, 13(3), 184, 2001
- [37] KG Ong, K Zeng, CA Grimes, *IEEE Sensors Journal*, 2 (2), 82, 2002
- [38] J Kong, NR Franklin, C Zhou, MG Chapeline, S Peng, *Science*, 287, 622, 2000
- [39] A Modi, N Koratkar, E Lass, B Wei, PM Ajayan, *Nature*, 424, 171, 2003
- [40] J Fraysse, AI Minett, O Jaschinski, GS Duesberg, S Roth, *Carbon*, 40, 1735, 2002
- [41] RH Baughman, C Cui, AA Zakhidov, Z Iqbal, JN Barisci, *Science*, 284, 1340, 1999
- [42] SJ Tans, MH Devoret, H Dai, A Thess, RE Smalley, C Dekker, LJ Geerligs, *Nature*, 386, 474, 1997
- [43] SJ Tans, ARM Verschueren, C Dekker, *Nature*, 393, 49, 1998
- [44] F Kreupl, AP Graham, GS Duesberg, W Steinhogel, M Liebau, *Microel. Eng.*, 64, 399, 2002
- [45] AB Dalton, S Collins, E Munoz, JM Razal, VH Ebron, JP Ferraris, JN Coleman, BG Kim, RH Baughman, *Nature*, 423, 703, 2003
- [46] W Ebbesen, PM Ajayan, *Nature*, 358, 220, 1992.
- [47] M Cadek, R Murphy, B McCarthy, A Drury, B Lahr, M ih Panhuis, JN Coleman, R Barklie, WJ Blau, *Carbon*, 40, 923, 2002.
- [48] Y Zhang, S Iijima, *Appl. Phys. Lett.*, 75 (20), 3087, 1999.

- [49] T Guo, P Nikolaev, AG Rinzler, D Tomanek, DT Colbert, RE Smalley, *J. Phys. Chem.*, 99, 10694, 1995
- [50] Y Homma, T Yamashita, Y Kobayashi, T Ogino, *Physica B*, 323, 122, 2002.
- [51] BQ Wei, R Vajtai, Y Jung, J Ward, R Zhang, G Ramanath, PM Ajayan, *Nature*, 416, 495, 2002.
- [52] ZW Pan, SS Xie, BH Chang, CY Wang, L Lu, W Liu, WY Zhou, WZ Li, LX Qian, *Nature*, 394, 631, 1998.
- [53] Y Tu, ZP Huang, DZ Wang, JG Wen, ZF Ren, *Appl. Phys. Lett.*, 80(21), 4018, 2002.
- [54] S Lastella, YJ Jung, H Yang, R Vajtai, PM Ajayan, CY Ryu, DA Rider, I Manners, *J. Meter. Chem.*, 14, 1791, 2004.
- [55] C Singh, M Shaffer, K Koziol, IA Kinloch, AH Windle, *Chem. Phys. Lett.*, 372, 860, 2003.
- [56] Y Zhang, A Chang, J Cao, Q Wang, W Kim, Y Li, N Morris, E Yenilmez, J Kong, H Dai, *Appl. Phys. Lett.*, 79(19) 3155, 2001.
- [57] A Ural, Y Li, H Dai, *Appl. Phys. Lett.*, 81(18), 3464, 2002.
- [58] OA Nerushev, S Dittmar, RE Morjan, F Rohmund, EEB Campbell, *J. Appl. Phys.*, 93(7), 4185, 2003.
- [59] W Kim, HC Choi, M Shim, Y Li, D Wang, H Dai, *Nano Lett.*, 2(7), 703, 2002
- [60] Y Li, D Mann, M Rolandi, W Kim, A Ural, S Hung, A Javey, J Cao, D Wang, E Yenilmez, Q Wang, JF Gibbons, Y Nishi, H Dai, *Nano Lett.*, 4(2), 317, 2004
- [61] M Meyyappan, L Delzeit, A Cassell, D Hash, *Plasma Sources Sci. Technol.*, 12, 205-216, 2003.
- [62] ZF Ren, ZP Huang, JW Xu, JH Wang, P Bush, MP Siegel, PN Provencio, *Science*, 282, 1105, 1998.
- [63] C Bower, W Zhu, S Jin, O Zhou, *Appl. Phys. Lett.*, 77 (6), 830, 2000.
- [64] P Nikolaev, MJ Bronikowski, RK Bradley, F Rohmund, DT Colbert, KA Smith, RE Smalley, *Chem. Phys. Lett.*, 313, 91-97, 1999.
- [65] MJ Bronikowski, PA Willis, DT Colbert, KA Smith, RE Smalley, *J. Vac. Sci. Technol. A*, 19 (4), 1800, 2001.
- [66] E Couteau, K Hernadi, JW Seo, L Thien-Nga, Cs Miko, R Gaal, L Forro, *Chem. Phys. Lett.*, 378, 9-17, 2003
- [67] R Andrews, D Jacques, AM Rao, F Derbyshire, D Qian, X Fan, EC Dickey, J Chen, *Chem. Phys. Lett.*, 303, 467, 1999
- [68] NS Kim, SY Bae, J Park, *Mat. Res. Soc. Symp. Proc.*, Vol. 800, AA3.5.1
- [69] S Huang, L Dai, AWH Mau, *Adv. Mater.*, 14 (16), 1140, 2002

- [70] J Kong, HT Soh, AM Cassell, CF Quate, H Dai, *Nature*, 395, 878, 1998
- [71] H Kind, JM Bonard, L Forro, K Kern, K Hernadi, LO Nilsson, L Schlapbach, *Langmuir*, 16, 6877, 2000.
- [72] S Huang, AWH Mau, TW Turney, PA White, L Dai, *J. Phys. Chem. B*, 104 (10), 2193, 2000.
- [73] JM Bonard, P Chauvin, C Klinke, *Nano Lett.*, 2 (6), 665, 2002.
- [74] HM Cheng, F Li, G Su, HY Pan, LL He, X Sun, MS Dresselhaus, *Appl. Phys. Lett.*, 72 (25), 3282, 1998
- [75] R Sen, A Govindaraj, CNR Rao, *Chem. Phys. Lett.*, 267, 276, 1997.
- [76] XZ Liao, A Serquis, QX Jia, DE Peterson, YT Zhu, *Appl. Phys. Lett.*, 82 (16), 2694, 2003.
- [77] R Tannenbaum, M Zubris, EP Goldberg, S Reich, N Dan, *Macromol.*, 38, 4254, 2005.
- [78] Q Fu, S Huang, J Liu, *J. Phys. Chem. B*, 108, 6124, 2004.
- [79] G Gu, G Philipp, X Wu, M Burghard, AM Bittner, S Roth, *Adv. Funct. Mater.*, 11 (4), 295, 2001.
- [80] E Lahiff, CY Ryu, S Curran, AI Minett, WJ Blau, PM Ajayan, *Nano Letters*, 3, (10), 1333, 2003.
- [81] S Huang, L Dai, AWH Mau, *J. Phys. Chem. B*, 103, 4223, 1999.
- [82] J Liu, M Shao, Q Xie, L Kong, W Yu, Y Qian, *Carbon*, 41, 2101, 2003.
- [83] V Derycke, R Martel, M Radosavljevic, FM Ross, Ph Avouris, *Nano Lett.*, 2(10), 1043, 2002
- [84] C Ducati, I Alexandrou, M Chowalla, GAJ Amaratunga, J Robertson, *J. Appl. Phys.*, 92(6), 3299, 2002.
- [85] SB Sinnott, R Andrews, D Qian, AM Rao, Z Mao, EC Dickey, F Derbyshire, *Chem. Phys. Lett.*, 315, 25, 1999.
- [86] C Klinke, JM Bonard, K Kern, *Phys. Rev. B*, 71, 035403, 2005.
- [87] IK Song, WJ Yu, YS Cho, GS Choi, D Kim, *Nanotechnol.*, 15, S590, 2004
- [88] A Maiti, CJ Brabec, J Bernholc, *Phys. Rev. B*, 55(10), 55, 1997
- [89] X Fan, R Buczko, AA Puretzky, DB Geohegan, JY Howe, ST Pantelides, SJ Pennycook, *Phys. Rev. Lett.*, 90 (14), 145501, 2003.
- [90] JY Raty, F Gygi, G Galli, *Phys. Rev. Lett.*, 95, 096103, 2005.
- [91] H Kanzow, A Ding, *Phys. Rev. B*, 60(15), 60, 1999
- [92] DB Geohegan, AA Puretzky, IN Ivanov, S Jesse, G Eres, *Appl. Phys. Lett.*, 83(9), 1851, 2003.

- [93] S Helveg, C Lopez-Cartes, J Sehested, PL Hansen, BS Clausen, JR Rostrup-Nielsen, F Abild-Pedersen, JK Nerskov, *Nature*, 427, 426, 2004.
- [94] PM Ajayan, *Nature*, 427, 402, 2004
- [95] S Huang, L Dai, A Mau, *Physica B*, 323, 333, 2002
- [96] KBK Teo, M Chhowalla, GAJ Amaratunga, WI Milne, DG Hasko, G Pirio, P Legagneux, F Wyczisk, D Pribat, *Appl. Phys. Lett.*, 79(10), 1534, 2001
- [97] P Bai, C Auth, S Balakrishnan, M Bost, R Brain et al, *International Electron Devices Meeting*, p. 657, 2004.
- [98] CA Mirkin, S Hong, LM Demers, *Chem. Phys. Chem.*, 2, 37, 2001.
- [99] SY Chou, PR Krauss, PJ Renstrom, *J. Vac. Sci. Technol. B*, 14(6), 4129, 1996
- [100] Y Xia, GM Whitesides, *Angew. Chem. Int. Ed.*, 37, 550, 1998.
- [101] A Kumar, GM Whitesides, *Appl. Phys. Lett.*, 63(14), 2002, 1993
- [102] B Michel, A Bernard, A Bietsch, E Delamarche, M Geissler et al, *IBM J. Res. Dev.*, 45(5), 697, 2001.
- [103] MMJ Decre, R Schneider, D Burdinski, J Schellekens, M Saalmink et al, *Mat. Res. Soc. Symp. Proc.*, Vol. EXS-2, M4.9.1
- [104] J Schellekens, D Burdinski, M Saalmink, M Beenhakkers, G Gelinck et al, *Mat. Res. Soc. Symp. Proc.*, Vol. EXS-2, M2.9.1
- [105] H Kind, JM Bonard, L Forro, K Kern, K Hernadi, LO Nilsson, L Schlapbach, *Langmuir*, 16, 6877, 2000.
- [106] H Kind, JM Bonard, C Emmenegger, LO Nilsson, K Hernadi, E Maillard-Schaller, L Schlapbach, L Forro, K Kern, *Adv. Mater.*, 11(15), 1285, 1999.
- [107] AM Cassell, NR Franklin, TW Tomblor, EM Chan, J Han, H Dai, *J. Am. Chem. Soc.*, 121, 7975, 1999.
- [108] KT Lau, D Hui, *Compos. B*, 33, 263, 2002
- [109] PM Ajayan, O Stephan, C Colliex, D Trauth, *Science*, 265, 1212, 1994.
- [110] J Sandler, MSP Shaffer, T Prasse, W Bauhofer, K Schulte, AH Windle, *Polymer*, 40, 5967, 1999.
- [111] S Curran, PM Ajayan, WJ Blau, DL Carroll, JN Coleman, AB Dalton, AP Davey, A Drury, B McCarthy, S Maier, A Strevens, *Adv. Mater.*, 10(14), 1091, 1998.
- [112] JN Coleman, AB Dalton, S Curran, A Rubio, AP Davey et al, *Adv. Mater.*, 12(3), 213, 2000.
- [113] MS Shaffer, AH Windle, *Adv. Mater.*, 11(11), 937, 1999.
- [114] JN Coleman, WJ Blau, AB Dalton, E Munoz, S Collins, *Appl. Phys. Lett.*, 82(11), 1682, 2003.

- [115] M Cochet, WK Maser, AM Benito, MA Callejas, MT Martinez, JM Benoit, J Schreiber, O Chauvet, *Chem. Commun.*, 1450, 2001
- [116] WK Maser, AM Benito, MA Callejas, T Seeger, MT Martinez, *Mater. Sci. Eng. C*, 23, 87, 2003
- [117] R Sainz, AM Benito, MT Martinez, JF Galindo, J Sotres, AM Baro, B Corraze, O Chauvet, AB Dalton, RH Baughman, WK Maser, *Nanotechnol.*, 16, S150, 2005.
- [118] AB Dalton, S Collins, JM Razal, E Munoz, VH Ebron, BG Kim, JN Coleman, JP Ferraris, RH Baughman, *J. Mater. Chem.*, 14, 1, 2004.
- [119] M Zhang, S Fang, AA Zakhidov, SB Lee, AE Aliev, CD Williams, KR Atkinson, RH Baughman, *Science*, 309, 1215, 2005.
- [120] YJ Kim, TS Shin, HD Choi, JH Kwon, YC Chung, HG Yoon, *Carbon*, 43, 23, 2005.
- [121] N Zhang, J Xie, M Guers, VK Varadan, *Smart Mater. Struct.*, 13, N1, 2004.
- [122] G Viswanathan, N Chakrapani, H Yang, B Wei, H Chung, K Cho, CY Ryu, PM Ajayan, *J. Am. Chem. Soc.*, 125, 9258, 2003.
- [123] R Blake, YK Gun'ko, J Coleman, M Cadek, A Fonseca, JB Nagy, WJ Blau, *J. Am. Chem. Soc.*, 126, 10226, 2004.
- [124] H Geng, R Rosen, B Zheng, H Shimoda, L Fleming, J Liu, O Zhou, *Adv. Mater.*, 14(19), 1387, 2002.
- [125] Applied Nanotechnologies, Inc.
- [126] PM Ajayan, L Schadler, C Giannaris, A Rubio, *Adv. Mater.*, 12 (10), 750, 2000.
- [127] SJV Frankland, VM Harik, GM Odegard, DW Brenner, TS Gates, *Compos. Sci. Technol.*, 63, 1655, 2003.
- [128] M Cadek, JN Coleman, V Barron, K Hedicke, WJ Blau, *Appl. Phys. Lett.*, 81(27), 5123, 2002.
- [129] TV Sreekumar, T Liu, BG Min, H Guo, S Kumar, RH Hauge, RE Smalley, *Adv. Mater.*, 16(1), 58, 2004.
- [130] AH Barber, SR Cohen, HD Wagner, *Appl. Phys. Lett.*, 82(23), 4140, 2003.
- [131] BE Kilbride, JN Coleman, J Fraysse, P Fournet, M Cadek et al, *J. Appl. Phys.*, 92(7), 4024, 2002.
- [132] E Munoz, DS Suh, S Collins, M Selvidge, AB Dalton, BG Kim, JM Razal, G Ussery et al, *Adv. Mater.*, 17(8), 1064, 2005.
- [133] JN Coleman, S Curran, AB Dalton, AP Davey, B McCarthy, W Blau, RC Barklie, *Phys. Rev. B*, 58(12), R7492, 1998.
- [134] MJ Biercuk, MC Llaguno, M Radosavljevic, JK Hyun, AT Johnson, *Appl. Phys. Lett.*, 80, 2767, 2002

- [135] R Baughman, AAPPS Bulletin, 13(4), 13, 2003.
- [136] S Kumar, TD Dang, FE Arnold, AP Bhattacharyya, BG Min et al, Macromol., 35, 9039, 2002.
- [137] RH Baughman, AA Zakhidov, WA de Heer, Science, 297, 787, 2002.
- [138] Hyperion Catalysis, Plastics Additives and Compounding, 3 (9), 20, 2001.
- [139] M Rutkofsky, R Folaron, Zyvex Corp. Application Note 9714.
- [140] M Rutkofsky, M Banash, R Rajagopal, J Chen, Zyvex Corp. Application Note 9709.

Chapter 3: Synthesis of a novel catalyst for the growth of carbon nanotubes

3.1 Introduction

The focus of this thesis is to produce freestanding carbon nanotube thin film composites. The technique of composite production developed during this work enables the position of nanotubes within a matrix to be controlled. The first step in the process is carbon nanotube growth. Growth is activated by a catalyst material. In our experiments we use a novel catalyst called poly(styrene-vinylferrocene). This copolymer is made by anionic synthesis. A detailed description of the catalyst synthesis and subsequent characterisation is given in this chapter.

3.2 Catalyst Synthesis

The transition metals iron, cobalt and nickel are the most effective catalysts for the growth of carbon nanotubes (CNTs). These catalysts are active in a variety of configurations (section 2.4.1) [1-6]. In an attempt to control the dispersion and size distribution of catalyst particles, we use a diblock copolymer containing an iron core. This is the first time a copolymer has been used as a catalyst for CNT growth. The copolymer used is poly(styrene-vinylferrocene), PS-PVF. As the name suggests, PS-PVF contains a poly(styrene) block and a poly(vinylferrocene) block (figure 1). These two polymer blocks can be covalently linked to produce a copolymer. The aim is that the poly(styrene) will act to disperse the poly(vinylferrocene) block and hence iron cores will be well distributed within the catalyst material.

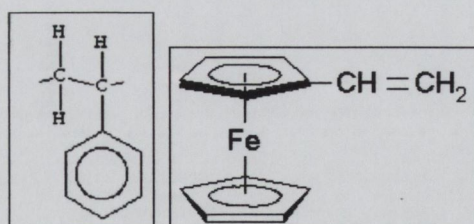


Figure 1: A styrene monomer and a vinylferrocene monomer. These are the building blocks from which PS-PVF is made. The ferrocene component contains an iron core and can thus catalyse carbon nanotube growth.

Poly(styrene-vinylferrocene) was synthesised in-house by anionic polymerisation. This involves the polymerisation of a monomer using an anionic initiator. Anionic polymerisation facilitates the production of a polymer product with a narrow molecular weight distribution. The molecular weight can be pre-determined and controlled. Monomers containing an electron-withdrawing group, such as styrene, are readily polymerised by this technique. Carbanions (δ^-) are the propagating species during anionic polymerisation. These form when the monomer (styrene in our case) attaches to the anionic initiator. The initiator we use is secondary butyllithium. During initiation of the reaction, styrene will attach onto the alkyl part of this molecule (figure 2). A by-product of carbanion formation is the formation of a metal gegenion (δ^+). Propagation of the reaction occurs as more monomer groups attach onto carbanions to form macrocarbanions. In the absence of contaminants, stable macrocarbanions form (this is called a “living polymer”). A second monomer type (vinylferrocene in our case) can then be introduced to the system. This will attach onto the styrene macrocarbanions to produce a diblock copolymer.

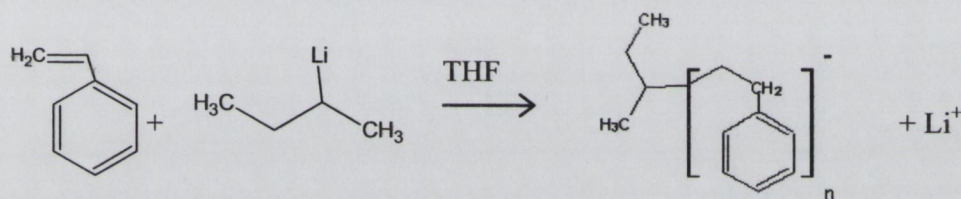


Figure 2: A styrene monomer reacts with sec-butyllithium initiator to form carbanions (δ^-) and metal gegenions (δ^+). This is the initiation stage of the anionic polymerisation reaction.

Carbanions are quickly neutralized by impurities such as water, carbon dioxide and oxygen. Therefore, the reaction must be done under inert conditions and monomers must be thoroughly purified prior to polymerisation. Polymerisation is carried out in tetrahydrofuran (THF). This must also be thoroughly purified. Figure 3 shows a reaction scheme for the anionic polymerisation. All glassware used during the polymerisation must be thoroughly cleaned and stored in an oven at 110°C prior to use. This prevents atmospheric water vapours condensing on the glassware.

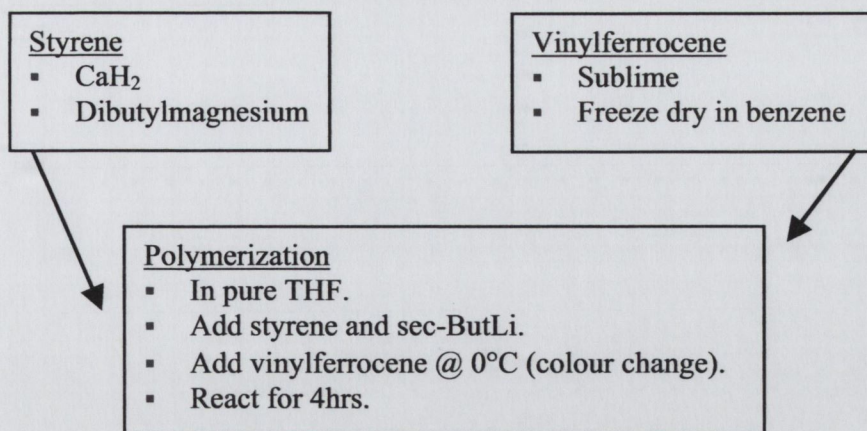


Figure 3: Reaction scheme for the anionic synthesis of the copolymer poly(styrene-vinylferrocene). Monomers are first purified. They are then polymerised in THF using sec-butyllithium as the initiator.

3.2.1 Styrene Purification

A styrene monomer was added to calcium hydride (CaH_2) powder to remove water molecules. The dehydrated styrene was then freeze-thawed to remove any dissolved gasses. Dibutylmagnesium was then added to styrene. Prior to this, the dibutylmagnesium was stirred under vacuum to remove the solvent heptane, which it is stored in. The mixture of styrene and dibutylmagnesium was stirred for two hours, under argon, to allow the dibutylmagnesium to react with any remaining impurities in the styrene. The styrene is then evaporated at 40°C into a liquid nitrogen cooled dewar leaving the larger molecules which have reacted with dibutylmagnesium behind.

3.2.2 Vinylferrocene Purification

Vinylferrocene (Aldrich, 97%) was purified by sublimation, below its melting point of 52°C . Crystals change from orange to pale yellow due to the removal of impurities. Crystals were dissolved in benzene and frozen using liquid nitrogen. Vacuum was applied and benzene was allowed to evaporate slowly as the solution thawed. Impurities are removed with the benzene as it evaporates leaving pure vinylferrocene behind.

3.2.3 Tetrahydrofuran Purification

Tetrahydrofuran (polarity=0.207, relative to water) was used as the solvent due to its relatively low polarity. The rate of polymerisation is slower in a non-polar solvent thus allowing greater control over the reaction. THF was refluxed in sodium and benzophenone for several days. The sodium removes water impurities and benzophenone acts as an indicator. Benzophenone will turn deep purple in the presence of pure THF. Purified THF (100ml) was removed from the reflux apparatus and freeze-thawed to remove dissolved gasses. Sec-butyllithium was added drop by drop to THF at -75°C until a pale green colour persisted. A bath of dry ice was used to maintain the low temperature. Sec-butyllithium reacts with impurities. A persistent pale green colour indicates that all impurities have reacted. THF was then allowed to return to room temperature where the colour disappeared. Purified THF can then be collected.

3.2.4 Polymerisation

Styrene (5ml) was added to the THF solvent. Sec-butyllithium ($250\mu\text{L}$, see calculations in section 3.2.5) was added to the styrene/THF at -75°C . The initiator adds an anion across the vinyl double bond in styrene to create a carbanion (figure 2). A relatively highly electropositive initiator is needed to polymerise styrene due to low electronegativity of the phenyl side group. The solution became pale orange due to the formation of styrene carbanions. The styrene was left to polymerise for 30 minutes.

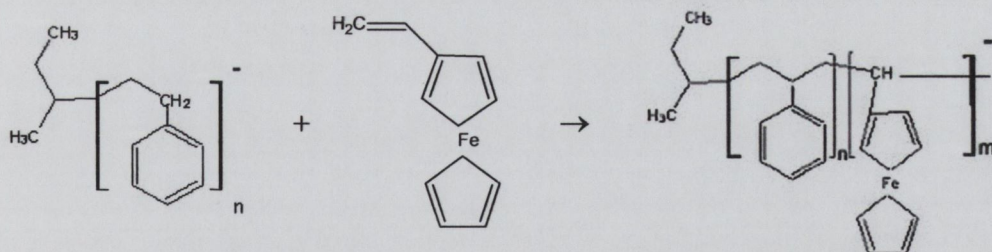


Figure 4: Vinylferrocene was added to the styrene carbanions to form the copolymer structure above.

Purified vinylferrocene (0.98g) was then added to the mixture (figure 4) at 0°C . The temperature was maintained at 0°C using an ice-bath. The reaction turned a deep red

colour. The system was left to react for four hours and was then killed using purified butanol. The polymer was then precipitated in methanol and collected by filtration.

3.2.5 Amount of Initiator required for a Specific Target Molecular Weight

We aim to produce a styrene block of number average molecular weight 14,000g/mol. This weight was chosen to maintain sufficient length of the polymer chain, while also preventing it from becoming too long and viscous in solution. The amount of initiator required to produce a target molecular weight can be calculated quite simply. Basically, one mole of initiator produces one mole of carbanions. Therefore, the amount of initiator is inversely proportional to the target molecular weight (equation 1).

$$M_{PS} / M_I = M_w(PS) / M_w(ST) \quad \text{Equation 1.}$$

$$M_{PS} = \text{moles of polystyrene} = \text{mass polystyrene} \div M_w \text{ polystyrene}$$

$$\text{Mass} = \text{volume} \times \text{density} = 5\text{ml} \times 0.909\text{g/ml}$$

$$M_w \text{ polystyrene} = 104.15\text{g}$$

$$M_I = \text{moles of initiator} = \text{molarity of initiator} \times \text{number of litres used}$$

$$M_w(PS) = \text{target molecular weight of polystyrene}$$

$$M_w(ST) = \text{molecular weight of styrene monomer}$$

$$\therefore \frac{(5\text{ml} \times 0.909\text{g/ml}) \div 104.15\text{g}}{1.3\text{M} \times x\text{L}} = \frac{14,000\text{g}}{104.15\text{g}}$$

$x\text{L} = 250\mu\text{L}$ of initiator required for a target molecular weight of 14,000g

3.3 Catalyst Characterisation

Several characterization techniques were used to determine the molecular weight, composition and decomposition temperature of the poly(styrene-vinylferrocene) copolymer catalyst synthesized. These include gel permeation chromatography, nuclear magnetic resonance, thermal gravimetric analysis and Raman spectroscopy.

3.3.1 Gel Permeation Chromatography

Gel permeation chromatography (GPC), also known as Size Exclusion Chromatography, is used to determine the molecular weight and molecular mass distribution of a polymer. The polymer sample is dissolved in a suitable solvent and passed through a column tightly packed with micro-porous beads of different pore sizes. The polymer molecules in dilute solution occupy space equivalent to their hydrodynamic volume. As they pass through the column, molecules get drawn into pores of size greater than or equal to their own hydrodynamic volume due to the force of diffusion. Larger molecules, unable to penetrate the pores, continue in the solvent flow and exit first. Smaller molecules, which pass into many pores, exit later from the column. Thus the technique grades molecules according to size.

A detector at the end of the column monitors the eluent and compares it with a calibrated standard (sample of known molecular weight) to produce a spectrum which reveals the molecular weight distribution of the polymer sample. From this spectrum it is possible to calculate the weight average, number average and higher order molecular weights of the sample. From these values the polydispersity of a polymer sample can be calculated.

The beads used to pack the column are made from either porous glass or silica where an aqueous solvent is to be used. Beads made from crosslinked styrene-divinylbenzene are used with non-polar solvents such as tetrahydrofuran or toluene. Due to advances in the stability of the bead structures, slightly polar solvents such as dimethylformamide can now also be used. This makes GPC of polymers such as Nylon and polyethylene possible. Previously polymers, which are insoluble in non-polar solvents, would need to be studied at higher temperatures to increase their solubility in the solvent. Increasing the temperature of course has an effect on the hydrodynamic volume and hence very careful calibration of the system is necessary.

The column is made from stainless steel and is typically 7.5mm in diameter and 300-600mm long. The solvent must flow through the column at a steady state. The polymer sample is introduced to the flow in very small, controlled amounts so as not to disturb the flow dynamics of the system (typically 1ml/min). Very low concentrations of the polymer solution are required for GPC which is of course an advantage of the technique.

The effective range of molecular weights, which can be measured by GPC, depends on the range of the pore sizes within the column. Typically pore sizes range from 0.5-10⁵ nm corresponding to a molecular weight range of <100g/mol to 1x10⁷g/mol. GPC however cannot be used to differentiate between branched and linear chains of the same molecular weight.

3.3.1.1 Catalyst Characterisation by GPC

A Waters Breeze GPC was used to determine the molecular weight distribution of the synthesised poly(styrene-vinylferrocene) copolymer. The GPC is connected to a Waters 2414 refractive index detector. A change in the refractive index of the eluent is indicative of the presence of polymer molecules. The magnitude of the change represents the amount of polymer present. Hence the GPC plots a change in refractive index against elution time. A solution of 0.25wt% polymer was made in tetrahydrofuran. The solution was filtered using a 0.2µm syringe filter and injected into the GPC apparatus using a 20µL syringe. The flow rate was 1ml/min and a Styragel[®] GPC column was used.

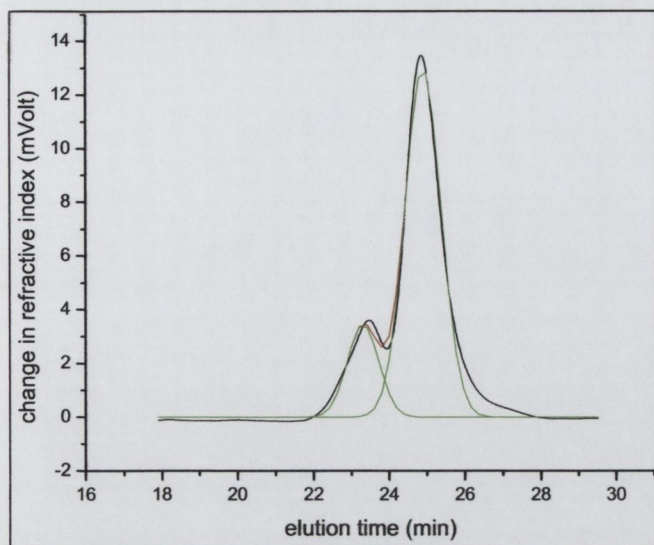


Figure 5: GPC spectrum of the synthesised PS-PVF copolymer shows two peaks.

Two peaks were observed in the GPC spectrum obtained indicating that two distinct molecular weights are present in our polymer (Figure 5). This suggests that the polymer is in fact a blend of a PS-PVF copolymer mixed with a polystyrene homopolymer. As larger molecules pass through a GPC column faster, we can assign the first peak to the copolymer fraction of the blend. Consequentially, the second peak must correspond to the polystyrene fraction. It appears that not all of the styrene macrocarbanions were able to attach onto vinylferrocene molecules during polymerisation. Perhaps tiny amounts of impurities caused the termination of some of the styrene carbanions before they were accessed by the vinylferrocene. Also, self-termination by other carbanions may have occurred during the reaction. For these reasons anionic polymer synthesis is an extremely tedious and difficult polymerisation technique.

3.3.1.2 Calculation of the Copolymer Blend Composition

The ratio of the peak areas in the GPC spectrum enables the percentage copolymer contained in the blend to be calculated.

The GPC spectrum (figure 5) gives a peak area of 15.48 arbitrary units (a.u.), corresponding to the polystyrene (PS) homopolymer, and 3.57 a.u. corresponding to the PS-PVF copolymer. The R^2 value for this peak fit was 0.99.

Therefore,

$$\%PS = 15.48 / (15.48 + 3.57) * 100 = 81.3\%$$

Table 3.1: Composition of the synthesised copolymer blend.

	PS homopolymer	PS-PVF copolymer
Percentage	81.3%	18.7%
M_n	16,366g/mol	34,169g/mol

Elution time is compared to a well-calibrated standard to obtain the corresponding molecular weight (table 3.1). The number average molecular weight of the polystyrene homopolymer is 16,366g/mol. Our target weight for the polystyrene fraction was 14,000g/mol. This indicates that we added slightly too much initiator. We added 250 μ L but, 218 μ L would be the amount required for a molecular weight of 16kg/mol. Due to the highly reactive nature of the initiator, it is possible that it became partially deactivated while being stored. This would explain the slightly higher molecular weight obtained. The molecular weight is in the region of the targetted weight and it's accuracy is not crucial to our experiments. For the poly(styrene-vinylferrocene) diblock copolymer the molecular weight is 34,169g/mol.

An estimate of the percentage of vinylferrocene (the iron containing part of the polymer) is possible using the data in Table 3.1.

Molecular weight of the vinylferrocene component = $34,169 - 16,366 = 17,803$

Fraction vinylferrocene in the copolymer blend = $17,803/34,169 * 18.7\% = 9.7\%$

This is a good estimate. However, a more accurate value is obtained from NMR.

3.3.2 Nuclear Magnetic Resonance

Nuclear magnetic resonance (NMR) is a powerful technique for determining the structure of organic compounds [7]. NMR can detect nuclei with non-zero nuclear spin, in our case ^1H which has a spin quantum number (I) of $\frac{1}{2}$. There is a magnetic moment associated with the nucleus. This depends on the direction of spin (Equation 2).

$$\mu = \gamma \hbar m_I \quad \text{Equation 2.}$$

μ = magnetic moment

γ = magnetogyric ratio of nucleus

$\hbar m_I$ = component of spin angular momentum ($= \pm 1/2\hbar$ for ^1H)

In the absence of an external magnetic field, these magnetic moment vectors are randomly aligned and spinning nuclei all possess the same energy. However when a magnetic field (\mathbf{B}_0) is applied, the magnetic moments become aligned along the field axis. Some nuclear spins align parallel and some align anti-parallel to \mathbf{B}_0 . The lower energy state is the one aligned parallel and as a result it is the more populated of the two states. Relative populations are determined by Boltzmann distribution (equation 3).

$$N_\beta / N_\alpha = \exp(-\Delta E/kT) \quad \text{Equation 3.}$$

N_β = number of spins in the higher energy state

N_α = number of spins in the lower energy state

ΔE = energy gap between α and β states

T = temperature

k = Boltzmann constant

Irradiation of the sample with a frequency corresponding to the spin state separation energy causes nuclei to be excited into the higher (β) state. Absorption only occurs at certain frequencies. The frequency at which a nucleus resonates is known as its Larmor frequency (ν_L).

$$\Delta E = E_\beta - E_\alpha = h\nu_L \quad \text{Equation 4.}$$

However in \mathbf{B} , the $2I+1$ orientations of a nucleus have different energies (E_{m_I}).

$$E_{m_I} = -\mu_z B = -\gamma\hbar m_I B$$

$$\Rightarrow \Delta E = 1/2\gamma\hbar B - (-1/2\gamma\hbar B) = \gamma\hbar B$$

$$\text{So, } \gamma\hbar B = h\nu_L$$

Equation 5.

For resonance to occur, radiation of frequency ν_L must excite the sample. At this frequency resonance will occur between the applied radiation and the nuclear spins. For a 12 T magnetic field resonance occurs at 500MHz, according to equation 5. The Larmor frequency generally lies in the radio frequency range (60-950 MHz). The resonance frequencies of a sample can be used to identify the structure of a material.

The gap between energy levels (and hence resonance frequency) depends on the chemical environment of a nucleus. Additional orbital angular momentum is induced by neighbouring ^1H nuclei. This implies that a small additional field (δB) exists at each nucleus.

$$\delta B = -\sigma B$$

Equation 6.

σ = shielding constant

The strength of a local field (B_{loc}) depends on the electronic structures near the magnetic nucleus of interest according to equation 7. Each nucleus contributes to local field and hence modifies the resonance of neighbouring nuclei. This results in the fine structure (line splitting) observed in NMR spectra. Singlets are split into multiplets by neighbouring nuclei. The relative intensities of lines in the multiplet can be determined using Pascal's triangle.

$$B_{loc} = B + \delta B = (1-\sigma)B$$

Equation 7.

$$\Rightarrow \nu_L = (1-\sigma)\gamma B / 2\pi$$

Therefore, nuclei experience resonance at different frequencies (ν_L) depending on their nuclear environment. The resonant frequency depends on the external field applied. Therefore, it is more convenient to convert to a standard field-independent value called the chemical shift (Equation 8). A NMR spectrum plots chemical shifts rather than resonant frequency against peak intensity.

$$\delta = (\nu_{\text{sample}} - \nu_{\text{TMS}}) \times 10^6 / \nu_{\text{TMS}} \quad \text{Equation 8.}$$

ν_{sample} = peak frequency of sample

ν_{TMS} = peak frequency of TMS standard

δ = chemical shift, measured in parts per million (ppm)

The standard used is TMS (tetramethylsilane, $\text{Si}(\text{CH}_3)_4$). TMS contains twelve equivalent protons and hence has only one intense peak for ^1H resonances. This peak is set at 0 ppm. Shifts from this standard are the same for all nuclei in an identical chemical environment. The ratio of peak intensities gives the ratio of the number of ^1H 's in each environment.

In modern NMR, the magnetic field applied is circularly polarised in the x-y plane and rotates at the Larmor frequency. Therefore, nuclei precessing at the same Larmor frequency (about the z plane) experience an effective steady field. Therefore the magnetisation vector (\mathbf{M}) precesses into the x-y plane and so a 90° pulse rotates in x-y at the Larmor frequency. This generates a signal. A broad band pulse is used to excite all frequencies simultaneously. The magnitude of the magnetisation vector decays exponentially with time (called free induction decay, FID). Detected signals give information about the different Larmor frequencies present in the sample and there are multiple harmonic components in a FID signal. Fourier transforms are used to obtain a frequency domain spectrum with each line representing ν_L of a particular nucleus. The spin-lattice relaxation time T_1 gives the time it takes for the magnetisation vector to relax back to the z-direction. This occurs as the populations of the α and β states revert to their equilibrium values and is an exponential decay. Also, randomisation of spin directions occurs with a time constant T_2 called the spin-spin relaxation time. T_2 results in spectral broadening (equation 9).

$$\Delta\nu_{1/2} = 1 / \pi T_2 \quad \text{Equation 9.}$$

$\Delta\nu_{1/2}$ = the spectral width at the half maximum.

Inhomogeneous external magnetic fields also contribute to spectral broadening. This is expressed in terms of the effective spin-spin relaxation time (T_2^*).

$$T_2^* = 1 / \pi \Delta\nu_{1/2} \quad \text{Equation 10.}$$

Samples are usually rotated in a magnetic field to minimise spectral broadening.

3.3.2.1 Catalyst Characterisation by NMR

NMR tubes were cleaned with THF and placed in the oven at 60°C for 30 minutes to remove any residual volatiles. Poly(styrene-vinylferrocene), 10mg, was added to the tube and dissolved using 1ml of deuterated chloroform, CDCl_3 . The tube was capped and placed in a Varian Unity 500 NMR. The tube was spun to average out any variations in the magnetic field.

In the spectrum obtained for our poly(styrene-vinylferrocene) sample, a sharp peak at 0ppm corresponds to the TMS standard and another sharp peak at 7.28ppm corresponds to traces of non-deuterated chloroform, CHCl_3 (figure 6). The presence of some water is indicated by the sharp peak at 1.6ppm. The sharp spike at 3.7ppm indicates the presence of some unpolymerised material. Monomers exhibit fine splitting in an NMR spectrum whereas polymer have much broader features. This is due to a short T_1/T_2 .

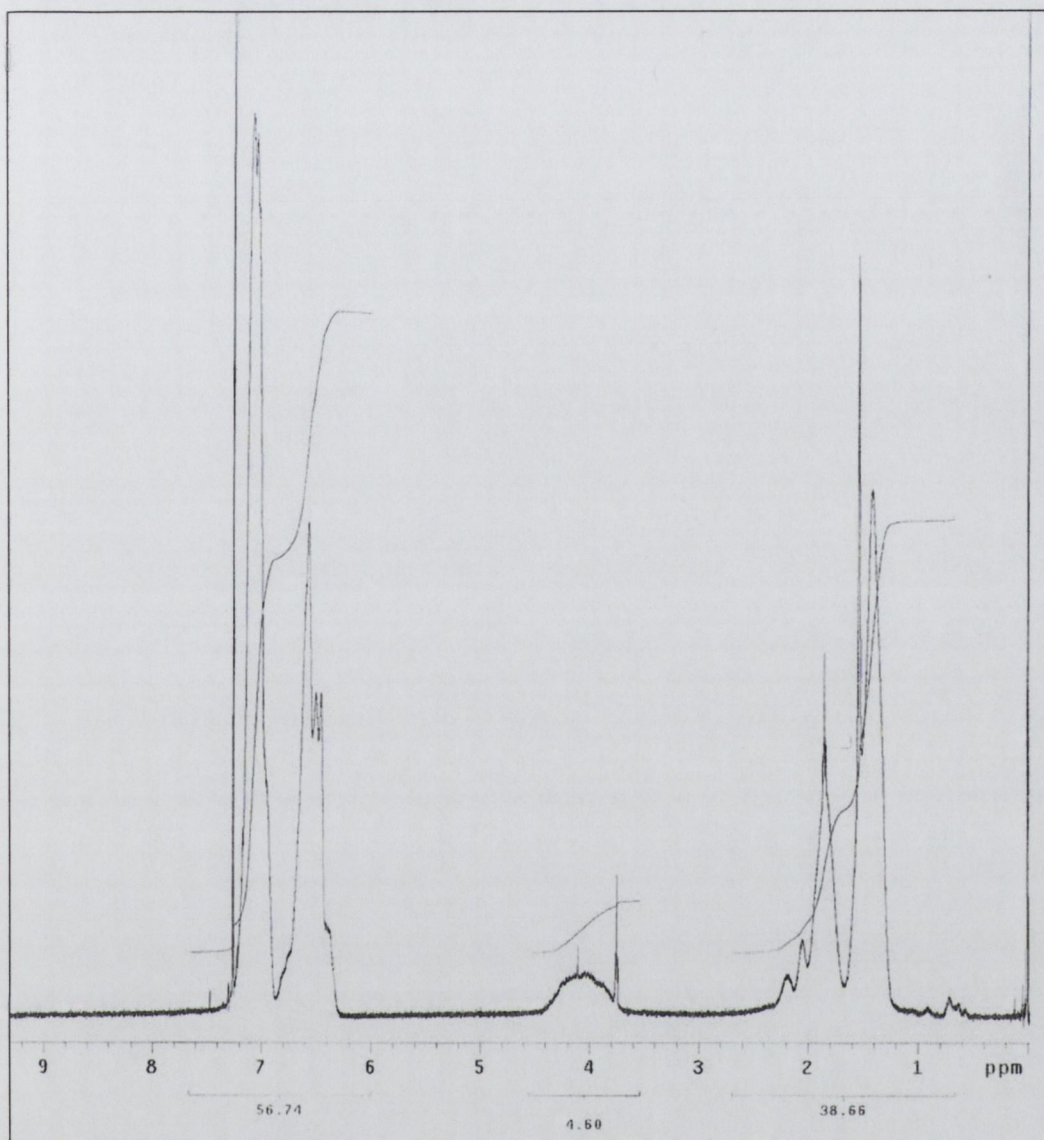


Figure 6: A NMR spectrum of the poly(styrene-vinylferrocene) copolymer blend.

In styrene, there are eight hydrogen atoms in five different environments (figure 7). Five of these are aromatic and three are aliphatic. Each particular hydrogen environment corresponds to a peak in the NMR spectrum. Peaks at 1.4ppm and 1.8-2.1ppm are due to aliphatic ^1H resonances. Peaks at 6.4-6.6ppm and 7.1ppm are assigned to aromatic ^1H 's. The ratio of peak intensities can be used to calculate the number of ^1H 's in each particular chemical environment. These peaks are all present in our NMR spectrum (Figure 6).

Position	δ ^1H (ppm)
1,2	7.1
3	6.4-6.6
4	1.8-2.1
5	1.4

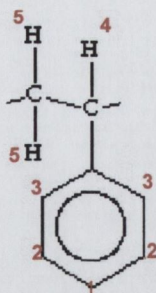


Figure 7: The styrene molecule. Each hydrogen atom, numbered 1 to 5, is in a different environment. Hydrogen atoms in an identical environment are labelled with the same number.

Peaks in the range 3.6-4.4ppm are not expected for polystyrene and indicate the presence of another component. These peak positions are consistent with resonances in the cyclopentadienyl ring. These peaks can thus be assigned to the aromatic hydrogens in ferrocene. The numbers below each resonance peak (Figure 6) indicate the relative signal strengths and can be used to calculate the percentage vinylferrocene contained in the polymer.

3.3.2.2 Calculation of Styrene-to-Vinylferrocene Ratio in the Copolymer

Method 1: The ratio of the vinylferrocene signal strength to the styrene signal strength (calculated by the NMR computer software) gives us the amount of vinylferrocene present.

$$4.60/56.74 * 100 = \mathbf{8.11\% \text{ vinylferrocene}}$$

Method 2: To calculate the percentage of each component present, the NMR spectrum can be integrated. Integrals divide peaks into ratios determined by the number of H's in identical environments.

Measure the ratio of integral traces;

$$\text{Aromatic styrene (5 H's) : Aromatic ferrocene (9H's)} = 10.4 : 0.8$$

(Values measured in cm to an accuracy of $\pm 1\text{mm}$)

$$\frac{(10.4/5) * M_0^{st}}{[(10.4/5) * M_0^{st}] + [(0.8/9) * M_0^{vf}]} = 0.9199 = \mathbf{92\% \text{ polystyrene}}$$

M_0^{st} = molecular weight of styrene = 104g

M_0^{vf} = molecular weight of vinylferrocene = 212g

Therefore, approximately 8% of the polymer is comprised of vinylferrocene, which agrees with our first calculation (section 3.3.1.2). The mass percentage of iron in vinylferrocene is 26.4% (56/212). The amount of **iron** in the polymer blend is thus estimated to be **2.1%** (0.264 * 8%). The remainder of the polymer consists of carbon and hydrogen, which are unstable at elevated temperatures.

3.3.3 Thermal Gravimetric Analysis

Thermal gravimetric analysis (TGA) is used to determine the thermal stability of a material. It records the change in sample mass over a particular temperature range. As the sample is heated the mass decreases. Losses at low temperatures can be due to the evaporation of absorbed moisture or other volatile additives. At higher temperatures, weight loss is due to the degradation and eventual decomposition of the sample.

TGA can be performed under an inert atmosphere such as nitrogen or, in a reactive atmosphere of oxygen. Heating in the presence of oxygen allows the oxidative stability of the sample to be determined. Heating under an inert atmosphere ensures that no oxidation occurs. Where sample temperatures are high enough full decomposition of the sample can be achieved. Any remaining weight can be used to determine the percentage of fillers or stabilisers, which do not decompose. Hence, TGA can be used as a method to determine the bulk composition of the sample. It can also be used to determine the materials present in a sample by plotting the derivative of weight loss against temperature. This gives derivative thermogravimetric analysis which identifies materials according to their peak degradation temperature.

TGA is also used to measure properties such as drying, re-hydration and the evolution of additives. Its primary function however remains in monitoring structural decomposition and it can do this, using only microgram quantities of the sample.

3.3.3.1 Thermal Analysis of the Synthesised Copolymer

Polymers generally decompose at temperatures in the region of 400°C. The poly(styrene-vinylferrocene) polymer we have synthesised is to be used as a catalyst for carbon nanotube growth. This is frequently carried out at elevated temperatures in the region of 600-900°C [8-10]. Although Silva et al have demonstrated growth at temperatures as low as room temperature, we do not have the capabilities to replicate their growth conditions [11]. Therefore, we need to confirm that catalyst particles will remain at temperatures in excess of 600°C.

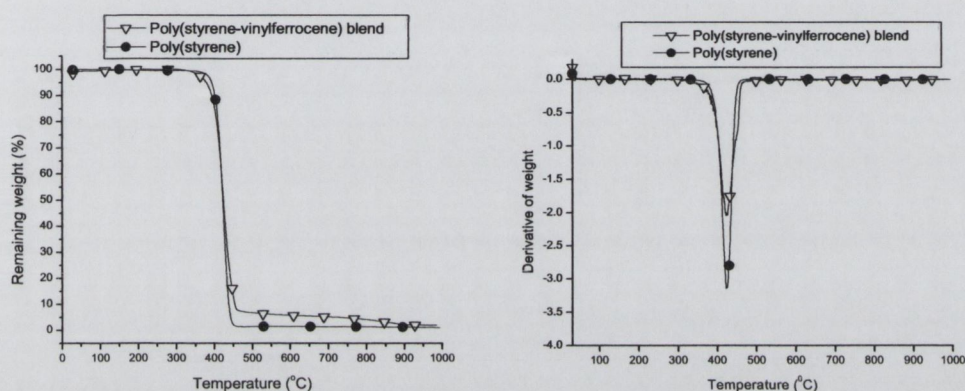


Figure 8: The TGA curve for poly(styrene-vinylferrocene) copolymer blend compared with a curve for polystyrene homopolymer. The plot on the right shows the derivative TGA curve.

Decomposition curves were obtained using a Mettler-Toledo TGA/SDTA851 (figure 8). Samples were heated from 25-1000°C at 10°C/minute while flowing nitrogen gas at 40ml/minute. Decomposition of the PS-PVF copolymer occurred in the region from 360°C to 460°C. Over this temperature range 91.96% of the PS-PVF sample weight was lost. This compares with 97.86% weight loss for the PS homopolymer across the same temperature region. The derivative of the TGA plots shows peak decomposition temperatures more clearly. This peak is at 425°C for both polymers. At elevated temperatures more copolymer than homopolymer remains. This is due to the vinylferrocene component or, more specifically iron. At 700°C, 5.09% copolymer remains compared to only 1.37% homopolymer. By 900°C, this has decreased to 2.17% compared to 1.17% (figure 9).

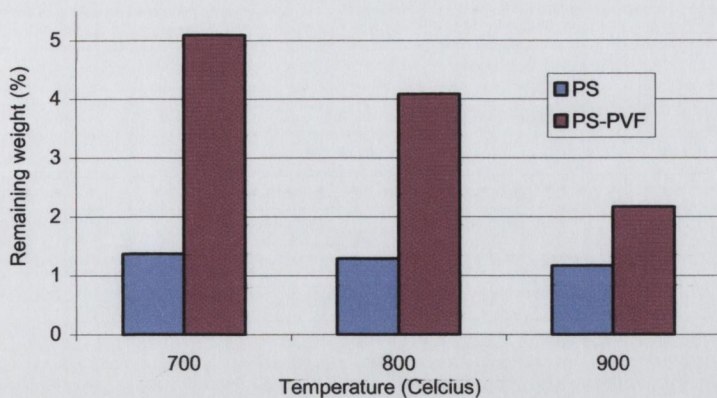


Figure 9: Comparison of remaining PS homopolymer and PS-PVF copolymer at high temperatures.

We can safely assume most of the carbon and hydrogen present in the copolymer blend have decomposed at higher temperatures leaving only iron remaining. This iron is to be the catalyst for carbon nanotube growth.

3.3.4 Raman Spectroscopy

Raman spectroscopy is a fingerprinting technique used to identify the composition of a sample material. When monochromatic light is shone on a sample, not all light is scattered at the same frequency as the incident light. A small amount is (Raman) shifted to a higher or lower frequency. This Raman shift gives information about the low frequency phonon modes present in the sample. This phenomenon was first observed by the Indian scientist Sir C.V. Raman [12]. He was awarded the Nobel Prize in 1930 for his discovery.

Raman spectroscopy involves illuminating a sample with laser light. The incident photons can interact with the sample on a molecular level by either absorption or scattering. The majority of incident light is elastically (Rayleigh) scattered and the wavelength of the scattered light remains close to that of the incident beam. Some light is however inelastically (Raman) scattered. The incident photons exchange energy with molecules in the sample. Molecules subsequently decay to a vibrational state above or below the initial energy state. The position of molecular vibrational energy levels can be determined using equation 11.

$$E_n = (n+1/2)\hbar\omega \quad \text{Equation 11.}$$

$$n = 0, 1, 2, \dots$$

$$\omega = \text{angular frequency } (2\pi f)$$

Incident phonons interact with the electron cloud of a molecule. The deformation of the electron cloud depends on the polarizability (α) of the molecule. The greater α , the greater the intensity of the Raman peak. Therefore for a sample to be Raman active, its polarization must change during interaction with an external field. The induced dipole moment depends on the strength of the applied field according to equation 12. Samples where the dipole moment does not change during vibration in an external field are Raman inactive. Vibrational energy change is represented by a frequency shift. Raman shift is therefore the difference in energy between the incident and scattered photon.

$$\mu = \alpha E \quad \text{Equation 12.}$$

μ = induced dipole moment
 α = polarisability of the molecule
 E = applied electric field

Rayleigh scattering is typically of higher intensity than Raman scattering and any output laser light close to the wavelength of the input laser line must be filtered. Only Raman scattered light eventually falls on the detector. Fourier transforms are used to separate the detected signal into its individual frequencies and hence produce a Raman spectrum.

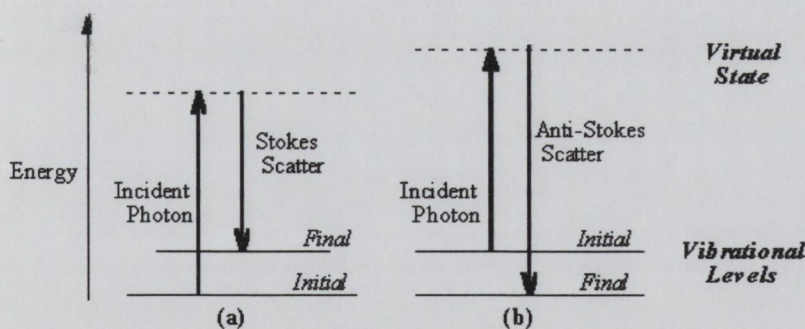


Figure 10: Energy level diagram for Raman scattering; (a) Stokes Raman scattering and (b) anti-Stokes Raman scattering.

An up- or down- Raman shift depends on whether the sample has lost or gained energy. Down-shifted components are Stokes and up-shifted components are anti-Stokes lines

(figure 10). Anti-Stokes lines result from incident radiation interacting with vibrational modes already in the excited state (stimulated emission). The modes decay releasing energy of a higher frequency than the incident radiation. A Raman spectrum is a plot of the detected number of photons versus the Raman shift in wavenumbers (equation 13).

$$\nu = 1/\lambda_{\text{incident}} - 1/\lambda_{\text{scattered}} \text{ (Units: cm}^{-1}\text{)} \quad \text{Equation 13.}$$

ν = wavenumber

$\lambda_{\text{incident}}$ = wavelength of incident light

$\lambda_{\text{scattered}}$ = wavelength of scattered light

Stokes shifts therefore correspond to up-shifted wavenumbers and anti-Stokes to downshifted. The Stokes shift is of higher intensity as the majority of modes are in the ground state at room temperature, as predicted by Boltzmann distribution. At room temperature vibrational wavenumbers lie above 200cm^{-1} . All materials have characteristic phonon modes and hence can be identified by Raman spectroscopy. Each peak in the spectrum corresponds to a particular molecular bond motion within the sample.

Raman spectroscopy is a non-destructive technique, no pre-treatment of samples is necessary and the presence of water has no effect on the spectra obtained. Water is strongly polar and hence the polarizability does not change as the molecules vibrate. Strong Raman scatterers generally have distributed electron clouds such as pi-bonds which are easily polarised. This makes Raman the ideal tool for characterising organic systems. The main limitation of Raman is interference from fluorescence, where high-energy photons are absorbed and re-emitted at lower frequencies releasing energy for molecular vibrations. Raman spectroscopy is nevertheless widely used technique in any modern polymer lab.

3.3.4.1 Raman Spectroscopy of the Synthesised Copolymer

A spectrum of poly(styrene-vinylferrocene) was obtained using a Renishaw Ramascope. The machine was first calibrated using a silicon wafer. Silicon should produce a single peak at 520cm^{-1} . This peak position is used to calibrate the instrument. To obtain a spectrum of poly(styrene-vinylferrocene), the copolymer powder was compressed into a flat pellet and placed on a glass microscopy slide. A white light microscope was used to focus on the sample. We then switched to an argon laser line ($\lambda = 514.5\text{nm}$), which is used to excite the sample. The time of the scans and the number of accumulations can be

adjusted to minimise noise in the spectrum. Generally we use 30 seconds per scan and take 4 accumulations but this can vary. Raman spectroscopy is done in the dark to avoid interference from polychromatic light.

Raman spectra obtained for the synthesised poly(styrene-vinylferrocene) and a polystyrene homopolymer can be compared to reference spectra (Appendix B). Dominant peaks for polystyrene are expected at 620, 1001, 1600, 2903 and 3165 cm^{-1} (Appendix B). For vinylferrocene dominant peaks should be located at 1055, 1105, 1460, 1475, 1630, 3080 and 3103 cm^{-1} (Appendix B). Vinylferrocene however is a small component of our synthesised copolymer (previously calculated to be 8%). Therefore we expect a Raman spectrum for the poly(styrene-vinylferrocene) to be dominated by characteristic polystyrene peaks. Indeed when we superimpose spectra of PS-PVF copolymer and PS homopolymer we see that they are almost identical (figure 11). Principal peaks common to both spectra are located at 615 cm^{-1} (can be assigned to a CH_2 rocking mode), 795 cm^{-1} (a monosubstituted benzene ring in vibration), 1001 cm^{-1} (benzene ring breathing mode), 1025 cm^{-1} (in plane CH deformation substituted on benzene), 1194 cm^{-1} (CH bend on benzene), 1450 cm^{-1} (CH_2 bending), 1602 cm^{-1} (C=C benzene ring stretch), 2846 cm^{-1} (aliphatic CH_3 stretch) and higher peaks at 2905, 3051 and 3093 cm^{-1} (all C-H stretches).

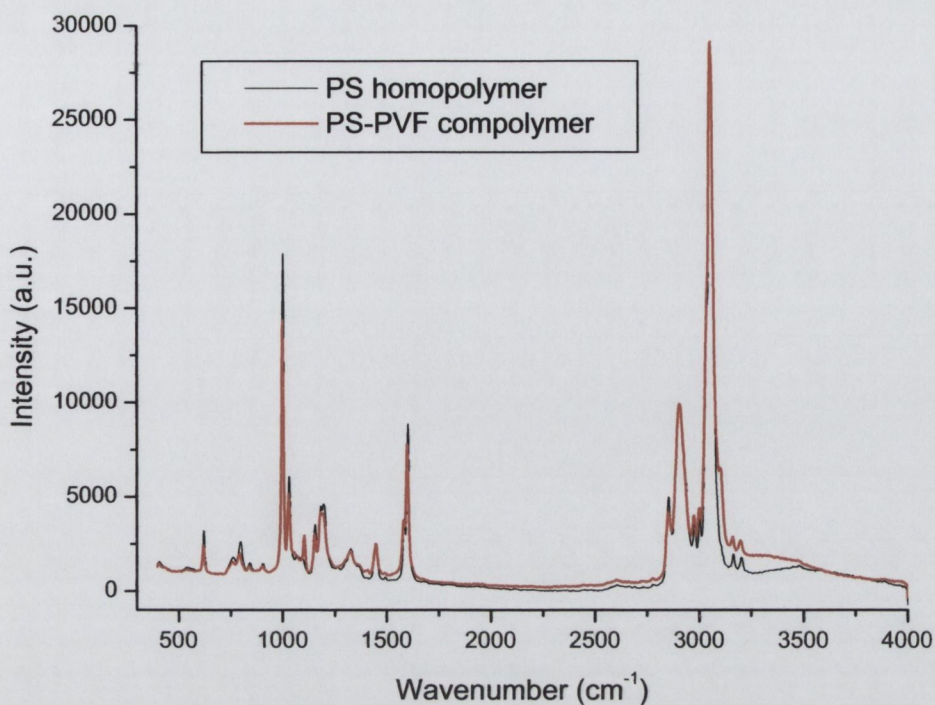


Figure 11: Raman spectrum of poly(styrene-vinylferrocene) superimposed on a spectrum of polystyrene homopolymer. The intensities of the spectra were adjusted for comparative purposes.

On closer inspection we see some differences between the two spectra (figure 12). The most obvious differences are distinct peaks at 1105 cm^{-1} and 3106 cm^{-1} (see arrows) for the copolymer. These peaks are absent for polystyrene. A peak at 1105 cm^{-1} is the most intense peak on a vinylferrocene Raman spectrum. It is due to a cyclopentadienyl ring stretch. There is no peak at this position for polystyrene. Therefore the presence of this peak is an indication that vinylferrocene is present [13]. The peak at 3106 cm^{-1} is due to the stretching of a C-H attached to cyclopentadienyl ring. There are also more subtle peak differences at 1054 cm^{-1} (due to a cyclopentadienyl ring plane deformation) and at 1413 cm^{-1} (due to a cyclopentadienyl ring stretch). We also notice slight variations in peak positions and intensities between the two spectra.

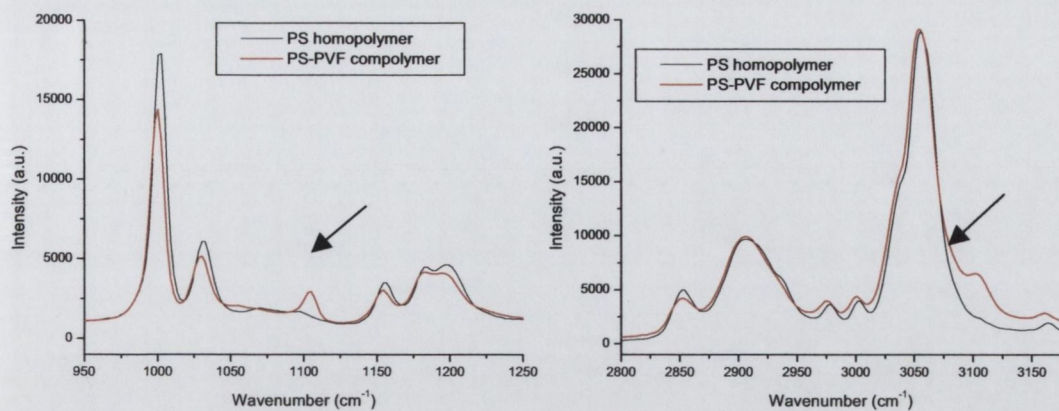


Figure 12: Closer inspection highlights differences between the two spectra. Additional peaks are present at 1105cm^{-1} and 3106cm^{-1} .

The Raman spectrum obtained for the copolymer is further evidence that what we have synthesised is not merely pure polystyrene but that a vinylferrocene component is also present.

3.4 Conclusion

In this chapter we have outlined how poly(styrene-vinylferrocene) was synthesised by anionic polymerisation. Characterisation revealed that we in fact produced a copolymer blend containing 81% polystyrene homopolymer and 19% poly(styrene-vinylferrocene). The iron content of the polymer blend was calculated to be 2.1%. This copolymer was demonstrated to be more stable than polystyrene at elevated temperatures with 5% of the copolymer remaining at 700°C . This can be assumed to be iron and it is this that we are interested in as a catalyst for carbon nanotube growth.

3.5 References

- [1] OA Nerushev, S Dittmar, RE Morjan, F Rohmund, EEB Campbell, *J. Appl. Phys.*, 93(7), 4185, 2003.
- [2] W Kim, HC Choi, M Shim, Y Li, D Wang, H Dai, *Nano Lett.*, 2(7), 703, 2002
- [3] S Huang, L Dai, AWH Mau, *Adv. Mater.*, 14 (16), 1140, 2002
- [4] JM Bonard, P Chauvin, C Klinke, *Nano Lett.*, 2 (6), 665, 2002.
- [5] R Sen, A Govindaraj, CNR Rao, *Chem. Phys. Lett.*, 267, 276, 1997.
- [6] S Lastella, YJ Jung, H Yang, R Vajtai, PM Ajayan, CY Ryu, DA Rider, I Mannners, *J. Meter. Chem.*, 14, 1791, 2004.
- [7] Felix Bloch and Edward Mills Purcell, Nobel Prize in Physics (1952)
- [8] R Seidel, GS Duesberg, E Unger, AP Graham, M Liebau, F Kreupl, *J. Phys. Chem. B*, 108, 1888, 2004
- [9] BQ Wei, R Vajtai, Y Jung, J Ward, R Zhang, G Ramanath, PM Ajayan, *Nature*, 416, 495, 2002.
- [10] W Kim, HC Choi, M Shim, Y Li, D Wang, H Dai, *Nano Lett.*, 2(7), 703, 2002
- [11] BO Boskovic, V Stolojan, RUA Khan, S Haq, SRP Silva, *Nature Materials*, 1, 165, 2002
- [12] CV Raman, *Indian J. Phys.*, 2, 387, 1928
- [13] G Davidson, *Organometallic Chem. Rev. A*, 8, 303-350, 1972

Chapter 4: Catalyst Patterning by Soft Lithography

4.1 Introduction

In the previous chapter we described the synthesis of the diblock copolymer poly(styrene-vinylferrocene). This material is to be used as a catalyst for carbon nanotube growth. Where the catalyst is patterned onto a substrate, it is possible to grow CNT arrays from specific locations [1-3]. Materials can be patterned onto substrate surfaces using a variety of techniques. Commonly used techniques include photolithography and electron beam deposition [4-5]. A less expensive, and more convenient, patterning technique is soft lithography. This simple process transfers a pattern onto a substrate surface using a moulded elastomer stamp [6]. The material to be deposited onto the substrate is dissolved in solution and transferred to the surface using the stamp. The shape and dimensions of the moulded elastomer can be easily modified for a variety of pattern geometries.

4.2 Generating a Master Template

The elastomer stamps used during soft lithography patterning are generated by replica moulding from a master. A single master can be used numerous times to cast many stamps. This has no damaging effects on the master. Masters are generated by either by photolithography or electron-beam lithography [7]. The first step in the process is to design the required pattern.

4.2.1 Mask Design

Master templates are generally etched from silicon wafers. We use photolithography to pattern a silicon template. The silicon is covered with a layer of photoresist and exposed to UV light through a chrome-patterned quartz mask (section 2.4.3). This allows the pattern on the mask to be transferred to the substrate below. For our experiments we decided to use grid patterns. These were mapped out using Kic 2.4 software [8]. Using the software, the three-inch-square mask template was divided into fifteen sections of size 1.5cm x 2.5cm. Seven of these sections were patterned with 5 μ m wide gridlines. These lines were separated by incremental spacings from 2 μ m to 75 μ m. Another seven sections were patterned with 2 μ m wide gridlines. Spacings between the 2 μ m wide lines were incremental

from 1 μm to 30 μm. These incremental spacings are identified in table 1. The final section was patterned with a logo.

Table 4.1: Dimensions of grid patterns

Cell #	1	2	3	4	5	6	7	8	9	10	11	12	13	14
Width, d (μm)	5	5	5	5	5	5	5	2	2	2	2	2	2	2
Separation, L (μm)	2	5	10	15	25	50	75	1	2	4	6	10	20	30
Covered surface, A _f (%)	92	75	56	44	31	17	12	89	75	56	44	31	17	12

The aim is for these grid patterns to be transferred to a silicon master. The master will be used to cast elastomer stamps. These stamps will subsequently be used to pattern catalyst solution onto substrates. Hence the catalyst will be deposited as grid formations. These patterns then act as templates for CNT growth. The position of nanotubes on the substrate surface is thus confined to within the dimensions of grid patterns. The use of gridlines with incremental spacings allows the amount of catalyst deposited on the substrates to be varied in a controlled manner. Ultimately then the area fraction of carbon nanotubes grown on the substrate surface can also be controlled. The dimensions of these gridlines correspond to a surface covering of between 12% and 92% of the substrate (table 4.1). Values for the area fraction (A_f) of substrate surface covered by the grids can be calculated by considering the geometry of the grid patterns (figure 1). The grid width (d) and the grid separation (L) are related according to equation 1.

$$A_f = \{(L + d)^2 - L^2\} / \{(L + d)^2\} \quad \text{Equation 1.}$$

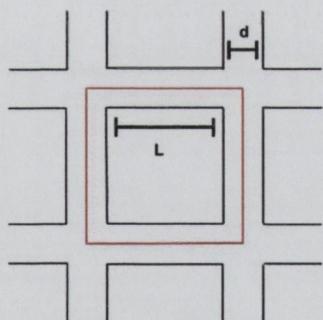


Figure 1: Grid patterns of width (d) and separation (L). The red outline represents the area enclosed by (L+d)².

The grid design was sent to Photonics (Wales) Ltd. where they manufactured a positive chrome on high grade quartz photomask. Soda-lime glass can be used instead of quartz

where feature sizes are greater than $2\mu\text{m}$. It is roughly 20% cheaper to get made. Quartz however contains less impurities and is more mechanically, thermally and chemically robust.

4.2.2 Transferring the Pattern onto a Silicon Wafer

This photomask was then used to transfer the grid pattern onto a silicon master. This was done under cleanroom conditions to minimise defects. A silicon wafer was first cleaned using a peroxide/sulphuric acid solution (H_2SO_4 : H_2O_2 in the ratio 3:1). This is an exothermic, corrosive mixture which removes any residual metals or organics from the silicon surface evolving H_2 bubbles in the process. Care must be taken to use only glassware and plastic with the mixture, stainless steel tweezers cannot be used. After bubbling has subsided, the silicon was rinsed and pre-baked to remove any residual water. Then a layer of hexamethyldisilazane (HMDS), adhesion promoter was spin cast onto the silicon. HMDS is toxic and fumes must not be inhaled. Next Shipley 1813 positive photoresist was dropped carefully onto the substrate, to avoid air bubbles, and spin coated at 5000rpm to yields a $1.2\mu\text{m}$ thick layer [9].

The photomask was then secured, chrome side down, in a Karl Suss MJB3 Aligner and positioned over the photoresist covered silicon wafer. The mask and the resist were carefully aligned. Unmasked areas were then exposed to UV (at $\lambda=250\text{nm}$) from a 274 Watt mercury lamp for 3.5 seconds. The exposed photoresist degrades and was subsequently removed using Shipley MF 319 developer. This leaves areas of the silicon substrate uncovered for etching.

4.2.2.1 Etching the Master

Etching is used to change the surface profile of a sample. Either wet or dry etching can be used. Wet etching involves reactants in the liquid phase and is a quick isotropic etch process. Hydrofluoric acid is an example of a liquid used for wet etching. Dry etching is slower and the etch rate is easier to control. The reactants are in the gas phase. We focus on reactive ion etching (RIE) which is a plasma based dry etch. The sample wafer is placed on the cathode plate in a RIE chamber. The machine is then pumped down to the required pressure, the process gas is introduced and a radio frequency (RF) electromagnetic field is applied across the electrodes in the chamber. We use carbon tetrafluoride (CF_4) as the

plasma process gas. This gas breaks down in the presence of an electric field forming a purple plasma. Positive plasma ions are attracted towards the anode and hence the wafer. There they etch the silicon both physically by ion bombardment, and chemically to release tetrafluorosilane (SiF_4) which desorbs from the surface.

The combined result is an anisotropic etch preferentially in the vertical direction. The amount of ions, and hence the chemical etch rate, can be controlled by the pressure. An increase in pressure results in an increase in the etch rate (figure 2). RF power can also be used to alter the etch rate as higher ion energies result in a more physical etch. However, physical etching can cause roughening of the substrate surface. We require a smooth surface for our master so it is preferential to use a lower RF power.

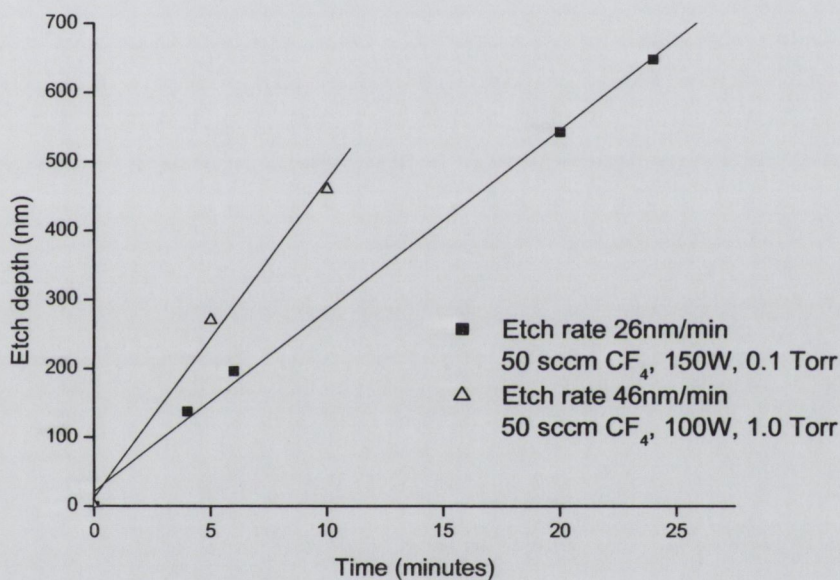


Figure 2: The etch rate can be controlled by varying RIE conditions. Etch depths were taken as the average measured from electron microscopy images.

We found optimum RIE conditions for our process to be CF_4 at a flow rate of 50 standard cubic centimeters per minute (sccm), RF power at 100W and a pressure of 1 Torr. This gave an etch rate of approximately 46nm/min. The etch time used was 15min. This should produce an etch depth of 690nm. After RIE the remaining photoresist was removed using sulphuric acid/peroxide (again in the ratio of 3:1). The etched silicon wafer was then imaged by a Hitachi S-4300 field emission scanning electron microscopy (FESEM). Images show pattern transfer to be successful. Grid patterns are well defined. It was observed however that when grid separations approach $2\mu\text{m}$, patterns begin to lose

definition and features become rounded. Interferometry was used to record the surface topography. Grids were measured to be 590nm deep (figure 3). This deviates slightly (~17%) from the predicted value of 690nm.

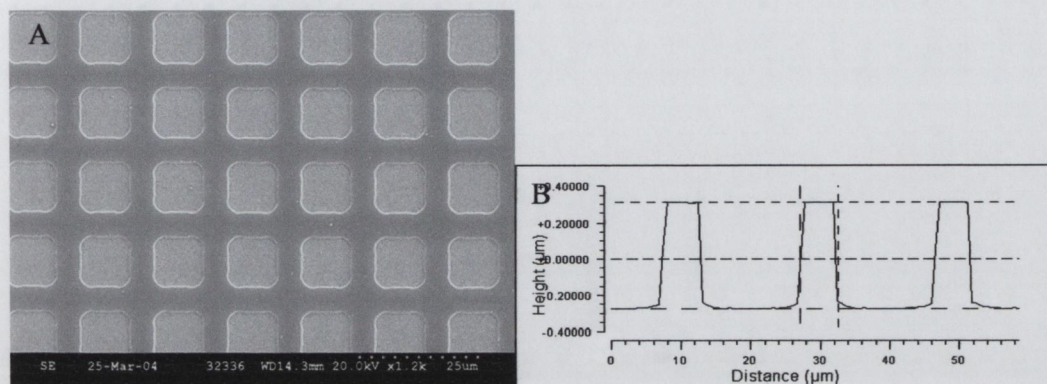


Figure 3: FESEM image of a grid pattern transferred onto a silicon master by photolithography. Lines are 5 μm wide and separated by 10 μm (A). Interferometry reveals the etch depth of the spacings between grids to be 590nm (B).

While optimising RIE conditions we tried removing the post-RIE photoresist using an oxygen plasma etch. This proved to be too harsh a process and resulted in a roughened silicon surface. The surface is much smoother when a peroxide/sulphuric acid solution is used (figure 4).

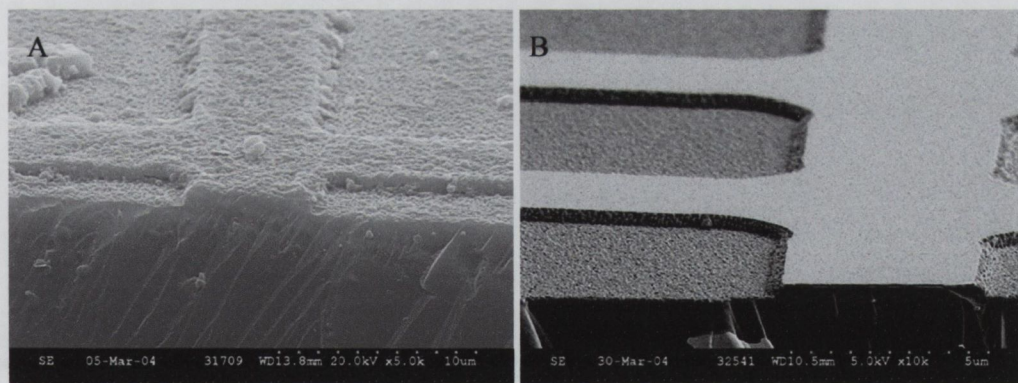


Figure 4: FESEM image of a roughened surface produced when an O₂ plasma is used to remove post-RIE photoresist (A). The surface is much smoother if a H₂SO₄: H₂O₂ mixture is used (B).

While optimising the etch rate, we also tried incorporating oxygen into the carbon tetrafluoride process gas. The presence of oxygen increases the etch rate as it reacts with carbon atoms in CF₄ thus releasing more fluoride ions. A mixture of CF₄ (50sccm) and O₂

(10sccm) was tried at an RF power of 100 Watt and a pressure of 1 Torr. These conditions were too vigorous and caused over-etching of the silicon (figure 5). Pattern definition was completely lost.

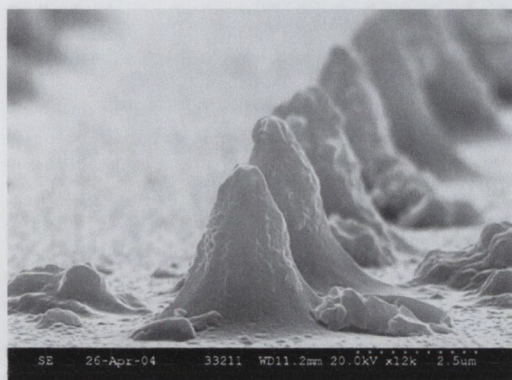


Figure 5: The presence of O₂ in the plasma etch causes over-exposure of the silicon.

As an alternative to RIE we tried argon ion milling. This is a physical etch process. The etch rate was extremely slow and after 30 minutes the etch depth was only 90nm. As a final option we switched to wet etching. This involved using hydrofluoric acid (48% HF, Sigma Aldrich) which is extremely corrosive and must be handled with the utmost care. The resist was baked at 110°C for 15 minutes prior to HF etching for it to harden. After 15 seconds in HF all the resist had disappeared. The acid was then diluted with water (HF: H₂O in a ratio 10:40 cm³). The substrate was dipped in this for 15 seconds followed by one minute in acetone. The etch depth was only 11nm. Henceforth all etching was done by RIE which is easier to control.

4.2.3 Release Promoter

Having successfully etched grid patterns into a silicon wafer, the aim was to cast elastomer stamps from this master. The elastomer used was Sylgard 184 (Dow Corning). This is a silicone elastomer and therefore has a -O-Si-O- backbone structure. All silicon wafers have a native surface oxide approximately 20Å thick [10]. The presence of water vapours and organics causes the functional groups -OH and -CH₃ to be present on a silicon surface. When an uncured Sylgard 184 mixture comes in contact with untreated silicon it forms a bonds with the surface as it cures. Irreversible sealing is caused by the formation of covalent -O-Si-O- bonds. This is the product of a condensation reaction between silanol groups and the -OH functional groups on the silicon surface (figure 6). The silicon master

must therefore be treated with a release promoter prior to casting Sylgard 184 elastomer stamps. The release layer must be extremely thin so that template feature sizes are not impaired.

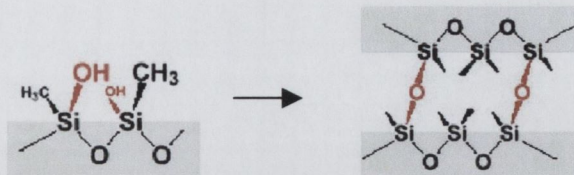


Figure 6: The presence of $-OH$ surface groups causes silicon to be hydrophilic. Sylgard 184 forms an irreversible seal with the surface due to the formation of covalent bonds during curing.

The master surface can be passivated by the gas phase deposition of a long-chain fluorinated alkylchlorosilane [11]. This is a bi-functional molecule. The silane-terminated end adheres to the template and the fluorinated chain orients away from the surface. Where fluorinated molecules are tightly packed, they provide a low energy surface release layer. The release layer must be durably bonded to the surface to remain functional after many imprints. For our experiments, we use 1H,1H,2H,2H-perfluorodecyltrichlorosilane, $CF_3(CF_2)_7(CH_2)_2SiCl_3$. This was purchased from Oakwood Products Inc. The silicon master is cleaned with deionised water and isopropanol. The surface is then activated by UV/ozone for 30mins. Ozone reacts with any organic impurities on the silicon surface. Immediately after activation, the substrate is placed in a dessicator together with about 0.3-0.5 ml 1H,1H,2H,2H-perfluorodecyltrichlorosilane. The dessicator is pumped down to a pressure of 2.0 mbar. The master is left exposed to fluorosilane vapours in the dessicator for one hour. The dessicator is vented. The silicon template is removed and immediately baked in a preheated oven at $60^\circ C$ for 45min. The change in surface energy of the master can be observed by contact angle measurements before and after treatment with the fluorosilane.

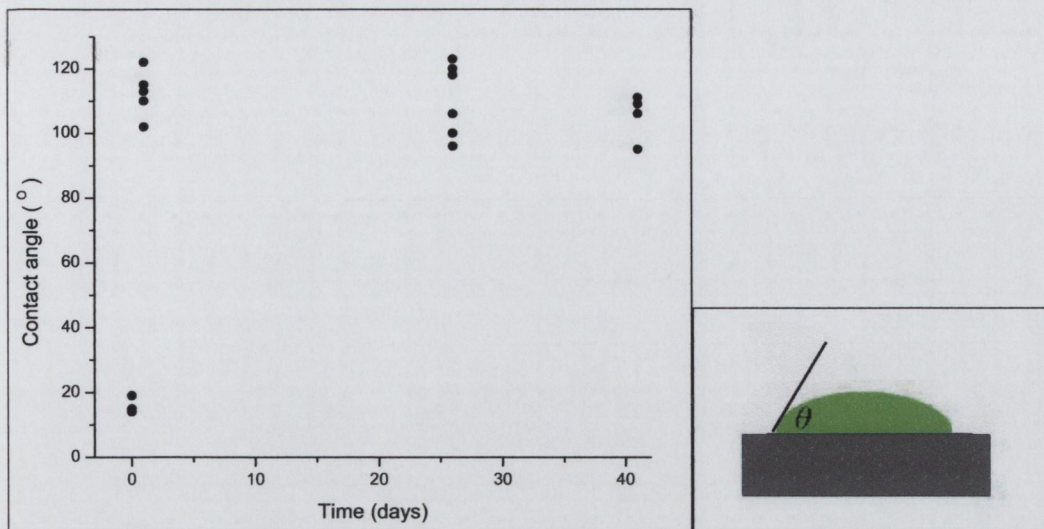


Figure 7: The contact angle (θ) of the silicon master increases after treatment with a release promoter. Measurements show no degradation of the release layer over 40 days. The image on the right shows θ to be the angle between the tangent to the droplet and the substrate surface.

The contact angle of the silicon master changes dramatically after exposure to fluorosilane. The surface transforms from hydrophilic to hydrophobic. Contact angles (measured using water droplets) change from 20° for the untreated surface to 110° for the treated surface. This hydrophobic surface is stable for periods in excess of 40 days, after which point we stopped measuring (figure 7). Stamps were cast from the master on day 5. This did not have any effect on the contact angle.

4.3 Casting Stamps

Sylgard 184 stamps were cast from the hydrophobic silicon master. The elastomer comes as a two-part kit with a base and curing agent. The two are mixed together in a 10:1 ratio. Mixing introduces air bubbles and the mixture must be left sit for at least one hour before use. The Sylgard 184 can then be poured onto the master template. The master must be confined on all sides to contain the medium viscosity elastomer mixture. Enough mixture is added to make stamps approximately 1cm thick. Sylgard 184 will cure in 24 hours at 23°C under room temperature and pressure. However, seven days is recommended for a complete cure [12]. We left stamps for ten days. After this time stamps have fully solidified and can be very easily released from the hydrophobic silicon master. The stamp topography was imaged using interferometry to ensure that pattern transfer was successful.

4.3.1 Interferometry of Stamps and Masters

White light interferometry is a non-contact technique used to obtain the height profile of a sample surface. The set-up is similar to a Michelson interferometer. Light is sent through a beamsplitter where the light is split along two arms, one leading to the sample and the other to a reference. The light reflected off the sample is then superimposed on the light beam scattered from the reference surface. Optical path differences between the waves results in a fringe pattern of constructive and destructive interference. This is detected by a CCD camera which then generates a three-dimensional image of the sample surface.

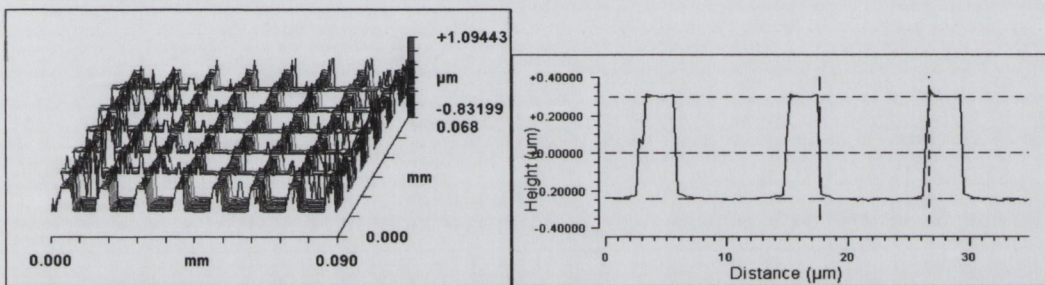


Figure 8: Interferometry images from a silicon master patterned with $2\mu\text{m}$ gridlines separated by $10\mu\text{m}$ hollows.

Surface profiles of the stamps were obtained using a Zygo New View 100 white light interferometer. Images show that pattern transfer was successful. The topography of a silicon master reveals protruding gridlines with indented separations (figure 8). Interferometry shows feature depths to be $540\mu\text{m}$. This is slightly less than the value of 590nm measured before the master was treated with fluorosilane. Stamps cast from these masters reveal an inverse topography. In this case gridlines are depressed and separations are elevated. Feature depths are slightly less than for the master at an average of $519\mu\text{m}$ (figure 9). Images show a good replication of the master profile.

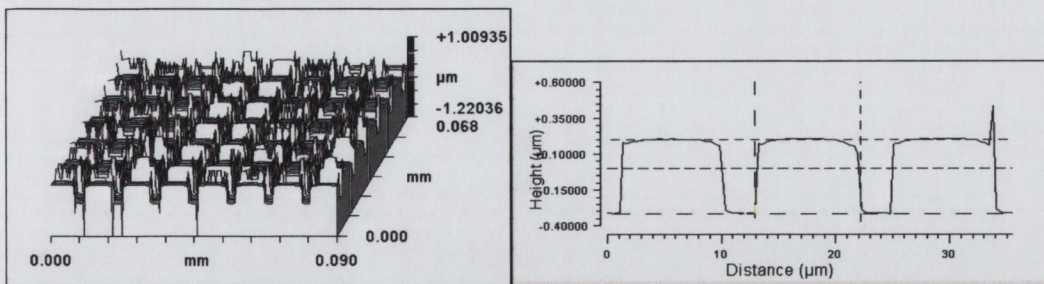


Figure 9: Interferometry images of a stamp, cast from the above silicon master, with $2\mu\text{m}$ hollows separated by $10\mu\text{m}$ wide plateaus.

Initially we tried to cast Sylgard 184 stamps from an untreated hydrophilic silicon master. The elastomer bonded to the silicon. After physically removing as much of the Sylgard as possible, the master was soaked overnight in a number of common solvents. Solvents used include acetone, tetrahydrofuran, methanol and dimethylsulphuroxide. None of these had any effect. The master was then soaked in white spirits for two weeks. This softened the elastomer but did not cleanly remove it. Interferometry of the silicon at this point showed an uneven surface with loss of pattern definition (figure 10). This is in complete contrast to the images obtained from a treated silicon master where the surface is smooth and the pattern is sharp. The only way we found to successfully remove Sylgard 184 from the untreated silicon was using dilute hydrochloric acid (10% in water). This was applied by rubbing the surface very gently with cotton buds. This removed the elastomer and appeared to leave the master undamaged.

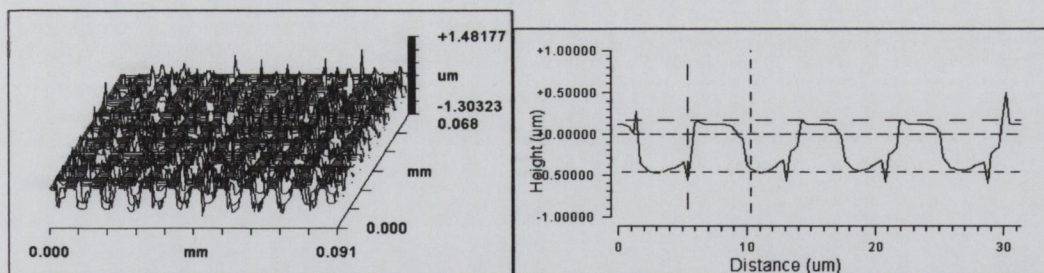


Figure 10: Interferometry of an untreated hydrophilic silicon master after casting Sylgard 184. The elastomer does not release from the master and remains bonded to the surface.

4.4 Patterning Substrates for Carbon Nanotube Growth

The Sylgard 184 stamps were then used to pattern poly(styrene-vinylferrocene) onto silicon oxide. When using an elastomer stamp to pattern liquid phase catalysts the solvent used must be chosen carefully. It has been reported that non-polar solvents such as toluene

and hexane cause elastomer stamps to swell and interfere with the conformal interface between the stamp and the substrate [13]. However, poly(styrene-vinylferrocene), PS-PVF, does not dissolve well in polar solvents and hence it was necessary to use toluene as the solvent. PS-PVF forms a solution in both toluene and tetrahydrofuran (THF). Toluene, C_7H_8 , has a boiling point of $110^\circ C$ compared to THF, C_4H_8O , which has a boiling point of $66^\circ C$. Toluene therefore evaporates more slowly than THF which results in the formation of more uniform catalyst patterns. We obtained good pattern transfer using toluene as the solvent. Also, contrary to expectation the quality of the stamps did not noticeably degrade after multiple (approximately 20 to 30) uses. The use of a non-polar solvent may conceivably shorten the lifetime of the stamps in the long-term. However, this was not investigated.

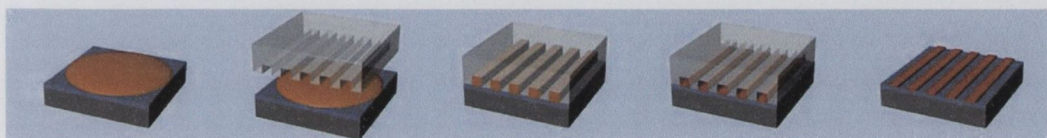


Figure 11: A diagram of the five-step process used to pattern a catalyst solution (orange) onto silicon oxide (purple). Here the patterning of parallel lines is illustrated.

The soft lithography patterning process used to deposit the poly(styrene-vinylferrocene) onto silicon oxide substrates is a simple five-step process (figure 11). First a small amount of catalyst solution is dropped onto a wafer (step 1). Then the pre-patterned Sylgard elastomer stamp is pressed into contact with the substrate (step 2). The stamp will make conformal contact with the substrate precluding the catalyst solution from the interface. The solution is forced to migrate into grooves on the stamp (step 3) thus replicating the pattern of the silicon master used to cast the stamp. This set-up is left overnight for the solvent to evaporate (step 4). The stamp is then removed and the catalyst micro-pattern can be observed on the substrate (step 5). The height of the micro-patterns can be controlled by varying the concentration of catalyst solution used.

4.4.1 Images of Catalyst Micro-Patterns

Soft lithography is a versatile patterning technique and can be used to generate a variety of pattern geometries. To illustrate this, we used elastomer stamps cast from a number of masters with different surface topographies. Using these stamps to pattern our catalyst, poly(styrene-vinylferrocene), we were able to generate dot, line and grid patterns (figure

12). The dots shown below are $5\mu\text{m}$ in diameter, lines are $2\mu\text{m}$ wide and gridlines are $5\mu\text{m}$ wide. Catalyst particles are confined to within the dimensions of these patterns. These micro-patterns can be used as substrates for carbon nanotube growth. Tubes will grow from catalyst particles. Thus we can expect that CNT growth will be selective to patterned areas of the substrates.



Figure 12: Silicon oxide substrates patterned by soft lithography. Catalyst particles are present within the patterns (darker regions) and absent elsewhere.

The area fraction of carbon nanotubes grown on the substrates can be controlled in either of two ways. The first is by altering the height of catalyst micro-patterns. This is achieved simply by varying the concentration of catalyst solution used to generate patterns. The nanotube density is a function of the number of catalyst particles present [14]. Therefore, an increase in the amount of catalyst deposited will result in an increase in the amount of CNTs grown. The second method is by varying the area fraction of the substrate surface covered in catalyst material. This can be controlled by changing the separation between pattern features. Taking grid patterns as an example, the inter-grid spacings can be incrementally increased. This effectively decreases the fraction of the substrate on which the catalyst is deposited. Using the master described in section 4.2, between 12% and 92% of the substrate surface can be covered. In the example below we show gridlines $5\mu\text{m}$ wide. Spacings between these gridlines can be increased from $10\mu\text{m}$ to $25\mu\text{m}$ to $50\mu\text{m}$. These values correspond (respectively) to area fractions of 56%, 31% and 17% of the substrate surface covered in catalyst (figure 13).

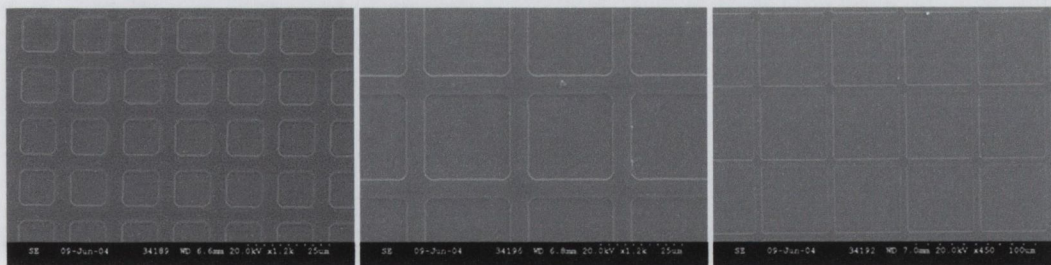


Figure 13: The polymer catalyst patterned into gridlines 5 μm wide. Spacings are incremental from 10 μm , to 25 μm and 50 μm (left-to-right).

FESEM images show that pattern transfer has been successful using soft lithography. However, they do not prove that poly(styrene-vinylferrocene) is confined to within the dimensions of the patterns. The location of PS-PVF on the substrate surface can be determined using energy dispersive x-ray spectroscopy.

4.4.2 Energy Dispersive X-Ray Spectroscopy

Many scanning electron microscopes (SEM) also have the capability for energy dispersive x-ray spectroscopy (EDXS). During SEM an electron beam is accelerated towards a sample and an image is generated from the scattered electrons. A high-energy electron beam may however excite the sample and cause photon emission. Photons are emitted when the occasional inner K-shell electron is knocked out thus leaving a vacant electron state. The energetic atom will relax back to the ground state by emitting a photon of energy. Emitted photons can be analysed to produce an x-ray spectrum. This spectrum displays x-ray intensity as a function of energy and can be used to determine elemental sample composition.

EDXS spectra for poly(styrene-vinylferrocene) patterned substrates were taken from 0 to 10 keV. The incident electron beam was accelerated at 15 keV, which is just over double the K_{α} energy for iron. An incident beam of higher energy would detect particles buried beneath the substrate surface. A lower energy beam would not be sufficient to remove an inner electron from its K-shell. Each peak in an EDXS spectrum can be assigned to a specific element. The elements we expect to see are iron, silicon, oxygen and carbon. They have K_{α} values at 6.4, 1.74, 0.523 and 0.282keV respectively. Iron also has an L_{α} value of 0.704 keV. Sum peaks and escape peaks are also present. For example a peak at 3.48 keV (2×1.74) is caused by two x-rays from silicon hitting the detector simultaneously.

Similarly, an escape peak is caused when two x-rays hit the detector simultaneously and interfere destructively causing a peak at 0 keV.

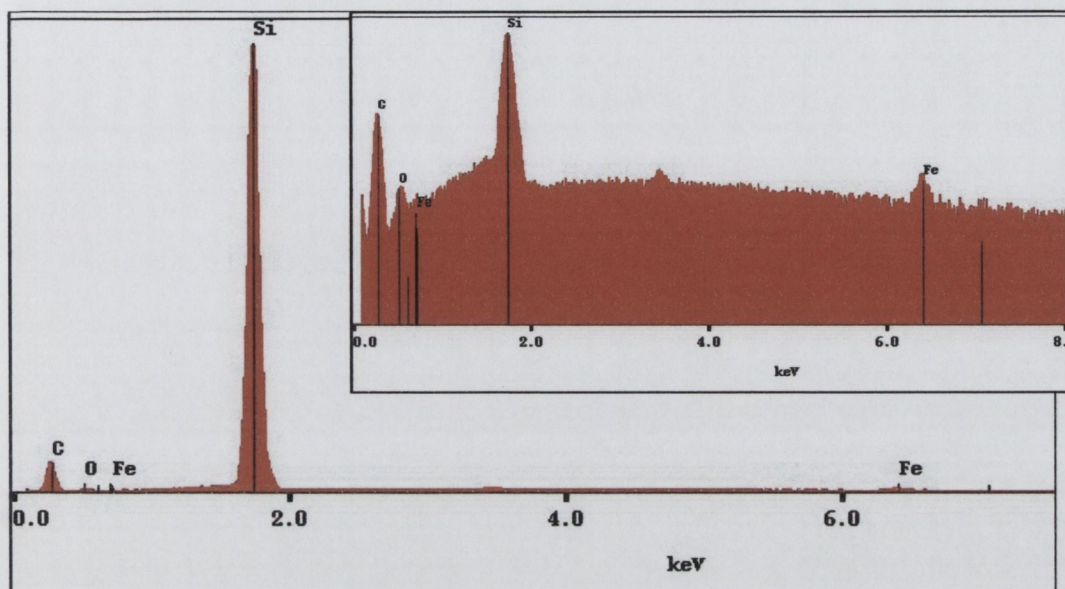


Figure 14: EDXS line plot taken from an area within the boundaries of a gridline. Due to the small amount of iron present, the plot is easier to read as a log plot (inset).

EDXS spectra were taken from areas within the dimensions of the micro-patterns. Here we expect to see an iron peak reflecting the iron nanoparticles contained within the poly(styrene-vinylferrocene) catalyst. Iron however accounts for only 2.1% of the polymer. The iron peak seen in EDXS should therefore be of low intensity. We also expect to detect silicon and oxygen peaks due to the proximity of SiO_2 to the polymer. Because the iron peak obtained was of low intensity, it is easier to see in a log plot (figure 14).

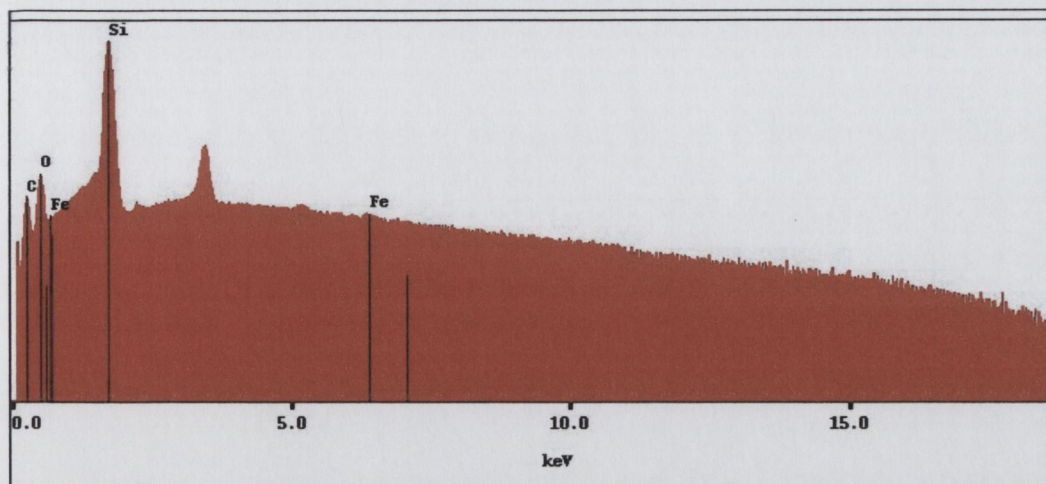


Figure 15: EDXS log plot taken from an area between gridlines. The spectrum verifies the presence of carbon, oxygen, silicon and the absence of iron.

A similar spectrum was obtained from the substrate area between pattern features. EDXS shows the presence of carbon, silicon and oxygen (along with a silicon sum peak, at 2×1.74 keV). The iron peak is notably absent. The silicon and oxygen are due to the SiO_2 surface. The amount of carbon is significantly reduced. The small carbon peak is probably due to trace amounts of organic materials (possibly toluene residue). Results from EDXS verify that catalyst particles are confined to within the dimensions of pattern features and are absent elsewhere on the substrate surface.

4.4.2.1 EDXS to Confirm the Presence of Iron at High Temperatures

Substrates are to be used as templates for carbon nanotube growth. CNT growth generally occurs at elevated temperatures above 600°C [15]. In section 3.3.3 thermal gravimetric analysis results showed that the majority of poly(styrene-vinylferrocene) degrades below 470°C . At temperatures above 700°C , less than 5% of the polymer remains. This is assumed to be the iron component of the polymer. To confirm the presence of iron at high temperatures, a poly(styrene-vinylferrocene) pattern was stamped onto silicon oxide. The sample was heated to 950°C under argon at atmospheric pressure. After cooling, EDXS was performed on the sample. Spectra (not shown) exhibit iron peaks. This confirms that iron particles remain and the polymer catalyst is suitable for CNT growth.

4.5 Conclusion

In this chapter we have demonstrated that poly(styrene-vinylferrocene) can be patterned onto silicon oxide substrates using soft lithography. A variety of pattern geometries are possible and line, dot and grid patterns were shown as examples. Using soft lithography the amount of catalyst deposited onto substrates can be easily controlled. We showed that catalyst particles are confined to within the dimensions of patterns and absent elsewhere on substrates. We also verified that iron from our catalyst copolymer remains at elevated temperatures. This is an important issue for CNT growth.

4.6 References

- [1] S Huang, L Dai, AWH Mau, *Adv. Mater.*, 14 (16), 1140, 2002
- [2] J Kong, HT Soh, AM Cassell, CF Quate, H Dai, *Nature*, 395, 878, 1998
- [3] H Kind, JM Bonard, L Forro, K Kern, K Hernadi, LO Nilsson, L Schlapbach, *Langmuir*, 16, 6877, 2000.
- [4] S Huang, L Dai, A Mau, *Physica B*, 323, 333, 2002
- [5] KBK Teo, M Chhowalla, GAJ Amaratunga, WI Milne, DG Hasko, G Pirio, P Legagneux, F Wyczisk, D Pribat, *Appl. Phys. Lett.*, 79(10), 1534, 2001
- [6] Y Xia, GM Whitesides, *Angew. Chem. Int. Ed.*, 37, 550, 1998.
- [7] B Michel, A Bernard, A Bietsch, E Delamarche, M Geissler et al, *IBM J. Res. Dev.*, 45(5), 697, 2001.
- [8] IC Design Software, Whiteley Research Inc., 456 Flora Vista Avenue, Sunnyvale CA 94086.
- [9] Shipley Microposit S1800 Series Photo Resists Data Sheet.
- [10] S Mizushima, *Metrologia*, 42, 208, 2005
- [11] YL Loo, T Someya, KW Baldwin, Z Bao, P Ho et al, *PNAS*, 99(16), 10252, 2002
- [12] Data sheet, 'Information about high technology silicon materials', Dow Corning.
- [13] JP Rolland, RM Van Dam, DA Schorzman, SR Quake, JM DeSimone, *J. Am. Chem. Soc.*, 126, 2322, 2004
- [14] Y Tu, ZP Huang, DZ Wang, JG Wen, ZF Ren, *Appl. Phys. Lett.*, 80(21), 4018, 2002.
- [15] ZF Ren, ZP Huang, JW Xu, JH Wang, P Bush, MP Siegel, PN Provencio, *Science*, 282, 1105, 1998.

Chapter 5: The Production of Nanotube Arrays

5.1 Introduction

In this chapter we introduce carbon nanotube production. We show how ordered nanotubes arrays can be grown from silicon oxide substrates. By patterning the substrates with a catalyst, the location of CNT growth can be controlled. We demonstrate how tubes of uniform diameter can be produced free from amorphous carbon. We also explore some difficulties associated with CNT growth.

5.2 Chemical vapour deposition system

Carbon nanotubes were produced by thermally activated chemical vapour deposition (CVD). The CVD system used was purpose built to allow variables such as pressure, temperature and gas flow rates to be monitored during carbon nanotube growth. A photograph of the set-up is shown in figure 1.

Substrates are patterned with a catalyst material (as described in section 4.4) and placed in an alumina crucible. The crucible is then placed midway along a horizontal quartz tube held in a furnace (#1, figure 1). Argon gas is flowed through the quartz tube to purge the system of atmospheric gases and water vapours. The argon flow rate is set using a digital monitor (#2, figure 1) connected to a mass flow controller (#3, figure 1). The furnace temperature is then set for 700°C and the substrate is heated under flowing argon. At 700°C, acetylene gas is added to the system. The acetylene flow rate is fixed using a second mass flow controller. After sufficient time has elapsed for CNT growth to occur, the system is cooled back to room temperature. Argon gas continues to flow during the cooling process to avoid potential oxidation of the nanotubes at high temperatures. CVD is often carried out under low pressures. Therefore, the CVD system is connected to a mechanical pump (#4, figure 1). The pressure of the system can be monitored by a vacuum gauge (#5, figure 1) connected to a thermovac sensor (#6, figure 1). A liquid nitrogen trap (#7, figure 1) is connected in series with the mechanical pump to remove by-products from the system and prevent decomposed hydrocarbon gases entering the pump and contaminating the oil.

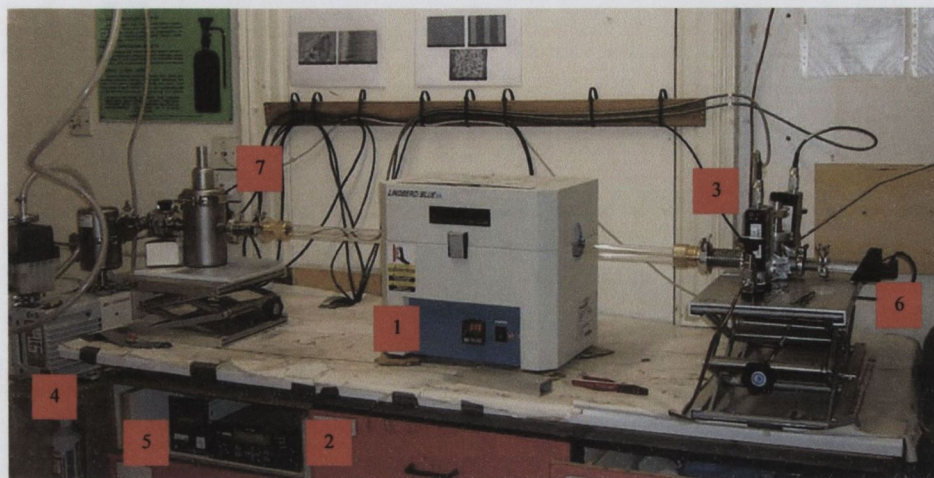


Figure 1: A photograph of the CVD system used for CNT growth (the apparatus was designed and assembled by Rory Leahy). The most important components are labelled from 1-7.

Atmospheric gases must be prevented from entering the CVD system as they can affect CNT growth. Stainless steel quick flange components are used to create an airtight chamber. Attaching flanges to the quartz tube was at first problematic. Initially an epoxy (Epoxy-EEZ general purpose twin pack) was used to secure flanges to either end of the tube. However, the epoxy seal was found to crack repeatedly and was not secure. To avoid leaks, a brass fitting was custom made to fit the diameter of the tube and connect it to the flanges (figure 2). These brass fittings have the advantage of being re-usable as they can be attached onto a number of consecutive tubes. Unlike epoxy, which takes time to cure, they can be used immediately. The brass fittings form a vacuum seal as threaded brass components are screwed together to secure an o-ring in the centre. The system can be confidently pumped down to 10^{-2} mbar without leaks.

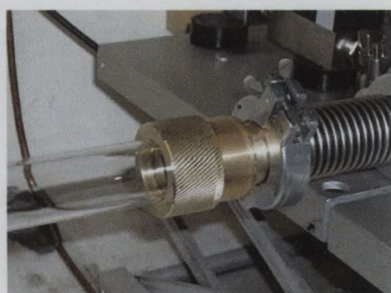


Figure 2: A brass fitting is used to connect the quartz tube to a stainless steel flange attached to the CVD system.

Typical operating conditions are an argon flow rate of 200 standard cubic centimetres per minute (sccm). After 5 minutes of argon flow, the furnace is heated to 700°C and liquid nitrogen is added to the trap. The system takes 16 minutes to reach 700°C (this implies a heating rate of approximately 42°C/min). The acetylene flow rate is typically 50sccm. Deposition times range from 10 to 30 minutes. Argon continues to flow during this time to avoid amorphous carbon deposition, which can occur when the acetylene partial pressure is too high [1]. CVD is carried out under atmospheric pressure (10^3 mbar). No advantage was observed to operating at lower pressures.

5.3 Process optimisation

The yield and morphology of CNTs produced by CVD depends on a number of factors. These include growth temperature, catalyst type and catalyst concentration. By altering these variables we were able to control the density, position and diameter of tubes grown. Control of these parameters is of huge importance for commercial applications such as flexible electronics. Other important variables in the CVD process include hydrocarbon source, growth time, carbon partial pressure and gas flow rates.

Many hydrocarbons have been successfully used to grow CNTs. These include methane, methanol, toluene and ethylene [2]. It has been reported that the most reactive carbon sources are unsaturated hydrocarbon as they bond more easily to reactive catalyst sites [2]. Saturated hydrocarbons (like methane) must first dehydrogenate which requires a higher reaction temperature. Aromatic hydrocarbons (like toluene) tend to decompose to C_6 molecules which do not bond as easily to catalyst particles. Alkynes are the most reactive unsaturated compounds due to the high chemical energy and reactivity of their triple bond. For this reason, we choose ethyne (C_2H_2) as the hydrocarbon source for our CNT growth. Ethyne is more commonly known as acetylene. Acetylene is a colourless, flammable gas which begins to pyrolyse above 400°C. Decomposition is exothermic and may give rise to explosions. Therefore, acetylene must be handled with extreme care and a flashback arrester must be connected to the pipe leading from the gas cylinder. Another requirement when working with acetylene is that stainless steel piping be used, as acetylene is incompatible with copper.

The catalyst containing compound used for CNT growth is poly(styrene-vinylferrocene). The iron core of this molecule is active during nanotube growth. The catalyst contains

2.1% iron, the remainder being carbon and hydrogen. The carbon and hydrogen molecules will decompose at relatively low temperatures and only 5% of the copolymer (presumably iron or iron oxide) remains at 700°C.

The catalyst is dissolved in toluene and patterned onto silicon oxide substrates by soft lithography. Patterned substrates were imaged by field emission scanning electron microscopy (FESEM). After CVD, it was observed that nanotube growth was selective to patterned areas of the silicon oxide substrate (figure 3). This is due to the presence of iron catalyst particles within the confines of the micro-patterns and the absence of any catalyst particles elsewhere on the substrate. This proves that poly(styrene-vinylferrocene) to be an active catalyst for the growth of CNTs. The diameter of the tubes varies between 30 and 45nm, which includes a 2x10nm gold layer deposited for imaging purposes. A variety of patterns geometries are possible and the dimensions of patterns shown below are from 5-10µm.

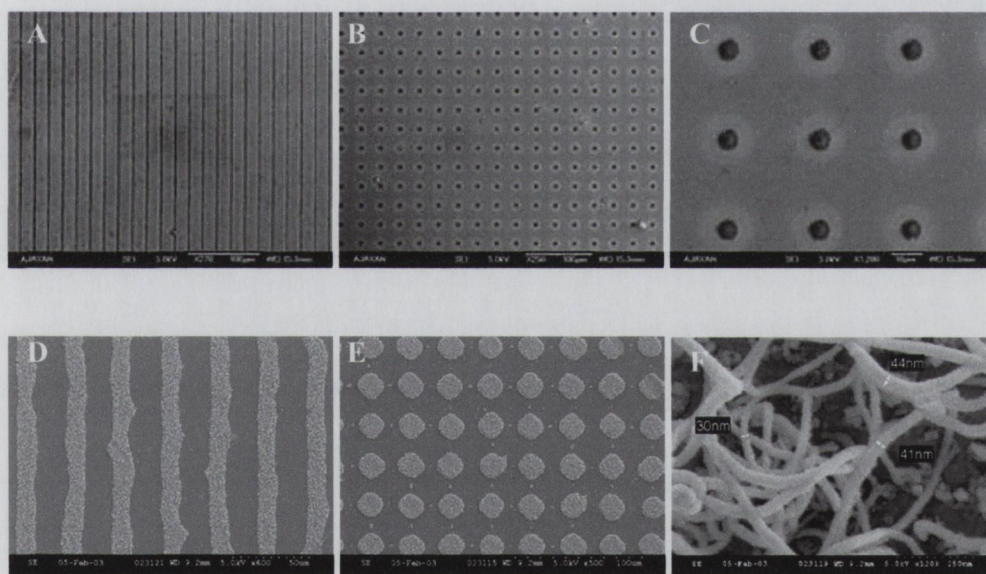


Figure 3: Micro-patterned substrates for NT growth. Darker areas correspond to regions of high catalyst concentration and paler areas represent the silicon oxide substrate (A-C). After CVD, carbon nanotube growth occurred only on the micro-patterned areas of the substrate (D-F).

Silicon oxide has been shown to be a good support material for iron catalysts used in the production of CNTs. The oxide must be a minimum of 5-6nm thick for CNTs to grow. The catalyst will diffuse through thinner oxide layers to react with the underlying silicon. This results in the formation of iron silicides (FeSi_2) and iron silicates (Fe_2SiO_4) which do not

catalyse CNT growth [3]. Iron in the form of γ -Fe (fcc) forms on silicon oxide and is active as a catalyst for CNT growth. For silicon oxide films greater than 6nm thick, some iron can diffuse through the oxide barrier and the CNT growth rate is diffusion limited. The CNT growth rate saturates for oxides \sim 50nm thick where diffusion no longer occurs [4].

Carbon atoms formed from the catalytic decomposition of acetylene, attach onto reactive sites on iron particles. At temperatures above 500°C, carbon atoms diffuse into iron with a mobility (diffusion coefficient) which increases with temperature. The iron nanoparticle becomes supersaturated and carbon precipitates out at less reactive sites. The ensuing density gradient is responsible for continued carbon diffusion [5]. Precipitated carbon forms a graphitic plane perpendicular to the surface of the iron particle. These graphitic planes quickly evolve to become nanotubes. CNT growth will cease when carbon atoms can no longer access catalyst particles.

Access to catalyst particles can be blocked by an oversupply of carbon. This occurs where hydrocarbon decomposition occurs at too high a rate. The amount of catalyst present is insufficient to absorb all the carbon and amorphous carbon deposition occurs. Decreasing the hydrocarbon pressure will reduce the amount of decomposed carbon available. Alternatively, an oversupply of carbon can result in the formation of iron carbide (FeC_3). The diffusion coefficient of carbon is low in FeC_3 and this also acts to inhibit CNT growth [6]. Therefore, the acetylene partial pressure is important for clean CNT growth.

The density of carbon nanotubes grown is dependent on the height of catalyst micro-patterns. This is easily controlled by altering the concentration of catalyst solution used during soft lithography patterning. For lower concentrations (1wt%) the nanotube growth is quite sparse and for higher concentrations (2wt%) the density of tube growth increases (figure 4). Control over density of tube growth is critical for applications such as field emission where, screening by neighbouring emitter tips occurs if the density is too high [7]. If the density is too low, amplification of the applied electric field is not sufficient. Control over nanotubes density is also desirable for composite applications where a specific concentration of CNTs is required for percolation [8].

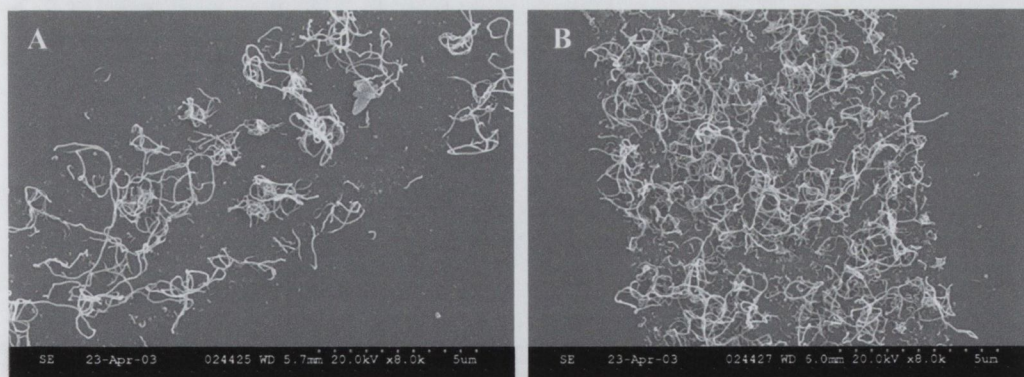


Figure 4: The density of tube growth increases with catalyst concentration. Image A shows CNTs grown using 1wt% PS-PVF in toluene. Image B shows CNTs grown using 2wt% solution.

The uniformity of the nanotube growth is sensitive to the choice of catalyst used. For comparison poly(vinylferrocene) was used as a catalyst. Poly(vinylferrocene), PVF, is a homopolymer similar in structure to PS-PVF, except without the polystyrene block. The PVF catalyst resulted in clusters of nanotubes forming within pattern boundaries (figure 5). No growth occurred outside the patterned areas. However, growth within the dimensions of the pattern was less homogeneous than that obtained using the PS-PVF copolymer catalyst. This suggests that the styrene part of the copolymer acts as an agent to disperse the catalyst (Fe) particles on the surface of the substrate. The PVF homopolymer is therefore not as efficient a catalyst as the PS-PVF copolymer for nanotube growth.

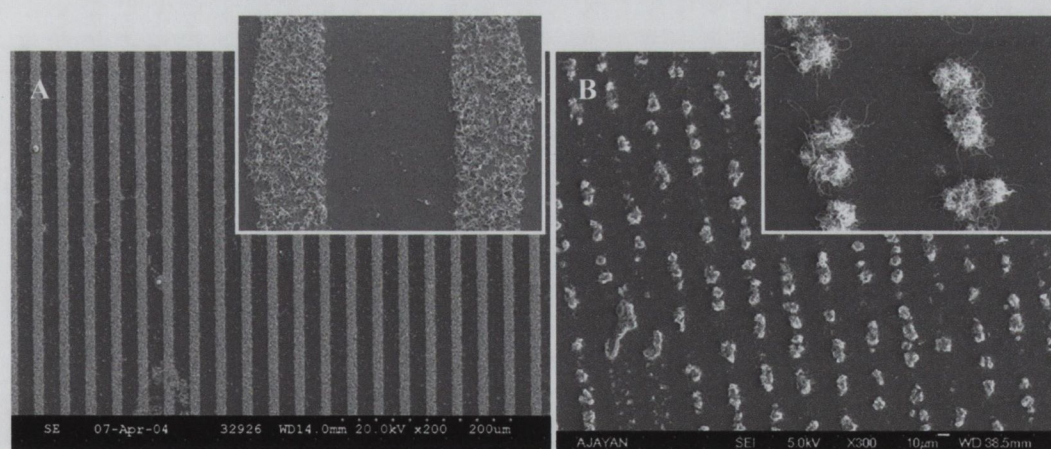


Figure 5: Nanotube growth was more homogeneous when a poly(styrene-vinylferrocene) copolymer (A) was used instead of a poly(vinylferrocene) homopolymer (B). Insets show magnified images of the CNT arrays.

The diameter of the carbon structures grown was observed to increase with temperature (figure 6). This has also been observed by other researchers [9]. The diameter increase is possibly due to the extra energy of catalyst particles at elevated temperatures. Iron particles migrate and agglomerate together to form clusters. Clusters have a lower surface energy than nanoparticles. This is a result of a decrease in the surface area to volume ratio. The tubes grown from these clusters have larger diameters than those grown from well-dispersed iron nanoparticles at lower temperatures. Nanotube diameter has been previously reported to increase with catalyst particle size [10]. It has been reported that above 900°C, acetylene will decompose to soot [2]. It is therefore better to use lower temperatures for CVD growth with acetylene. Other hydrocarbons such as methane require higher processing temperatures.

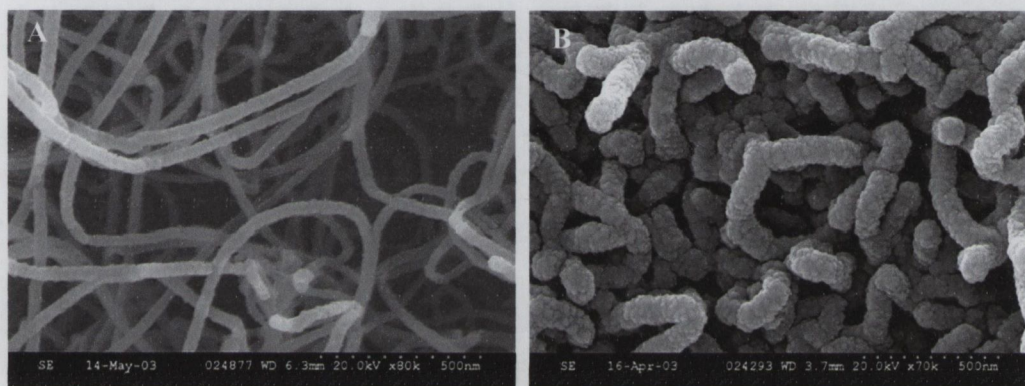


Figure 6: Nanotube diameter increases with temperature. At 700°C, average diameters are 20nm (A). At 800°C average diameters are 70nm (B). These values exclude the thickness of the gold coating. The diameter distribution is uniform at both temperatures.

Deposition time also affects the morphology of CNT arrays formed. Beyond a critical point, decomposed carbon vapours can no longer access catalyst particles and amorphous carbon deposition occurs. This amorphous carbon forms as a layer over the CNT array already formed (figure 7).

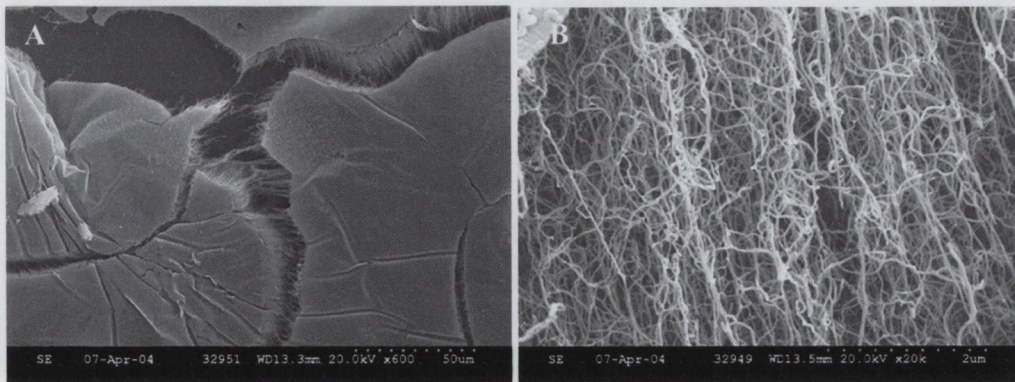


Figure 7: After 30 minutes deposition time, an amorphous layer was observed to form over the surface of CNTs (A). A close-up side-profile shows CNTs formed under the amorphous layer (B).

It is necessary to maintain the acetylene partial pressure below a certain threshold value during CVD. This is achieved by using a sufficiently low acetylene flow rate. The acetylene flow is also diluted by flowing argon simultaneously. It was observed that when argon does not flow during the deposition time and acetylene pressure is allowed to increase, only amorphous carbon is deposited (figure 8). The acetylene content in this situation is too high for it to catalytically decompose and re-form as CNTs. Instead, pyrolysis to amorphous carbon at high temperatures occurs. EDXS (not shown) confirmed that structures are composed of carbon.

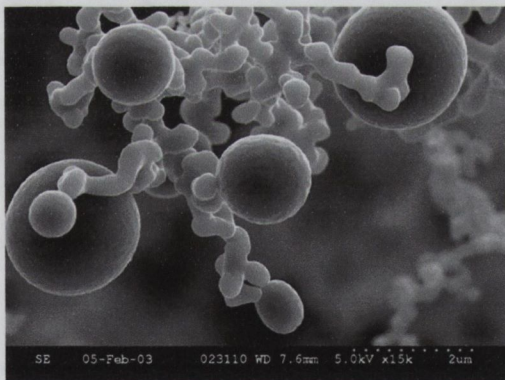


Figure 8: Amorphous carbon deposits form where the acetylene partial pressure is too high.

5.4 CNT growth on grid patterns

Carbon nanotubes arrays can be grown in a variety of geometries. Line and dot patterns have already been demonstrated in section 5.3. It is intended that as-grown nanotubes be directly incorporated into a flexible free-standing thin film composite. This can be

achieved by spin coating a curable polymer onto the tubes. To enable reinforcement in both the x- and the y-plane of a thin film composite, we position nanotubes into grid patterns. Grid lines are chosen to be 5 μ m wide. The amount of CNTs grown on the substrates can be manipulated by simply varying the grid separations. When embedded in a polymer film, these grid patterns will provide a means of pre-determining the volume fraction of nanotubes embedded within the polymer. Soft lithography patterning can thus be used to selectively position CNT conduction channels and control their volume fraction within a composite.

To produce CNT grid patterns, 4% poly(styrene-vinylferrocene) catalyst solution was patterned onto silicon oxide substrates by soft lithography. The SiO₂ was 100nm thick, which is sufficiently above the critical thickness of 50nm where CNT growth velocity saturates [4]. CNTs were grown by thermal CVD under an argon environment at atmospheric pressure. The argon flow rate was 200 sccm. The furnace was heated to 700°C. Then the carbon source, acetylene, was released into the CVD chamber for a deposition time of 20 minutes. After CVD, the substrates were imaged using FESEM (figure 9).

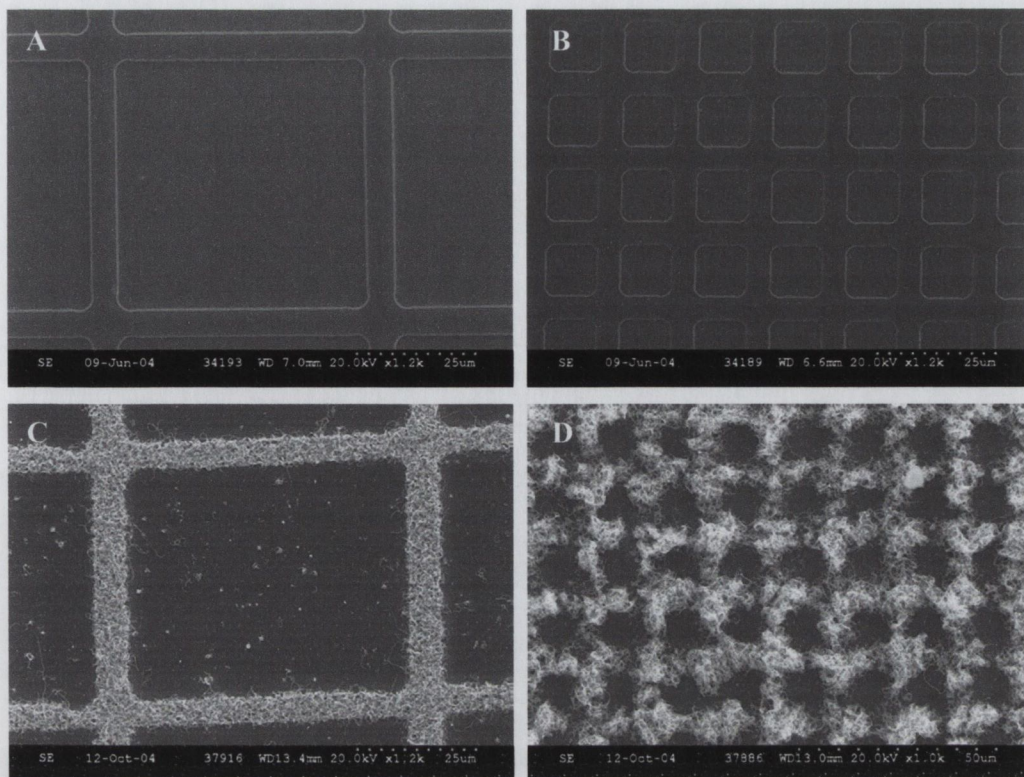


Figure 9: Catalyst micro-patterns generated by soft lithography patterning (A and B). The width of the gridlines is $5\mu\text{m}$ and spacings are $50\mu\text{m}$ and $10\mu\text{m}$. After CVD, CNTs were observed to grow selectively on the grid lines (C and D).

The area fraction of the substrate surface covered by CNTs can be calculated from the dimensions of the grid patterns. A $5\mu\text{m}$ wide grid line with a $50\mu\text{m}$ separation corresponds to 17% of the surface area being covered. A $5\mu\text{m}$ wide grid line with a $10\mu\text{m}$ separation corresponds to 56% of the surface being covered. Therefore by increasing the grid separations we have decreased the amount of nanotubes covering the surface by approximately one third (see section 4.1.1 for calculations).

Magnification of the carbon nanotube arrays reveal that CNTs do not grow aligned (figure 10). The random orientation and entanglements of tubes is desirable for polymer reinforcement. When aligned CNTs are embedded in a polymer matrix, reinforcement is limited only to the direction of alignment. However, when nanotubes are randomly oriented, reinforcement can be achieved in three-dimensions.

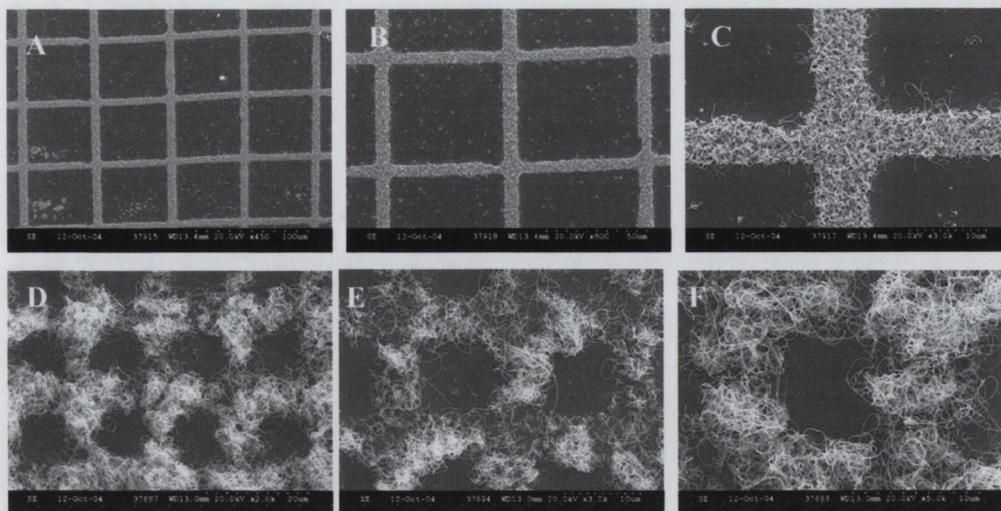


Figure 10: CNTs grown on grid patterns with 50µm (A-C) and 10µm (D-F) spacings. Magnification of the arrays shows the random entanglement of tubes within the dimensions of the patterns.

Closer inspection reveals a narrow diameter distribution for CNTs produced at 700°C. Their diameter, measured from FESEM images, varies between 25 and 49nm (figure 11). This includes a gold coating of approximately 2x10nm deposited for imaging purposes. The majority of values lie in the region of 40 to 44nm, which corresponds to tube diameters of approximately 20nm. This is consistent with multi-walled nanotubes.

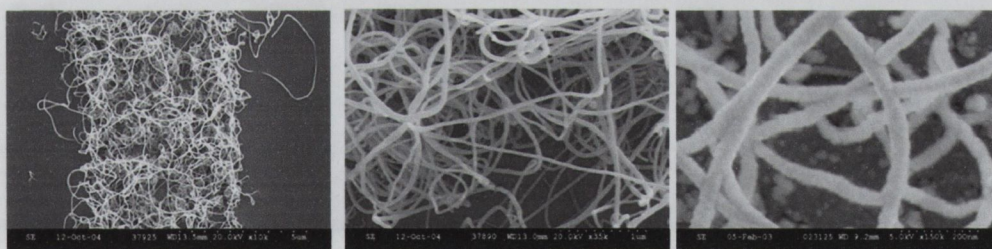


Figure 11: Average diameters for the MWNTs produced are 20 nm (not including the gold coating).

It was also possible to produce aligned CNT forests using the conditions described above (figure 12). This is achieved by increasing the concentration of catalyst particles on the substrate surface. Instead of soft lithography patterning, the catalyst solution was drop cast onto silicon oxide. A relatively large volume of solution can be deposited by drop casting, as the liquid is not confined by the dimensions of a stamp. The solvent is allowed to evaporate and the substrate is exposed to CVD conditions identical to those described above.

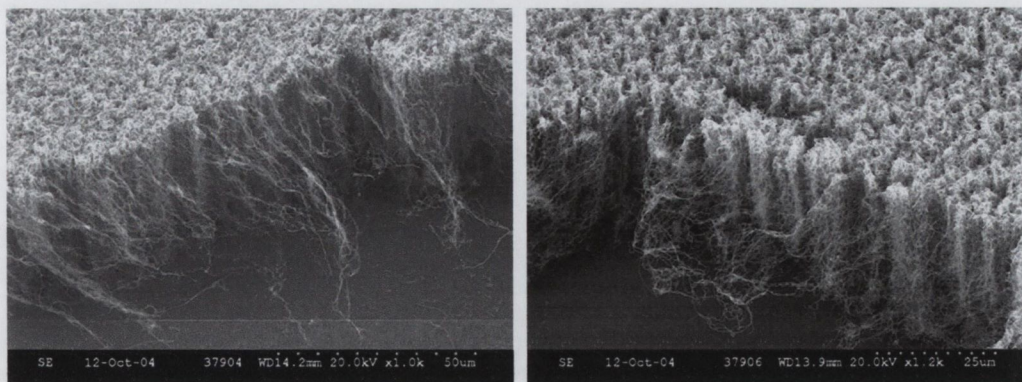


Figure 12: Aligned CNTs can be produced by drop casting the catalyst solution onto a silicon oxide template. These images were produced by flowing acetylene (200 sccm) for 20min.

5.5 Nanotube growth using other CVD systems

The CVD system built in Trinity College, has two gas inlets. One is connected to acetylene and the other to argon. We determined the preferred CVD conditions for a poly(styrene-vinylferrocene) catalyst to be an argon flow rate of 200sccm, an acetylene flow rate of 50sccm, atmospheric pressure and a temperature of 700°C. Other research groups have reported nanotube growth using similar CVD processes. Minor variations of the basic CVD process can often enhance CNT production. For example, ammonia has been used to eliminate the deposition of amorphous carbon [11]. Some research groups also use hydrogen for the reduction of oxidised catalyst particles prior to CVD [12]. Our set-up does not have the capability for either of these processes. Collaborations with other research groups however allowed us investigate some alternative CVD processes. All substrates used were prepared in the usual manner by patterning the poly(styrene-vinylferrocene) catalyst onto silicon oxide substrates.

Prof. Bill Milne's research group, based in the University of Cambridge, have developed a technique of rapid CNT growth. A short burst of acetylene gas is introduced to their CVD system at high temperatures. The short deposition time prevents the formation of amorphous carbon. The system is typically used to produce SWNTs grown on a triple-layer catalyst film of aluminium, iron and molybdenum deposited onto silicon oxide [13]. These samples are heated to 1000° C in helium. The chamber is then evacuated and acetylene is introduced at a flow rate of 50-250 sccm for deposition times typically ranging

from 10-100 seconds. Then chamber is refilled with helium and cooled to room temperature. Longer deposition times result in the formation of a layer of amorphous carbon. For example 10 minutes deposition time caused a 30nm thick amorphous layer to form. The SWNTs produced are highly crystalline due to the elevated temperature used.

Due to a collaboration, it was possible to send samples over to be tested in this CVD system [14]. Prior to shipping, it was necessary to anneal our samples. This is done to remove the hydrogen and carbon components from the catalyst and prevent possible contamination of the CVD set-up at Cambridge. Annealing was done under an argon atmosphere at 470°C for 10 minutes. Samples were then cooled back to room temperature under flowing argon to impede oxidation of the iron particles. At Cambridge, these samples were heated under low vacuum (without argon). Hydrogen was introduced at the CVD temperature to reduce the iron catalyst particles. This was followed by a short burst of acetylene. The optimum temperature for the poly(styrene-vinylferrocene) catalyst material was 750°C. A deposition time of 90 seconds produced the best results (figure 13). Tubes grown under these conditions were exclusively MWNTs.

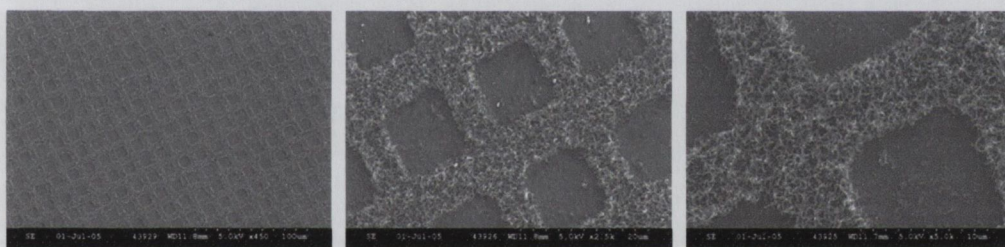


Figure 13: CNTs grown from a 90 seconds burst of acetylene gas at at 750°C. MWNTs grow selectively on catalyst patterned areas of the substrate. FESEM images increase in magnification from left to right.

Poly(styrene-vinylferrocene) patterned substrates were also sent to a collaborator at Infineon Technologies [15]. There they were placed in a CVD reactor which can hold up to twenty five six-inch wafers. Infineon's process involves pre-treating the substrates with hydrogen, followed by the introduction of acetylene. A deposition time of only 2 minutes is required to produce CNTs 50 μ m long [16]. Temperatures range from 400-800°C. Standard operating conditions are H₂/C₂H₂ under atmospheric pressure at 700°C [16]. Nanotubes were successfully grown onto grid patterns using this system (figure 14).

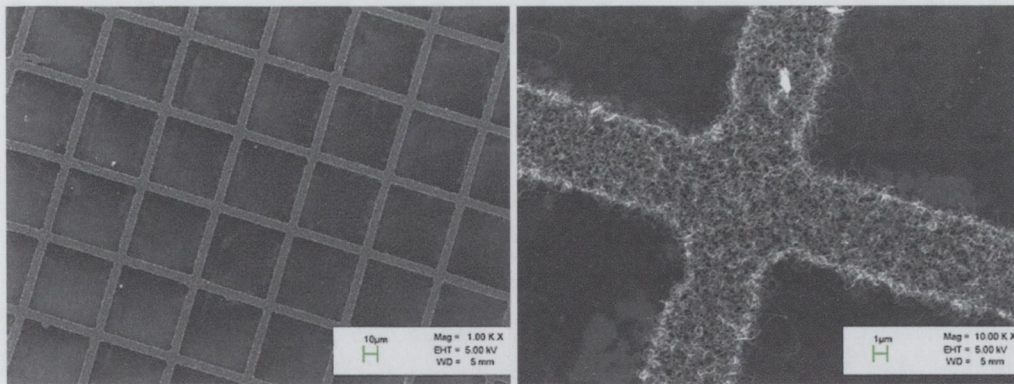


Figure 14: CNTs grown from on a PS-PVF patterned substrate at Infineon Technologies. CVD is done at 700°C using H_2/C_2H_2 .

CVD using ammonia was also explored. This was done at the Max Planck Institute, Stuttgart [17]. The furnace for this system is on wheels and can thus be moved along the length of the CVD tube. This provides a means of rapidly heating the substrates. The tube was connected to both ammonia and acetylene gas sources. The furnace temperature is maintained at 700°C and samples are inserted at the cool end of the CVD tube. The system is sealed and evacuated to $\sim 3 \times 10^{-2}$ mbar. After 5 minutes, the pre-heated furnace can then be moved to cover the substrate. This results in an almost instantaneously jump in substrate temperature to 700°C. The system is allowed to equilibrate for a further 10 minutes and then ammonia is released into the CVD chamber. There are no mass flow controllers on this system. To slow the ammonia flow rate, the butterfly valve connecting the CVD system to the mechanical pump is closed half way. The pressure (due to ammonia) then reads 1 mbar. The ammonia is then switched off and acetylene is subsequently released into the CVD system (also at 1 mbar). There is no argon used in this process. Instead, atmospheric gases are removed by pumping. During deposition, the pump cannot be switched off as pumping (or argon flow) is required to prevent amorphous carbon deposition. We tried varying the ammonia pre-treatment time from 2-10 minutes. The acetylene deposition time was also varied from 2-15 minutes. These times had no obvious effect on the quality of tubes produced (figure 15).

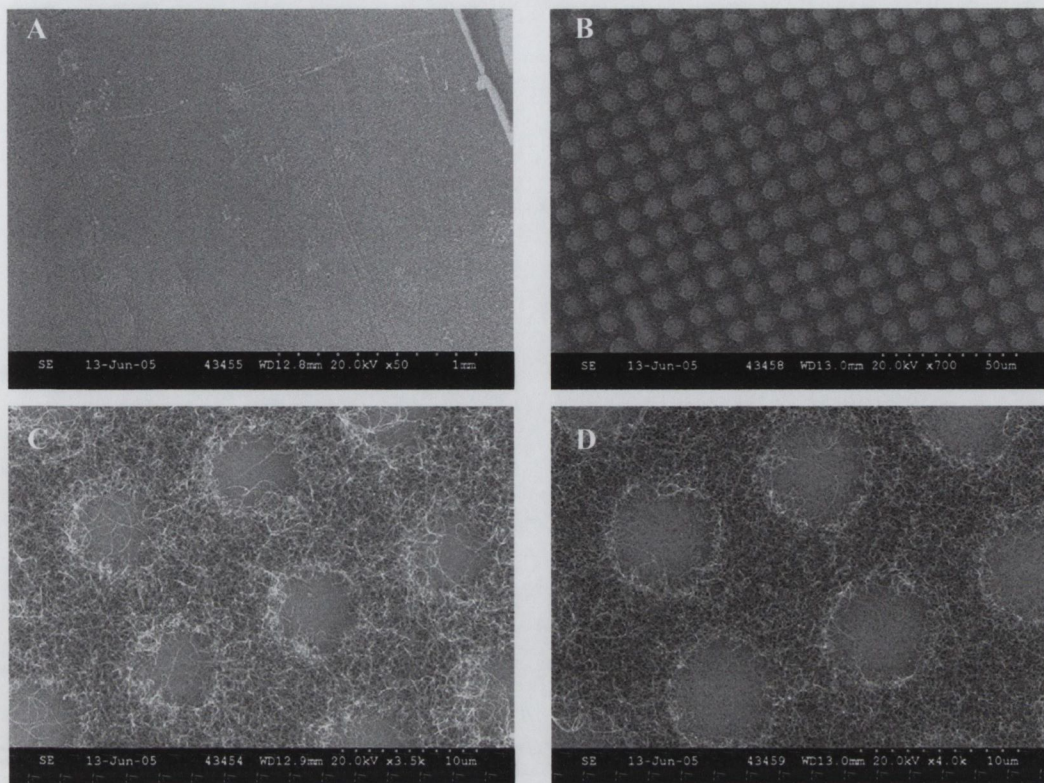


Figure 15: CNT arrays grown at the Max Planck Institute. Grids shown here have a $5\mu\text{m}$ separation. Figure A shows CNT arrays over an area $\sim 4\text{mm}^2$. This image is magnified in B. Figure C shows CNTs produced by 5 minutes ammonia pre-treatment followed by 2 minutes of acetylene. Figure D, shows results for 10 minutes of ammonia followed by 10 minutes acetylene.

It was noticed that when inter-grid separations are reduced to $5\mu\text{m}$, some definition is lost. Elastomer stamps used to pattern the substrates are cast from silicon masters. These masters in turn are patterned by photolithography. As pattern dimensions become smaller it becomes more difficult to etch precise patterns using photolithography. As a result, edges often lose their sharpness. This lack of clear resolution transfers to elastomer stamps cast from the masters. It was observed that for grid spacings of $5\mu\text{m}$, the corners of grid patterns became rounded (figure 16).

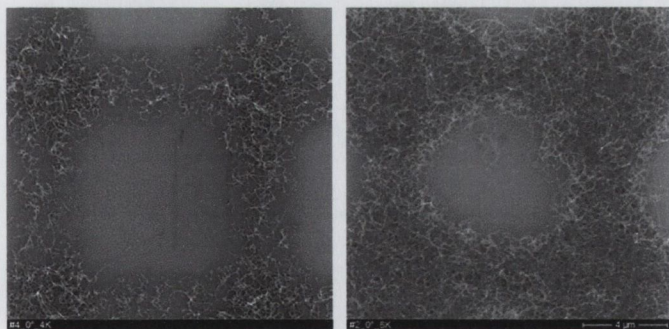


Figure 16: Pattern edges become rounded as dimensions are reduced. Grid spacings are reduced from 10 to 5 μm (left to right). Images were taken using the SEM at the Max Planck Institute.

The very first experiments done using poly(styrene-vinylferrocene) as a catalyst for CNT growth were done in Prof. Ajayan's research group in Rensselaer Polytechnic Institute. There we used xylene, rather than acetylene, as the carbon source (figure 17). Xylene is an aromatic liquid solvent which has the formula C_8H_{10} . Samples are placed in a horizontal tube furnace pumped down to 4×10^{-1} mbar. An argon/hydrogen gas mix, containing <10% H_2 , is then introduced and the system is heated to 790°C. The xylene is pre-heated in an external bubbler to 150°C for 5 minutes prior to being released into the chamber. Ar/ H_2 gas is switched off as the xylene enters the chamber. The valve to the mechanical pump is closed. Xylene vapours circulate in the CVD chamber for 5 minutes during which time CNT growth occurs. After CVD, the Ar/ H_2 gas is switched on and the valve to the pump is opened. The furnace is then cooled to room temperature before removing the substrates.

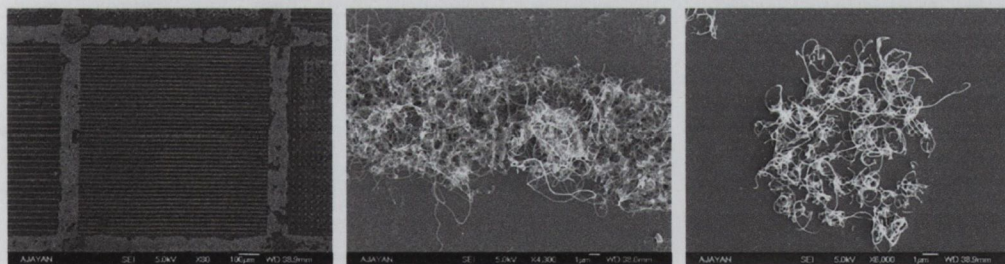


Figure 17: CNTs grown on line and dot patterns using xylene as the carbon source.

Prof. Ajayan's group have had much success growing CNTs onto silicon oxide using ferrocene as the catalyst material. They pre-heat ferrocene and introduce it in the vapour phase along with xylene. Other CVD conditions are the same as mentioned above. Using this technique controlled CNT architectures have been produced [18]. This process can be used to grow aligned CNTs onto patterned silicon oxide substrates. Patterns can be etched

into the silicon oxide substrates so that bare silicon is exposed in specific areas. CNTs will then grow selectively on the oxide. Nanotubes grow aligned perpendicular to the substrate. Figure 18 shows CNTs grown onto 500 μm diameter silicon oxide circles. For our particular application of polymer reinforcement, we do not require aligned CNTs. We also prefer to use soft lithography catalyst patterning rather than the photolithography patterning which is required for etching silicon oxide substrates. However for some applications where one-dimensional composite reinforcement is desired, this ferrocene/xylene growth process may potentially be useful.

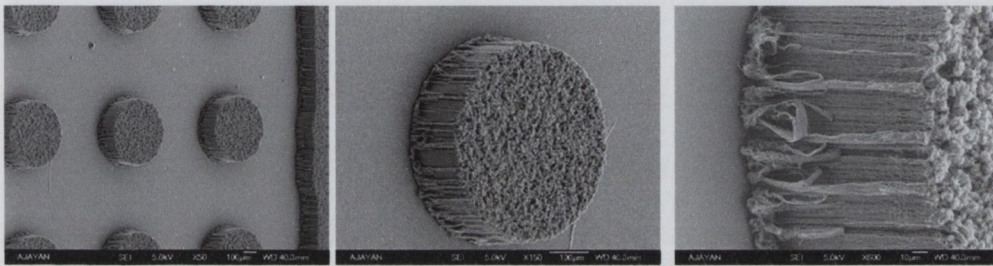


Figure 18: Using a ferrocene/ xylene mixture (typically 10% ferrocene) excellent CNT alignment was achieved. The tubes grow on silicon oxide in preference to silicon. Magnification of FESEM images increases from left to right.

5.6 Problems with producing large scale arrays

While it is possible to selectively grow CNTs onto patterns using poly(styrene-vinylferrocene) as the catalyst, it is difficult to produce large scale arrays. We estimate that the maximum area over which we could produce ordered CNT arrays was $\sim 6\text{mm}^2$. Often areas were smaller. It is unclear what exactly the limiting factor is. Large-scale arrays have been produced by Infineon Technologies on wafers up to six-inches in diameter. This proves that it is not the CVD process itself which is flawed. It is more likely that the deviation in our results is due either to the catalyst composition or the interaction between the catalyst and substrate.

It is clear from section 5.5 that patterned CNT growth can be achieved, using the catalyst poly(styrene-vinylferrocene), under a number of different CVD conditions. Hydrogen and ammonia do not appear to enhance the quality of tubes produced and in fact tubes of equal quality were grown using the basic argon/acetylene process. The growth of CNTs is also not exclusive to the use of acetylene, and xylene was seen to also be an effective carbon source.

Figure 19A shows a low magnification image of nanotube arrays with inter-grid separations of $75\mu\text{m}$. The pattern shows good uniformity over certain areas on the substrate. However, patterned CNT growth is confined to isolated sections on the substrate and random CNT growth occurs between these areas. Within patterned sections, defects can occur where the periodicity of the pattern is disrupted (figure 19B).

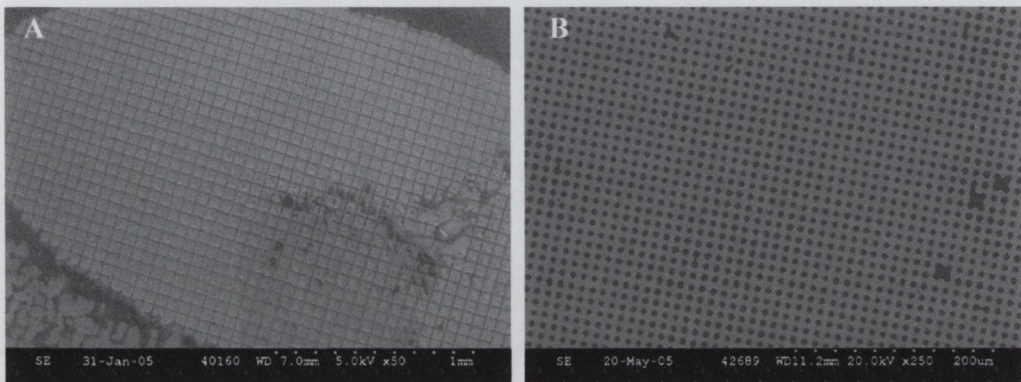


Figure 19: The growth of patterned nanotubes arrays is not uniform over the entire substrate surface (A). Within patterned areas sometimes defects occur (B).

Defects can be caused during soft lithography patterning where an elastomer stamp is used to transfer catalyst solution onto a substrate. If features moulded into the elastomer stamp are well separated, sagging between pillars can occur (inset figure 20A). This causes catalyst material to be deposited in areas intended to be catalyst free. As a result, CVD grown nanotubes will be observed in the centre of grid patterns as well as within grid lines (figure 20A). It has been demonstrated that attaching a rigid back plate to elastomer stamps prevents sagging [19-20].

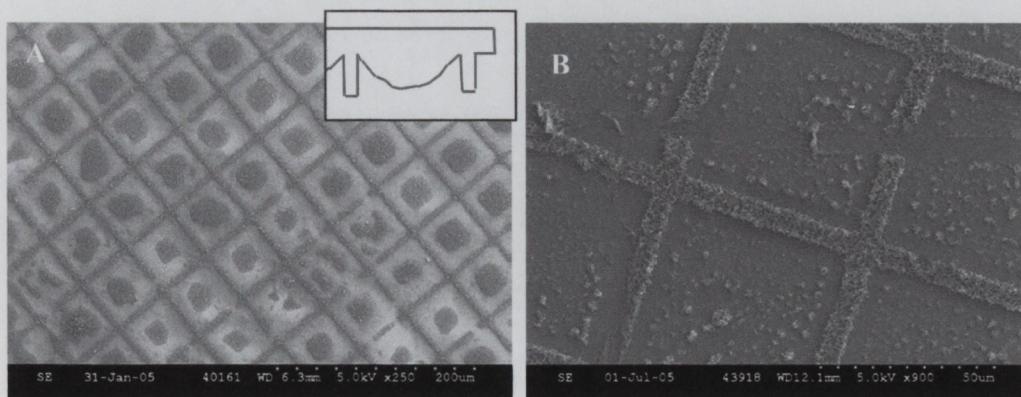


Figure 20: Pattern defects can be caused by sagging between the pillars of an elastomer stamp (A). Discontinuities can also occur within the dimensions of the patterns (B).

Defects can also occur within pattern borders (figure 2B). It is not immediately obvious why this occurs. Perhaps it is a result of damaged or scratched elastomer stamps. Feature sizes on a stamp are on the micron scale meaning that any damage caused is not obvious to the naked eye and can go undetected.

5.7 Conclusion

We have shown that poly(styrene-vinylferrocene) can be used to catalyse carbon nanotube growth. By controlling the conditions under which tubes are produced it is possible to control their morphology. In this chapter we demonstrated control over the diameter, density and position of nanotubes. We also showed that we could produce CNTs with very little amorphous carbon present. Unfortunately, this technique of nanotube growth was limited in that we were unable to produce large-scale arrays. For future research it may be possible to scale up the production of CNT arrays using this technique. This could be achieved by incorporating wave-printing technologies as mentioned in chapter 2 [19-20].

5.8 References

- [1] M Meyyappan, L Delzeit, A Cassell, D Hash, *Plasma Sources Sci. Technol.*, 12, 205-216, 2003.
- [2] K Hernadi, A Fonseca, JB Nagy, A Siska, I Kiricsi, *Appl. Catal. A*, 199, 245, 2000
- [3] YJ Jung, B Wei, R Vajtai, PM Ajayan, Y Homma, K Prabhakaran, T Ogino, *Nano Lett.*, 3(4), 561, 2003
- [4] A Cao, PM Ajayan, G Ramanath, R Baskaran, K Turner, *Appl. Phys. Lett.*, 84(1), 109, 2004
- [5] SB Sinnott, R Andrews, D Qian, AM Rao, Z Mao, EC Dickey, F Derbyshire, *Chem. Phys. Lett.*, 315, 25, 1999.
- [6] C Klinke, JM Bonard, K Kern, *Phys. Rev. B*, 71, 035403, 2005.
- [7] JM Bonard, N Weiss, H Kind, T Stockli, L Forro, K Kern, A Chatelain, *Adv. Mater.*, 13(3), 184, 2001
- [8] J Sandler, MSP Shaffer, T Prasse, W Bauhofer, K Schulte, AH Windle, *Polymer*, 40, 5967, 1999.
- [9] R Seidel, GS Duesberg, E Unger, AP Graham, M Liebau et al, *J. Phys. Chem. B*, 108, 1888, 2004
- [10] O.A. Nerushev, S. Dittmar, R.E. Morjan, F. Rohmund, E.E.B. Campbell, *J. Appl. Phys.*, 93 (7), 4185, 2003.
- [11] KBK Teo, M Chhowalla, GAJ Amaratunga, WI Milne, DG Hasko et al, *Appl. Phys. Lett.*, 79(10), 1524
- [12] GS Duesberg, AP Graham, M Liebau, R Seidel, E Unger et al, *Nano Lett.*, 3 (2), 257, 2003
- [13] RG Lacerda, AS The, MH Yang, KBK Teo, NL Rupesinghe et al, *Appl. Phys. Lett.*, 84(2), 269, 2004
- [14] AunShih Teh, part of Prof. Bill Milne's research group, University of Cambridge, UK.
- [15] Georg Duesberg, Infineon Technologies AG, Corporate Research, 81739 Munich
- [16] F Kreupl, AP Graham, GS Duesberg, W Steinhogel, M Liebau, *Microel. Eng.*, 64, 399, 2002
- [17] Martii Kaempgen, of Prof. Siegmur Roth's Research Group, Max Planck Institute, Stuttgart, Germany.
- [18] BQ Wei, R Vajtai, Y Jung, J Ward, R Zhang, G Ramanath, PM Ajayan, *Nature*, 416, 495, 2002.

[19] MMJ Decre, R Schneider, D Burdinski, J Schellekens, M Saalmink et al, Mat. Res. Soc. Symp. Proc., Vol. EXS-2, M4.9.1

[20] J Schellekens, D Burdinski, M Saalmink, M Beenhakkers, G Gelinck et al, Mat. Res. Soc. Symp. Proc., Vol. EXS-2, M2.9.1

Chapter 6: Incorporation of Nanotube Arrays into a Composite

6.1 Introduction

As-grown carbon nanotube arrays were subsequently incorporated into a thin film polymer matrix. This was achieved by spin coating a curable polymer directly onto the substrate from which the tubes are grown. Once cured, the composite can be peeled away from the substrate to produce a free-standing polymer-nanotube film. This method of composite synthesis allows the density and location of CNTs to be tailored. Therefore, it is possible to control the position of conduction channels through the insulating polymer matrix. The need for additional processing steps such as nanotube dispersion is eliminated. This composite production technique was first published by us, and has been included in a patent application entitled, "Embedding Nanotube Array Sensor and Method of Making a Nanotube Polymer Composite" [1,2]. The technology can be licensed from the Office of Technology Commercialization, at Rensselaer Polytechnic Institute in New York.

6.2 The Silicone Elastomer Matrix

The polymer used for the composite matrix is a silicone elastomer called Sylgard 184 (Dow Corning). This is a transparent, flexible elastomer which cures quickly under atmospheric conditions. Sylgard 184 is supplied as a two-part kit containing a base and a curing agent. The two are mixed together to form a viscous solution. This can be poured into a mould of any shape prior to curing.

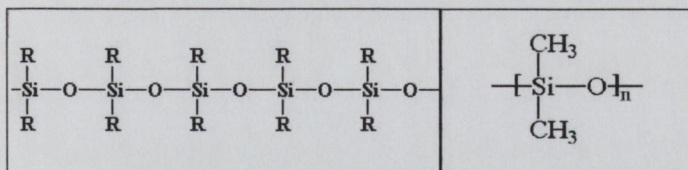


Figure 1: Silicone polymers consist of a silicon-oxygen backbone, as shown on the left. The structure of poly(dimethylsiloxane) is shown on the right.

All silicone polymers consist of a silicon-oxygen backbone with side groups attached. They are based on the structural unit R_2SiO , where R is an organic functional group (figure 1). The most commonly used silicone is poly(dimethylsiloxane), which has methyl side groups ($\text{R} = \text{CH}_3$). Key properties of silicones include thermal stability, chemical stability,

low water absorption, electrical insulation and low toxicity. Sylgard 184 contains a mixture of silicone polymers which are similar in structure to poly(dimethylsiloxane). It is most commonly used for electronic encapsulation applications. The material is supplied by Dow Corning as a two-part system. The base and a curing agent are mixed together in the ratio of 10:1. Curing occurs after 24 hours at room temperature and over shorter time periods if the temperature is increased. It takes a full week however for the polymer to reach full mechanical strength. Once cured, the material is stable over a wide temperature range (from -55 to 200°C) [3]. Sylgard 184 is a hydrosilylation cured system. The principal components are basic poly(dimethylsiloxane) polymer chains of various lengths capped with dimethylvinyl groups and dimethylhydrogen [4]. It also contains a silicate for reinforcement and a catalyst. The catalyst provides the transition metal (Pt) necessary for curing by addition across unsaturated bonds.

Sylgard 184 is a non-toxic material thus making it safe to handle. It has no cure by-products, which simplifies the fabrication process removing the need for venting and the possibility of shrinkage during production. It is flexible and provides relief from mechanical shock and a low transmission of vibrations. It has good dielectric properties making it suitable for electrical insulation. It is also stable and flame resistant. The lack of carbon-carbon double bonds in the backbone makes it less susceptible to oxidation than other polymers. Also, it is hydrophobic and has a low water absorption (after 7 days immersion at 25°C only 0.1% absorption occurs [3]).

6.3 Composite Fabrication

Sylgard 184 base and curing agent are added together to produce a medium viscosity mixture. The mixture must be left to settle for at least an hour, under atmospheric conditions, to eliminate any air bubbles introduced by mixing. Once the air bubbles have dissipated, the solution can be spin coated onto the nanotube arrays produced by CVD. The spin speed can be adjusted depending on the composite thickness required. For thicker film, the Sylgard 184 solution can be drop cast onto CNT arrays.

The medium viscosity of the polymer mixture allows it to flow and intercalate in between CNTs grown from a substrate. It should fill all inter-nanotube vacancies. The nanotube-polymer matrix is then left to solidify at room temperature. Full cure is obtained after seven days. The resultant composite is then simply peeled away from the substrate to

produce a freestanding flexible film (figure 2). During CVD nanotubes grow attached to the substrate, these tubes become securely embedded in the elastomer and detach from the substrate as the cured composite is peeled away. The location of nanotubes within the film can be controlled by soft lithography patterning of a catalyst material onto substrates prior to CNT growth. The density of tubes can be controlled by varying the concentration of the catalyst used in tube growth.

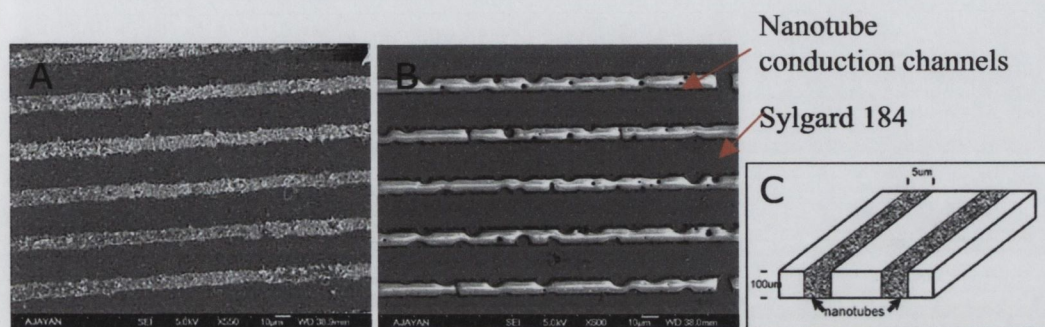


Figure 2: FESEM image of nanotubes grown on a SiO_2 substrate (A). Tubes are subsequently integrated into a polymer matrix to produce nanotube-containing channels separated by pure Sylgard 184 (B). Schematic of a thin film composite with nanotubes lines $5\mu\text{m}$ wide incorporated into a composite $\sim 100\mu\text{m}$ thick (C).

Using this technique of composite production we have a high level of control over nanotube morphology and orientation within a composite. We have also eliminated nanotube dispersion as a processing step. By growing nanotubes using CVD, rather than arc discharge or any other technique, we can produce clean nanotubes and therefore eliminate the need for purification. Combining all these advantages together make this a very attractive and simple method for composite fabrication.

6.3.1 Composite Thickness

The composite thickness increases as spin speed decreases. Therefore, it can be controlled to within certain limits. It was determined that below $120\mu\text{m}$, films are too thin to be peeled from substrates without tearing. It was also observed that for very thin films, the Sylgard 184 matrix does not achieve full cure and remains in a tacky state. Therefore, it is desirable that films be greater than $120\mu\text{m}$ thick. Sylgard 184 films were cast onto silicon substrates. The spin speed was varied from 500-3,000 rotations per minute (rpm). The time was kept constant at 60 seconds. After curing, the polymer film was left on the substrate and the thickness was measured using a travelling microscope. This is more accurate than a

digital micrometer. Using a micrometer it can be difficult to ascertain exactly where the surface begins. The flexible nature of the elastomer means that the micrometer can press into the surface to give inaccurate readings. After plotting the elastomer film thickness against spin speed, it was clear that spin speeds of below 1000 rpm were required for a film thickness above 120 μm (figure 3). As a comparison, two elastomer films were peeled from substrates. Free standing film thickness' were measured to be 274 μm and 183 μm for spin speeds of 500rpm and 800rpm respectively. These values are consistent with the values in the graph below. Thinner films curled up once removed from the substrate and could not be measured. When nanotubes are incorporated into these thin films, it is likely that they cause a slight increase in thickness. However the values presented can be taken as a good estimate for composite film thickness.

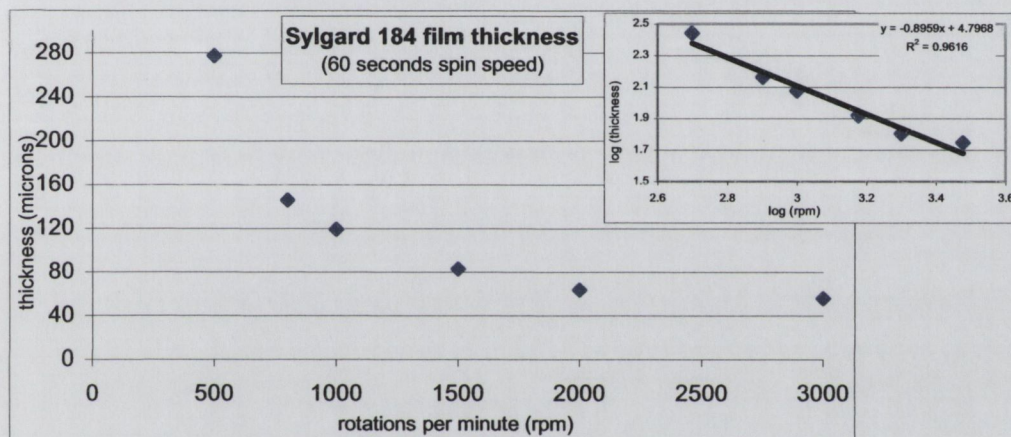


Figure 3: Elastomer film thickness decreases exponentially as spin speed increases, thickness $\propto (\text{rpm})^{-0.9}$. These values were measured using a travelling microscope.

6.4 The Composite Surface

Carbon nanotubes are highly conductive [5]. Incorporating them into a polymer introduces conduction channels into an otherwise insulating material [6]. The presence of nanotubes conduction channels through Sylgard 184 was confirmed by a combination of atomic force microscopy and electron force microscopy.

6.4.1 Atomic Force Microscopy

Atomic force microscopy is a type of probe microscopy used for imaging and manipulation at the nanoscale. The first type of probe microscopy developed was Scanning Tunnelling

Microscopy (STM) [7]. Binnig and Rohrer from the IBM labs in Zurich were awarded the Nobel Prize in 1986 for this invention. STM can be used to image atomic arrangements and relies on the quantum tunnelling of electrons between a probe tip and a sample surface. Both tip and surface must be conducting and separated by an insulating gap of $\sim 1\text{nm}$. The probe is moved across the sample surface and control of the tunnelling current across the tip-to-sample gap allows a sense of surface topography.

A modification of the STM technique led to the development of atomic force microscopy (AFM) [8]. AFM has the advantage of being able to image insulating surfaces. A probe tip is brought close to the sample surface where it experiences an interatomic attraction. As the sample-to-tip distance changes so too does the force experienced by the tip. Hence by maintaining a constant force at the tip, the tip will need to be moved closer and further away as it rasters across the dips and peaks of the sample surface. Hence the topography of the sample can be monitored.

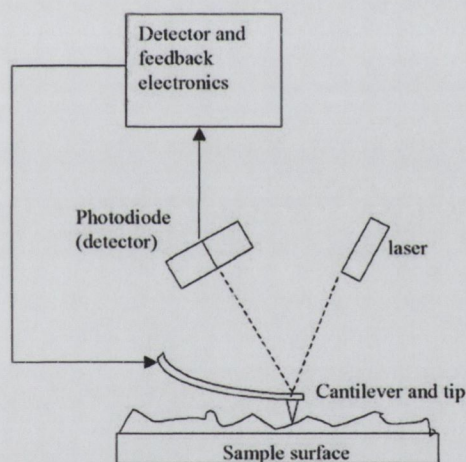


Figure 4: Schematic of an AFM set-up. (Taken from wikipedia.com.)

An AFM consists of a fine tip attached to a cantilever spring. The cantilever has a low spring constant and can respond quickly to interatomic force variations. The magnitude of this deflection is governed by Hooke's law and monitored using a laser beam focused on the back of the tip (figure 4). The laser reflects the light back onto a position-sensitive photodiode (PSPD) which can detect movement of the cantilever. Cantilevers must have a low mass to increase their resonant frequency (equation 1). AFM cantilevers are therefore very small with lengths typically of $125\text{-}450\mu\text{m}$ [8]. These tiny cantilevers are mounted on the end of chips which are typically $3.4\times 1.6\text{mm}$ [9]. The resolution of the AFM is limited

by the radius of the tip attached to the end of the cantilever. The tip radius is typically in the region of 30nm. Distances as small as 10Å can be measured.

$$f = 1/2\pi (k/m)^{1/2} \quad \text{equation 1.}$$

f = resonant frequency

k = spring constant

m = mass

The PSPD inputs information from the tip deflection into a feedback loop. The feedback loop is connected to the piezoelectric sample stage. The piezoelectric stage responds mechanically to electrical impulses and adjusts the Z-height of the sample depending on the information from the feedback mechanism. Hence the sample-to-tip distance (and force on the cantilever) is maintained constant throughout the scan. The piezoelectric stage is also responsible for moving the sample in the x-y direction during scanning.

AFM is a useful imaging tool and it can be used to produce 3-dimensional surface profiles. No sample treatment is required and scans can be obtained under ambient conditions. The scan speed is limited by the response time of the feedback circuit and is therefore slow. AFM can only image small areas (~100µm²) and cannot be used to image rough surfaces. It must also be isolated from vibrations to obtain optimum resolution.

Additions to an AFM system are available whereby topography and a second property, such as electric force, are measured simultaneously. During electric force microscopy (EFM), a conductive AFM tip (usually platinum coated) responds to long range Coulomb forces. The cantilever frequency changes in response to electric field gradients between the tip and sample surface. These fields can be generated by trapped charges. Alternatively, a field can be induced by applying a voltage between the tip and the sample. The location of conduction pathways across a sample surface can thus be determined.

6.4.2 Probing the Composite Surface

A combination of AFM and EFM can be used to obtain a height profile of the composite surface while simultaneously mapping the position of conduction channels through the film. It was observed that, as expected, the height profile of the composite correlated with the position of the conduction channels. The uneven height of the composite surface is due

to nanotubes protruding from the elastomer surface. The position of the nanotubes in the AFM scan matches the location of conduction paths in the EFM image (figure 5).

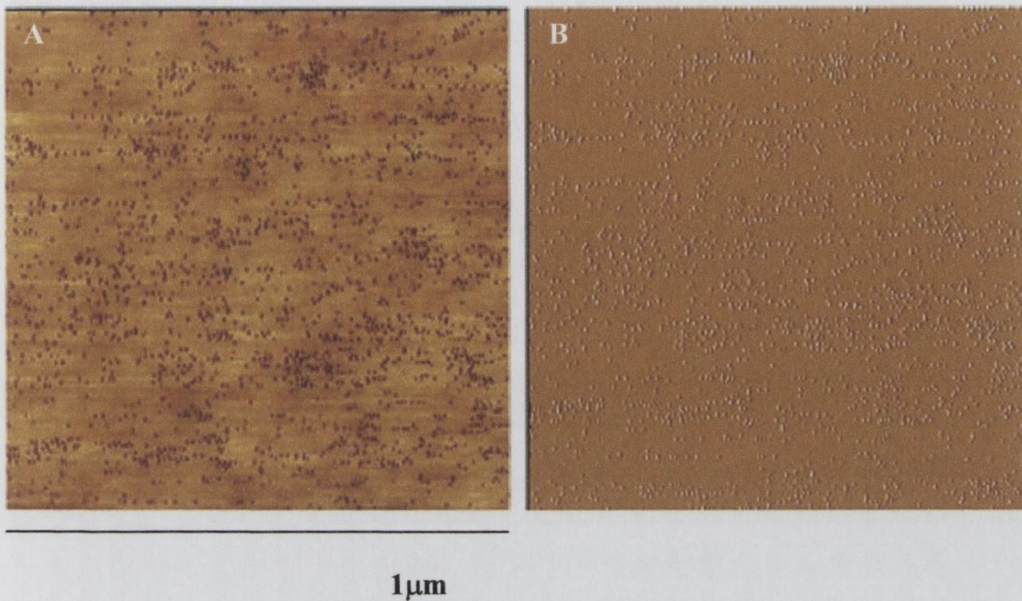


Figure 5: An AFM scan shows nanotubes protruding from the composite surface (A). An EFM scan across the same area shows the positions of conduction channels (B).

We have therefore shown that nanotubes can be used to introduce conduction pathways through an insulating matrix. The images shown in figure 4 were taken over a $1 \mu\text{m}^2$ section of the composite. This section displays a high density of protruding CNTs due to a large amount of embedded nanotubes beneath the surface. Areas of pure polymer regularly separate nanotube arrays within the composite. When a similar scan was taken over a polymer section of the composite it shows few nanotubes protruding from the surface (figure 6). These areas are therefore mainly insulating. Ideally, sections of the composite between nanotubes arrays should contain no CNTs. During CVD however, some sparse CNT growth occasionally occurs between patterned areas of the substrate. This is probably due to stray catalyst particles deposited during soft lithography patterning.

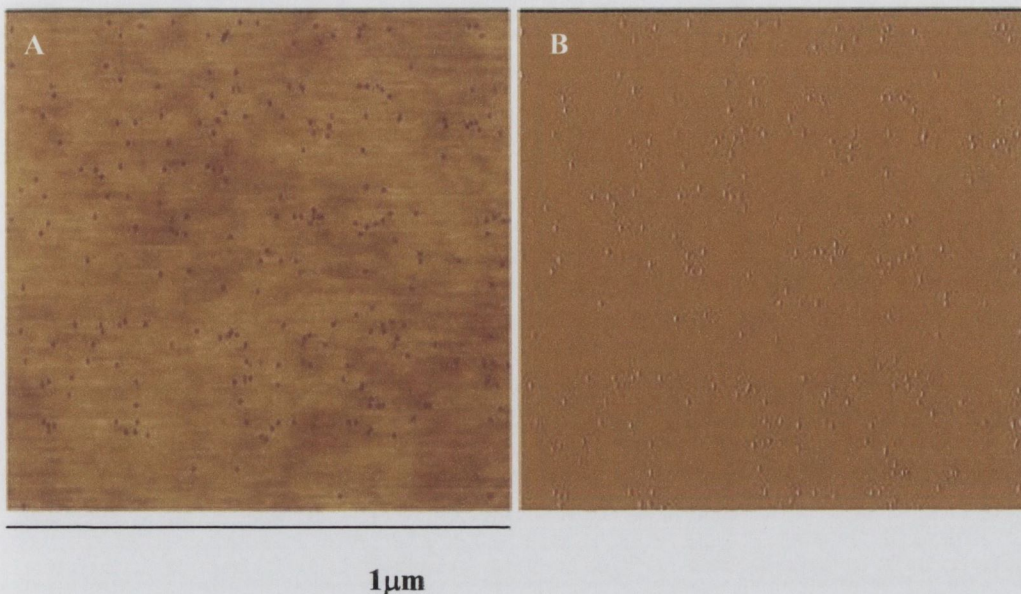


Figure 6: An AFM scan taken across a polymer section of the composite (A). An EFM scan over the same area shows very few conduction channels (B).

All results were taken at a scan rate of 0.5008Hz. The AFM images show height data on a scale of 0-10nm. The dots in AFM images, which correspond to protruding CNTs, have a uniform diameter of ~20nm. The average diameter of nanotubes used in the composite was measured by FESEM to be ~20nm. Considering that protruding tips should be coated with a polymer wetting layer, this indicates that it is possibly only the very tips of the tubes which protrude from the surface. Corresponding EFM images show amplitude data on a scale of 0-300mV. The dots in EFM images represent conduction channels through the insulating polymer matrix.

6.5 The Nanotube-Polymer Interface

The mechanical reinforcement of a composite is determined by the properties of the filler material. It also depends on the strength of the matrix-filler interface [10]. Nanotube fillers have a large surface area available for bonding to the matrix. Therefore strong coupling at the interface is possible. The interface between nanotubes and Sylgard 184 was investigated using FESEM (figure 7). This was tedious work as the polymer burns off at high electron acceleration voltages (greater than 5keV). However, for low accelerating voltages (less than 5keV) it is often difficult to obtain clear high-resolution images. Charging of the surface is also a problem due to the insulating nature of the polymer. The

composite was coated with gold to improve conductivity and make the samples easier to image. The gold layer must be very fine so as not to obscure the topology of the composite.

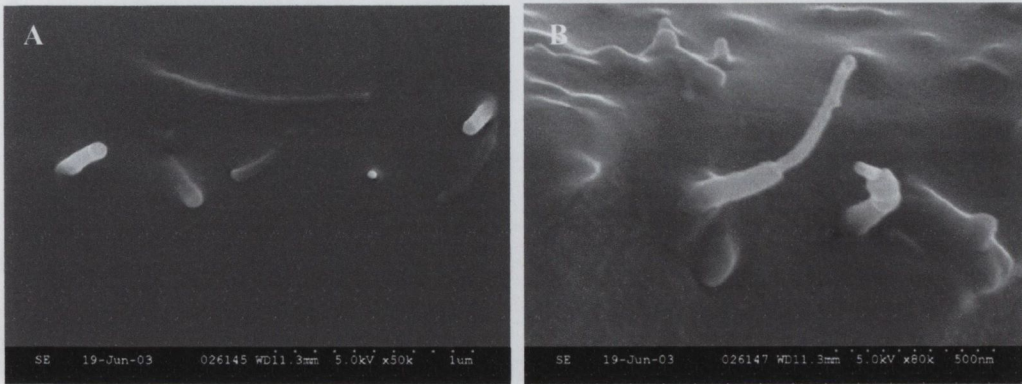


Figure 7: A FESEM image of nanotubes embedded within the elastomer matrix (A). Only the very tips of the tubes emerge from the surface. Figure B shows two protruding nanotubes covered in polymer this indicates good wetting.

Both nanotubes and Sylgard 184 are hydrophobic in nature [11]. This suggests compatibility and the possibility of a strong interface between the two materials. FESEM images show that nanotubes protruding from the composite surface are coated in polymer. This indicates good wetting behaviour at the interface. A favorable interaction between the two materials should allow for greater load transfer from the matrix to the nanotubes, thus enhancing the mechanical reinforcement provided by the tubes.

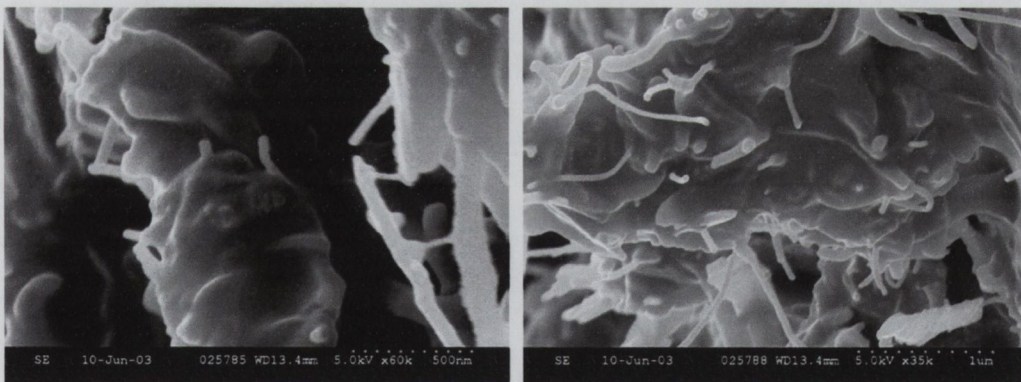


Figure 8: FESEM images of torn composite films show that nanotubes remain coated in polymer.

When composite films are torn, fracture occurs in the matrix. Images of the torn surface reveal that nanotubes remain coated in Sylgard 184 (figure 8). This shows that the nanotubes-polymer interface is stronger than the polymer-polymer interaction. A weak

interface would result in slippage between the tubes and polymer. Tubes would thus essentially be pulled from the polymer matrix. Fracture occurs at the weakest point in a material. The good wetting behaviour observed means that any fracture will occur in the matrix.

6.6 Macroscopic Composite Images

The composite production technique can be summarised as a four-step process. Step one is to grow nanotubes arrays by CVD. The second step is then to spin coat a curable polymer onto the as-grown tubes. The polymer is left to cure and finally, the composite is peeled from the substrate surface. This produces a free standing composite. When an elastomer, such as Sylgard 184, is used as the polymer matrix the resulting composite is extremely flexible. Where arrays are well separated, the nanotubes loading in the composite is relatively low. As a consequence the composite is either transparent or semi-transparent.

A substrate was patterned with a series of 1mm^2 sections. Each section contained either line or dot patterns. The lines were $10\mu\text{m}$ wide and dots were $10\mu\text{m}$ in diameter. Feature separations varied from $10\text{-}25\mu\text{m}$. Nanotubes grown from these patterns correspond to grey areas in figure 9A. These arrays are then incorporated into a composite. After curing, the composite is peeled from the substrate to produce a freestanding film (figure 9B). Black lines through the composite correspond to the location of embedded nanotubes. The composite is mainly transparent and a blue background is clearly visible behind it. The composite is also extremely flexible and can be bent repeatedly without causing damage (figure 9C).

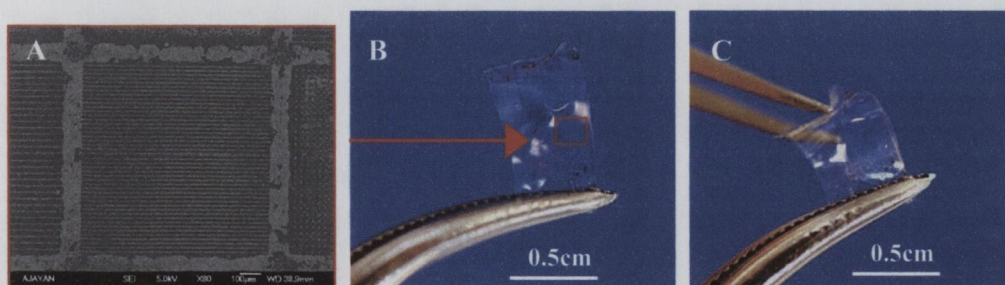


Figure 9: Controlled nanotube arrays (A) are embedded in an elastomer thin film (B). This produces a flexible composite (C).

6.7 Conclusion

The composite production technique described in this chapter can be used to control the position of carbon nanotubes conduction channels through a polymer matrix. This simple method could also be used to incorporate the grid patterns demonstrated in section 5.4 into a composite. The technique can be adapted to suit any nanotube geometry. Different polymer hosts could also be used where properties such as strength are required.

6.8 References

- [1] Lahiff E, Ryu CY, Curran S, Minett AI, Blau WJ, Ajayan PM, "Selective positioning and density control of nanotubes within a polymer thin film, " *Nano Letters*, 3, (10), 1333-1337 (2003).
- [2] P.M. Ajayan, E. Lahiff, P. Stryjek, C.Y. Ryu, S. Curran, Patent No. WO2004053464. Publication date 2004-06-24. Embedding Nanotube Array Sensor and Method of Making a Nanotube Polymer Composite.
- [3] Dow Corning Sylgard 184 data sheet
- [4] Sylgard 184 MSDS Sheet, Dow Corning
- [5] AY Kasumov, II Khodos, PM Ajayan, C Colliex, *Europhys. Lett.*, 34(6), 429, 1996
- [6] J Sandler, MSP Shaffer, T Prasse, W Bauhofer, K Schulte, AH Windle, *Polymer*, 40, 5967, 1999.
- [7] G Binning, H Rohrer, C Gerber, E Weibel, *Phys. Rev. Lett.*, 49(1), 57, 1982
- [8] G Binning, CF Quate, C Gerber, *Phys. Rev. Lett.*, 56(9), 930, 1986
- [9] http://www.nanoscience.com/products/AFM_cantilevers.html
- [10] PM Ajayan, L Schadler, C Giannaris, A Rubio, *Adv. Mater.*, 12 (10), 750, 2000
- [11] JH Walther, RL Jaffe, EM Kotsalis, T Werder, T Halicioglu et al., *Carbon*, 42, 1185, 2004.

Chapter 7: Physical Characterisation of Composites

7.1 Introduction

To characterise the properties of the composite, macroscopic samples must be tested. For example, samples for mechanical testing must be at least 1cm long. Using a combination of the catalyst poly(styrene-vinylferrocene) and soft lithography patterning it was difficult to produce large-scale uniform carbon nanotube arrays. The largest area over which we were able to produce a homogeneous CNT grid pattern was estimated to be $\sim 6\text{mm}^2$ (section 5.7). Therefore, rather than using nanotube arrays, blanket carbon nanotube films were incorporated into Sylgard 184. Resulting composites were characterised to quantify the reinforcement provided by embedded nanotubes.

7.2 Composites Tested

CNT blanket films were grown by CVD from a layer of poly(styrene-vinylferrocene) catalyst on a silicon oxide substrate. Uniform PS-PVF films were deposited by spin coating. The film thickness was determined by the spin speed and by the concentration of catalyst solution used. Thickness values for two different concentrations at three different speeds were measured using ellipsometry (figure 1). Film thickness was observed to depend primarily on concentration and doubled as the concentration of the catalyst solution was increased from 0.5 to 1 weight percent (wt%). The spin speed had less effect on thickness.

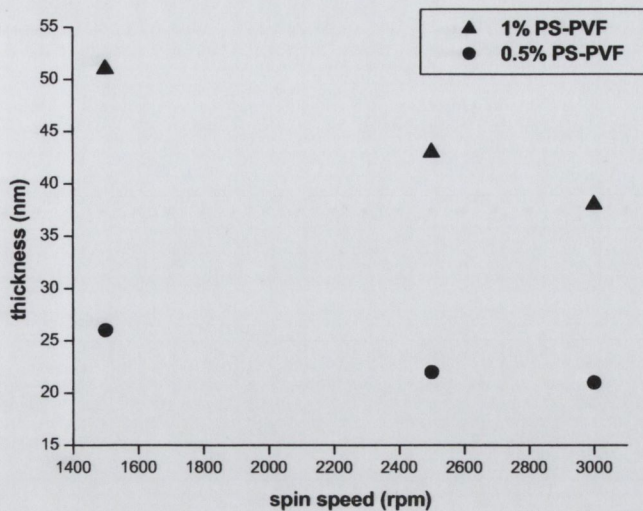


Figure 1: A PS-PVF catalyst layer is deposited by spin coating. The film thickness changes dramatically as the concentration of the catalyst solution is increased. The spin speed has less effect on film thickness.

CNTs were subsequently grown from these catalyst films by CVD. A 1wt% solution however produced only low density CNT growth. For composite measurements, we need to ensure the CNT concentration is above the percolation threshold. Therefore, catalyst films were spin cast using 4wt% solution. Nanotubes were then observed to grow in abundance over the entire substrate surface. FESEM images reveal the tubes to have a narrow diameter distribution from 77nm to 103nm with the majority of tubes being 85nm wide. These values include a 2x15nm gold layer making the actual diameter distribution from 47nm to 73nm with a peak at 55nm. This gold layer is deposited for imaging purposes and is absent from any CNT arrays incorporated into composites. Nanotubes are produced as an entangled spaghetti-like mat (figure 2). It is also possible to grow aligned nanotube forests, as demonstrated in section 5.4. When incorporated into a polymer host, aligned CNTs provide anisotropic one-dimensional reinforcement. We prefer to use randomly oriented tubes as they can be used to produce polymer reinforcement in three-dimensions.

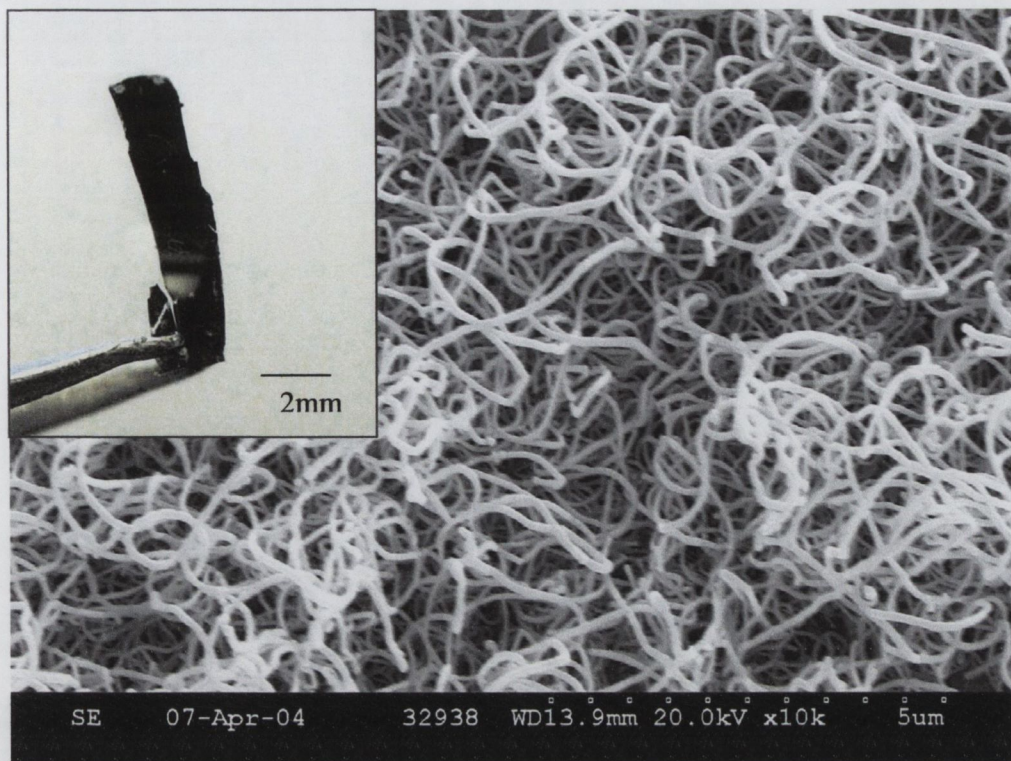


Figure 2: FESEM image of entangled NTs grown from a catalyst thin film spin cast onto a silicon oxide substrate. The inset shows a free standing composite film containing a similar CNT network embedded in Sylgard 184.

Composite formation was achieved by spin coating Sylgard 184 (base and curing agent mixed together) at 500rpm for 60 seconds onto the as-grown entangled nanotubes. The mixture intercalates into the free volume between the CNTs and can be left to cure under atmospheric conditions. After a period of seven days, the system is fully cured and the composite film can be peeled away from the substrate. This produces a freestanding, flexible thin film approximately 250 μ m thick. As seen from the inset of figure 2, the resulting composite is opaque due to the dense CNT network embedded throughout the transparent polymer matrix. Although we have chosen to use an elastomer in this work, any soluble polymer can be used for composite formation using this technique.

Prior to composite formation, CNT films grown on silicon oxide substrates appear black. After composite formation and cure, the composite is peeled away from the substrate. The substrate exposed is shiny and similar in colour to the original silicon oxide wafer prior to CNT growth. Therefore we conclude that the CNTs have been removed from the substrate and must be held within the polymer matrix. This indicates that a stronger interaction

exists between the CNTs and the elastomer than between the CNTs and the substrate from which they are grown. Composites made by this technique were subsequently characterised to quantify the electrical conductivity and mechanical reinforcement provided by the carbon nanotubes.

7.3 Electrical Conductivity

Electrical conductivity was measured using a two-point probe set-up. Gold electrodes were evaporated onto the composite films to act as low resistivity contacts ($\rho = 2.44 \times 10^{-8} \Omega\text{m}$ for Au [1]). A thin silver wire was then attached to each electrode using silver paint ($\rho = 1.47 \times 10^{-8} \Omega\text{m}$ for Ag [1]). These wires were connected to larger circuit wires via crocodile clips. It is not possible to obtain good electrical contact directly between thick circuit wires and the delicate gold electrodes. Silver wires acts as an intermediate and provide good contact with the thin gold electrodes. Composite films are thus incorporated into a circuit where a Keithley Model 2400 source-meter is used to provide a potential drop across the samples. The resulting current flow through the composite is measured with an ammeter. A diagram of the circuit is shown in figure 3.

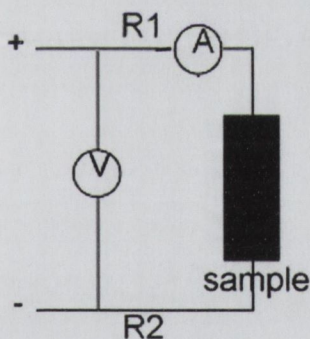


Figure 3: Diagram of the two-point probe set-up where a potential is applied across the sample. V represents the voltmeter and A is the ammeter. This set-up is only suitable for samples which have a resistance much greater than the contact resistance, R1 plus R2.

All samples to be measured are made either using a silicone elastomer. Silicone is an electrically insulating material. Composites are made by incorporating CNTs into this insulating matrix. This is expected to result in an increase in conductivity. However, due to the insulating nature of the elastomer matrix, conductivity values are not expected to rise beyond that of a doped semiconductor. The conductivity values for the gold and silver contacts are in the metallic region, and therefore significantly higher. As sample resistance

is much greater than the resistance of the contacts, a two-point probe arrangement is sufficient for conductivity measurements. Only where samples have low resistance, the resistivity of the contacts becomes important. Four-point probe measurements are then necessary to eliminate the effects of contact resistance [2]. In a four-point probe set-up, a current is applied across the outer two probes attached to a sample surface. The resulting potential drop is measured across the inner two probes. Because all four probes are attached to the sample surface, it is not possible to measure volume resistivity using this technique. A two-point probe arrangement can be used to obtain both surface and volume resistivity values. These values are accurate only for samples with relatively high resistivities.

It is obvious from figure 3 that the potential drop (V) is measured not only across the sample but also across the two connecting wires and gold contacts (R_1 and R_2). This contact resistance reduces the current flow through the sample by an amount which can be calculated using Ohm's law (equation 1).

$$V = I (R_1 + R_s + R_2)$$

Equation 1.

I = current flow in the circuit

R_s = resistance of the sample

R_1 = resistance across lead 1 plus contact 1

R_2 = resistance across lead 2 plus contact 2

Contacts consist of silver wires attached to gold electrodes. The resistance of these contacts is therefore extremely low. Where sample resistance (R_s) is high, contact resistance (R_1 and R_2) becomes negligible. The resistance of our samples is sufficiently high that any contact resistance has no significant effect on the conductivity results obtained. It can therefore be ignored

As already mentioned, probes were connected to samples via gold electrodes. To deposit the electrodes, samples were placed in a bell jar ~20cm above a small amount of coiled gold wire. The jar was evacuated to 2×10^{-6} mbar. The gold wire was heated by passing a current of 2 Amperes through it. As the gold begins to melt, it evaporates. A gold layer is deposited onto all surfaces in the bell jar, including the exposed sample surface. Deposition time is such that 50nm thick gold layers were deposited onto our samples.

The bottom of sample films was coated with a continuous gold layer. Six isolated rectangular gold electrodes were deposited onto top surfaces. In order to deposit six rectangular electrodes onto the upper surface, wires ($\sim 330\mu\text{m}$ wide) were placed over the sample in a grid formation prior to evaporation. After gold evaporation, the wires were removed to reveal uncoated areas beneath. These spacings between electrodes were measured using a travelling microscope and separations were found to vary between $270\mu\text{m}$ and $400\mu\text{m}$. To avoid short-circuits, sample edges should be kept free of gold. This was achieved by covering sample edges with aluminium foil. Silver wire contacts could be subsequently attached to gold electrodes using silver paint.

Using this electrode configuration, it is possible to measure both the surface and the volume resistivity of each sample. Surface resistivity can be measured by contacting two adjacent surface electrodes and measuring the current flow over a range of voltages. These values can be used to produce a current-voltage (I-V) plot. Bulk resistivity can similarly be measured by connecting one surface electrode to the continuous bottom electrode (figure 4).

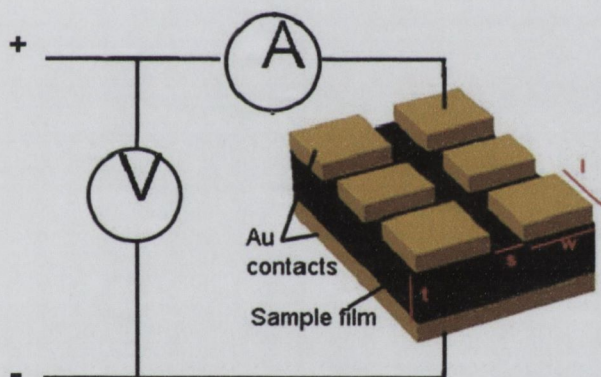


Figure 4: A schematic of gold contacts evaporated onto a composite thin film (in black). The bulk conductivity of the sample can be measured by connecting one wire to the base electrode and a second wire to one of the top electrodes. Surface conductivity can also be measured by connecting wires across any two adjacent top electrodes.

All our electrical measurements were made in direct current (DC) mode. Where NT loading is below the level required for conduction, alternating current (AC) measurements can be used to determine the onset of percolation. The frequency of the AC potential is varied and the NT concentration where percolation occurs can be calculated. We are well above the percolation threshold however, so DC measurements are sufficient.

I-V curves obtained were linear at low voltages but tended to become super-linear outside the region $\pm 10V$. The linear I-V relationship obtained for composite samples at low applied voltages indicates that conduction in this region is dominated by CNTs (which are ohmic conductors). At higher voltages plots become super-linear. We suggest that this is most likely due to the onset of tunnelling between adjacent tubes. The initial ohmic regions of the I-V plots can be used to calculate a value for the DC conductance of each composite sample. Conductance can then be converted to conductivity values.

Conductance (G) is a measure of how well electric current flows through a material. It is measured in Siemens (S). More specifically, conductance can be defined in terms of the amount of current flow for a particular potential drop across a sample. One Siemen is therefore equivalent to one ampere per volt (equation 2). From Ohm's law, it can be deduced that conductance is inversely proportional to resistance.

$$G = I/V = 1/R$$

Equation 2.

G = conductance (siemens, S)

I = current (amperes, A)

V = voltage (volts, V)

R = resistance (ohms, Ω)

Conductance values are therefore equivalent to the slope of the linear region of I-V plots obtained for our composite samples. Conductance values can be measured either across the bulk or across the surface of samples (figures 5 and 6).

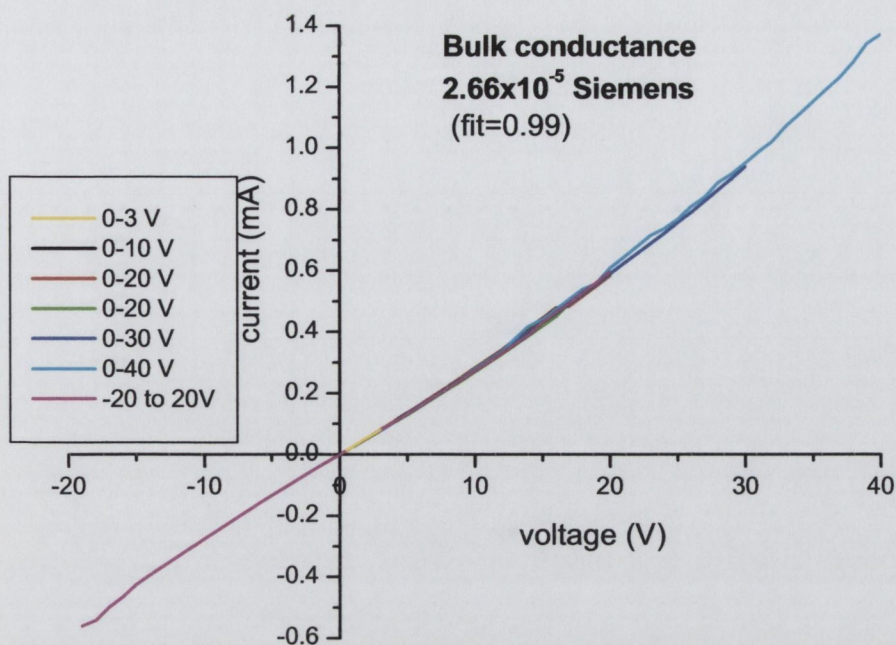


Figure 5: A typical series of I-V plots obtained across the bulk of a composite thin film. The slope of the linear region of the graph gives a bulk conductance of 2.7×10^{-5} S. Conductance values are stable over seven measurements as the voltage range is gradually expanded to between -20 and 20 V.

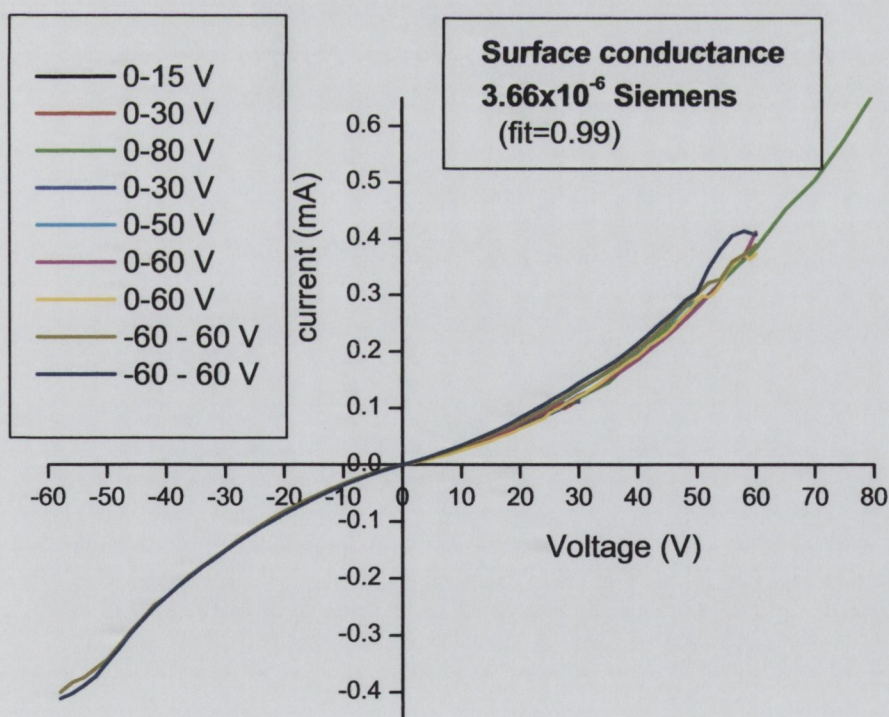


Figure 6: A typical series of I-V plots obtained across the surface of a composite thin film. Surface conductance is 3.7×10^{-6} S and is stable over ten measurements as the voltage range is expanded to between -60 and 60 V.

Conductance values can be translated into conductivity provided the dimensions and separation of electrodes are known. Conductivity is defined as the ratio of current density to the magnitude of an applied electric field (equation 3). Conductivity is the inverse of resistivity.

$$\sigma = J / E = 1 / \rho \quad \text{Equation 3.}$$

σ = conductivity (S/m)

J = current density (A/m²)

E = electric field (V/m)

ρ = resistivity ((Ω -m))

For bulk conductivity measurements, the electric field is applied over the thickness of the composite film. The current density is therefore equivalent to the current per cross-section area of electrode (equation 4). The bottom of the composite is coated with a continuous gold layer. Therefore, the electrode area is determined by the surface electrode. This area is calculated as a product of the length (l) and width (w) as shown in figure 4. All electrodes do not have the same surface area and values range from 11mm² to 27mm² (table 7.1).

$$\sigma_v = J / E = (I/A) / (V/t) = G * t/A \quad \text{Equation 4.}$$

σ_v = bulk conductivity (S/m)

G = conductance (S)

t = sample thickness (m)

A = electrode surface area (m²)

For surface conductivity, the electric field is applied between two adjacent electrodes. Therefore current density is equivalent to the current per unit length (linear current density). Surface conductivity depends on the electrode separation and the length of the electrode edge along the separation gap (figure 4).

$$\sigma_s = J / E = (I/l) / (V/s) = G * s/l \quad \text{Equation 5.}$$

σ_s = conductivity (S/ \square)

G = conductance (S)

s = electrode separation (m)

l = length of electrode along separation (m)

Numerical values for the length (l), width (w), separation (s) and thickness (t) were measured using a travelling microscope. The travelling microscope can measure distances to an accuracy of $\pm 0.001\text{cm}$ ($10\mu\text{m}$). Composite thickness values were measured to lie between $240\mu\text{m}$ and $280\mu\text{m}$. Films are cast by spin coating and so variations in the thickness are not due to an inhomogeneous film thickness. Rather they are a result of the fact that measurements are subjective and open to the interpretation of the observer. The range of values is therefore unlikely to be reduced even if the number of measurements made increases. A thickness of $250\mu\text{m}$ is expected for Sylgard 184 deposited at a spin speed of 500rpm for 60 seconds (chapter 6, figure 3). This lies within the range of values measured. Composite thickness measurements are especially tedious, as samples must be viewed from the side. It is therefore much simpler (while remaining accurate) to adopt a thickness of $250\mu\text{m}$ for all samples. Average values measured for length (l), separation (s) and cross-section area (A) are shown in table 7.1. These values are used to convert conductance to conductivity using equations 3 and 4.

Table 7.1: Values of t, A, s and l used to convert conductance measurements to conductivity.

Sample number	conductance (S)	t (m)	A (m ²)	$\sigma_v (=G*t/A)$ (S/m)	Sample number	conductance (S)	s (m)	l (m)	$\sigma_s (=G*s/l)$ (S/□)
1	4.17E-06	2.50E-04	1.32E-05	7.90E-05	1	2.23E-05	3.00E-04	3.19E-03	2.10E-06
2	2.66E-05	2.50E-04	1.14E-05	5.83E-04	2	1.06E-03	4.10E-04	4.49E-03	9.68E-05
3	1.56E-06	2.50E-04	1.18E-05	3.30E-05	3	6.44E-04	4.10E-04	6.49E-03	4.07E-05
4	1.23E-04	2.50E-04	2.53E-05	1.21E-03	4	8.07E-05	2.70E-04	5.79E-03	3.76E-06
5	1.39E-04	2.50E-04	2.71E-05	1.28E-03	5	6.88E-05	3.50E-04	4.37E-03	5.51E-06
6	2.95E-05	2.50E-04	2.25E-05	3.28E-04	6	1.39E-04	4.00E-04	4.68E-03	1.19E-05
7	3.90E-05	2.50E-04	2.41E-05	4.05E-04	7	1.28E-04	2.70E-04	5.14E-03	6.71E-06
8	1.79E-05	2.50E-04	1.10E-05	4.08E-04	8	1.19E-05	2.70E-04	2.55E-03	1.26E-06
9	5.28E-07	2.50E-04	1.65E-05	8.00E-06	9	4.44E-04	2.70E-04	2.62E-03	4.58E-05
10	1.62E-06	2.50E-04	1.70E-05	2.38E-05					

The bulk conductivity was calculated for ten composite samples to produce a mean value of $(4.4\pm 4.7)\times 10^{-4}$ S/m. The main source of error was the difficulty in accurately measuring small distances, in this case composite thickness (t). The dimensions of the electrodes were easier to measure as they are an order of magnitude larger. The surface conductivity was measured across nine electrode pairs to produce a mean value of $(2.4\pm 3.2)\times 10^{-6}$ S/□. Again the main source of error was incurred when measuring small distances, in this case the electrode separation (s).

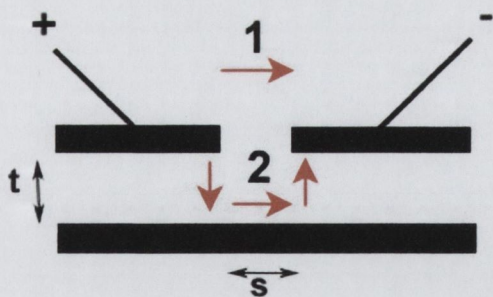


Figure 7: The surface conductivity is measured using an I-V plot obtained by connecting two adjacent surface electrodes. It is assumed that electrons follow path 1. However, the sample thickness is of the same order of the electrode separation and the possibility that electrons follow path 2 has to be considered.

When calculating surface conductivity, we assume that electrons follow the shortest path to the adjacent electrode (path1, figure 7). However, sample thickness is of the same order of the electrode separation and it is possible that electrons may encounter less resistance by travelling through the bulk of the composite rather than across the surface (path 2, figure). The distance travelled by electrons would then be twice the sample thickness plus the electrode separation ($2t + s$). This can be approximated to $3t$, as s and t are approximately equal in our set-up. If the value calculated for σ_s (10^{-6} S/ \square) was in fact a bulk conductivity, it's value would be $1/3 \sigma_v$ (10^{-4} S/m). This is due to the fact that electrons would be travelling three times the distance, $3t$. The value is however two orders of magnitude less than σ_v (10^{-6} vs 10^{-4}). Therefore we can say with certainty that it is a surface conductivity value and not due to electron transport through the bulk.

While the conductivity was observed to degrade after successive measurements, potentials of up to 100V could be dropped across the composites repeatedly without destroying conductive pathways. Conductance values were stable over at least eleven measurements (figure 8).

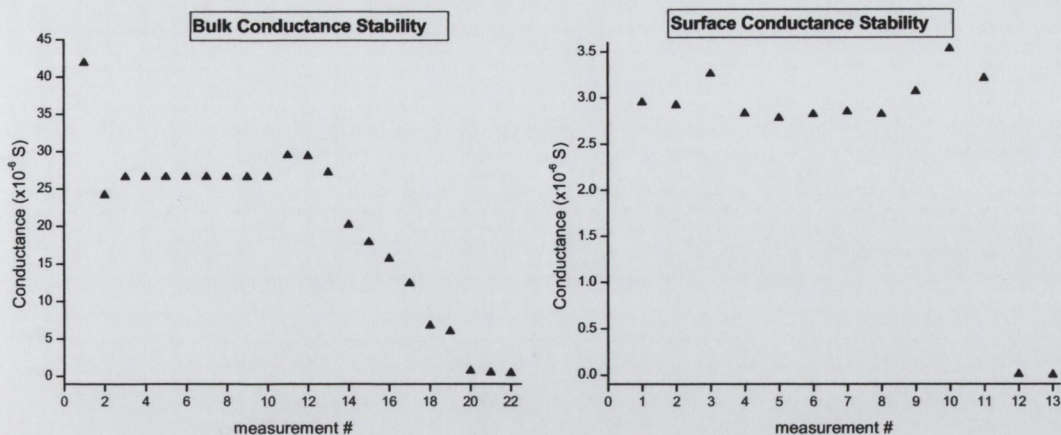


Figure 8: Conductance values are stable for a minimum of eleven measurements.

Composite conductivity values were compared to values for Sylgard 184 thin films containing no CNT reinforcement. Elastomer control samples were made by spinning a Sylgard 184 mixture at 500rpm for 60 seconds onto a Teflon substrate. Sylgard 184 will adhere to silicon substrates. Cured films can be more easily removed from Teflon. As always, the mixture was left to settle before spinning to eliminate any air bubbles. The elastomer was cured for seven days under atmospheric conditions. After curing, the elastomer thin films were removed from the substrates to produce free-standing films of similar dimensions to the composite samples. Gold electrodes were deposited onto the Sylgard 184. The samples were connected to the two-point probe set-up and I-V curves were obtained. Sylgard 184 is an insulating material. Curves contain many noise peaks that were absent in composite I-V plots. After smoothing, I-V plots for both surface and bulk measurements could be used to calculate conductance values (figures 9 and 10).

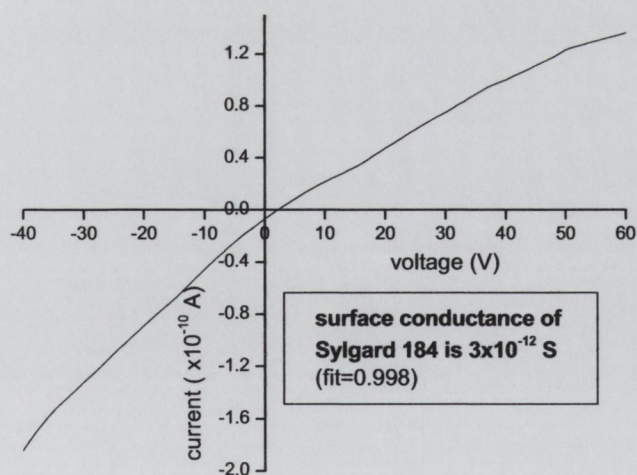


Figure 9: I-V plot obtained between two surface electrodes for a Sylgard 184 thin film sample. Prior to smoothing, the plot showed a lot of noise peaks.

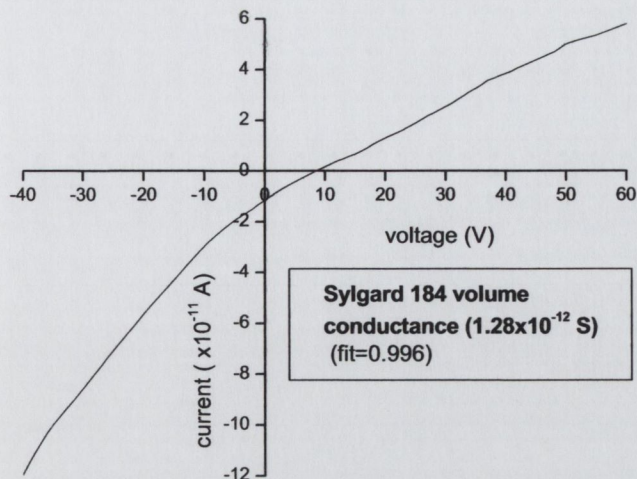


Figure 10: I-V plot obtained across the bulk of a Sylgard 184 thin film sample. Prior to smoothing the plot showed a lot of noise peaks.

As before, conductance values were converted to conductivity values. The average surface conductivity was calculated to be $(2.0 \pm 1.5) \times 10^{-12}$ S/□. This value is an average measured over three samples (figure 11). The average bulk conductivity was calculated to be $(4.1 \pm 4.7) \times 10^{-12}$ S/m. This value is also an average measured over three samples (figure 12). Again, deviations result from the error involved in measuring the thickness thin film and the separation of electrodes. This compares to a volume resistivity of 2×10^{15} Ω-cm (2×10^{-13} S/m) quoted by Dow Corning [3].

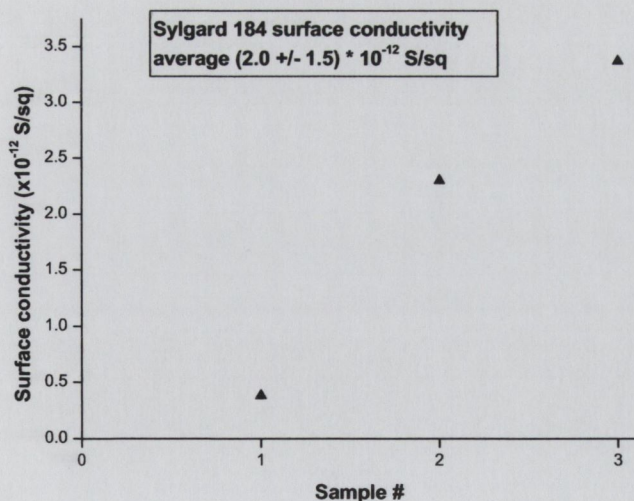


Figure 11: The average surface conductivity for a Sylgard 184 thin film was measured over three samples.

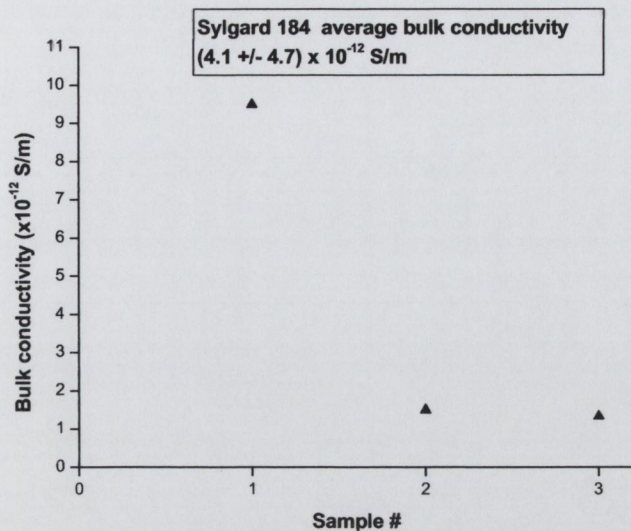


Figure 12: The average bulk conductivity for a Sylgard 184 thin film was measured over three samples.

Therefore, surface conductivity changes from $(2.0 \pm 1.5) \times 10^{-12} \text{ S}/\square$ to $(2.4 \pm 3.2) \times 10^{-6} \text{ S}/\square$. This corresponds to an increase of 10^6 . Bulk conductivity changes from $(4.1 \pm 4.7) \times 10^{-12} \text{ S/m}$ to $(4.4 \pm 4.7) \times 10^{-4} \text{ S/m}$. This corresponds to an increase of 10^8 . Although CNTs are entangled, the general direction of growth during CVD is upwards from the substrate surface. Therefore, we expect the bulk conductivity to be greater than the surface conductivity. However, the surface conductivity also increases by a significant amount indicating good CNT contact and entanglement in the plane of the substrate. If aligned CNTs had been used to reinforce the polymer, we would have expected good bulk conductivity but poor surface conductivity due to a lack of entanglement.

Our technique of composite synthesis can therefore be used to transform an insulating system into a conducting polymer [4]. Conductivity values for the films are well within the range required for electrostatic discharge applications. It should also be possible to increase conductivity values further still by using an alternative polymer matrix to Sylgard 184. For example, the electrical conductivity of nanotube-composite fibres was increased by one hundred times when the matrix poly(vinylalcohol) was replaced with the ionomer poly(ethyleneimine) [5]. This could push conductivity values into the region required for touch screen displays ($10^{-3} \text{ S}/\square$), flat panel devices ($10^{-2} \text{ S}/\square$) and possibly even electromagnetic interface shielding ($10^{-2} \text{ S}/\square$) [6].

7.4 Mechanical Reinforcement

Due to their large Young's modulus (0.1-1 TPa) and tensile strength (10-50 GPa), CNTs are expected to be excellent fillers for the mechanical reinforcement of polymer systems [7,8]. The mechanical reinforcement of our samples was quantified using a Perkin-Elmer dynamic mechanical analyser. A dynamic mechanical analyser (DMA) measures the force required to stretch a material and can therefore be used to calculate the Young's modulus. The Young's modulus (Y) is defined as the ratio of stress to strain (equation 6). It reflects the ease with which a material can be stretched and is often referred to as the modulus of elasticity. The observation that elongation is proportional to the force applied is known as Hooke's law.

$$Y = d\sigma / d\varepsilon \Big|_{\varepsilon \rightarrow 0} \quad \text{Equation 6.}$$

$$\sigma = \text{stress} = \text{force} / \text{area} (\text{N/m}^2)$$

$$\varepsilon = \text{strain} = \text{change in length} / \text{original length} (\text{no units})$$

The sample under investigation is held between two clamps and stretched at a uniform rate. A plot of force against elongation is obtained from the DMA. Where the cross-section area and original length of the sample is known, the force and elongation can be converted to stress and strain values respectively. The initial slope of a stress-strain plot reveals a value for Y . The shape of the plot depends on the material being tested. For all materials, initial deformation is elastic and stress is directly proportional to strain. In this region, the work produced by external forces is stored as elastic energy and can be recovered once the force is removed. As the applied force increases, deformation becomes permanent. Finally when the force is sufficiently large, the material fractures. The point of fracture depends on the strength of the material. Stress-strain plots can also be used to determine the toughness of a material. Toughness is defined as the amount of energy that a material can absorb before breaking. It can be calculated as the area underneath a stress-strain curve.

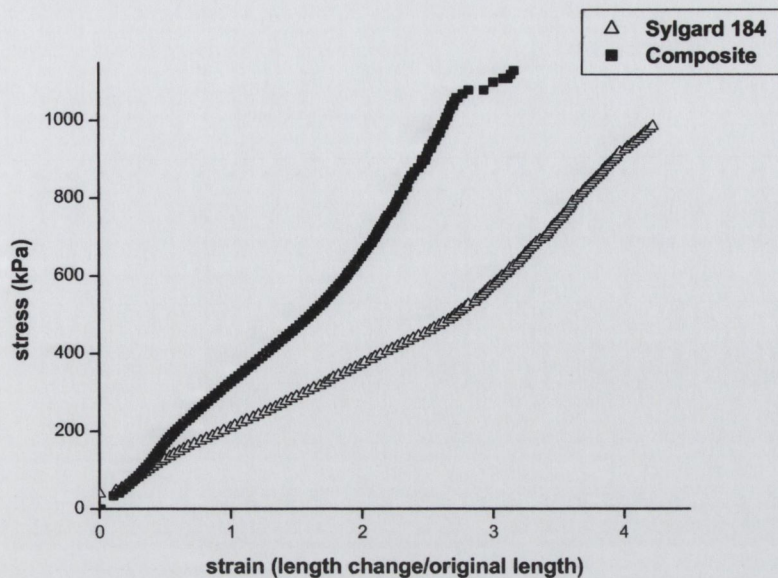


Figure 13: A comparison of σ - ϵ curves obtained for Sylgard 184 versus a composite. The Young's modulus is seen to increase as nanotubes are incorporated into the elastomer matrix. The increase shown here is from 188 kPa to 369 kPa.

Stress-strain curves were measured for a number of thin elastomer and composite strips. All measurements were made at room temperature for an applied force of 30mN/min. A comparison of stress-strain curves for Sylgard 184 films and composite films revealed that the incorporation of CNTs caused an increase in Young's modulus (figure 13). Average Y values were calculated to be 195 ± 43 kPa for the elastomer and 418 ± 83 kPa for the composite. Therefore, by adding CNTs to the elastomer system Y increases by a factor of 2.1 ± 0.9 [4]. Values were measured over an average of 13 polymer samples and 5 composite samples. Strips were approximately 2cm long, 2mm wide and 250 μ m thick. Hence, cross-section areas are of the order 10^{-7} m². Such a small cross-section area is difficult to measure accurately and even slight deviations from the actual value can result in an error in the Young's modulus calculation. Sample dimensions were measured using a travelling microscope. This gives a tighter distribution of thickness values than a digital micrometer. The width and thickness of each sample was measured a number of times for optimal accuracy. Y values were calculated using the mean cross-section area for each sample. Error bars for each Y value were calculated to reflect the spread of cross-section areas obtained for each individual sample (figure 14).

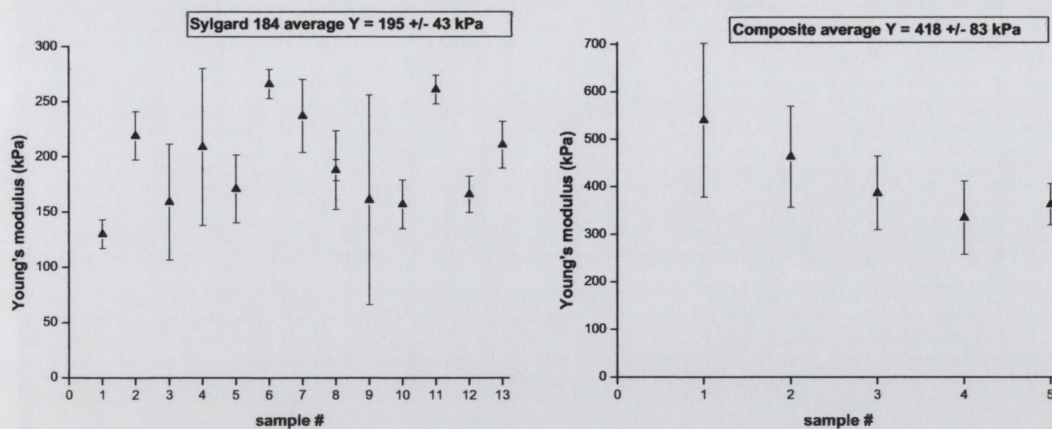


Figure 14: Young's modulus values were calculated for a number of samples to obtain an average. Error bars reflect fluctuations in cross-section area measurements.

Although the modulus shows a significant increase in the composite samples, we might expect greater reinforcement even for a very low percentage loading of CNTs as the polymer modulus itself is so low. The rule of mixtures relates the composite modulus, Y_C , to the volume fraction, V_f , of nanotubes (equation 7).

$$Y_C = (Y_{NT} - Y_P) V_f + Y_P \quad \text{Equation 7.}$$

Y_{NT} = nanotubes modulus
 Y_P = polymer modulus

This suggests that, taking a conservative value of $Y_{NT} = 100$ GPa, an increase in modulus by a factor of two should occur for a volume fraction of $V_f = 2 \times 10^{-6}$. The volume fraction in our system was calculated to be 0.41wt% (section 7.5). This means that the reinforcement is significantly lower than expected.

Stress-strain curves can also be used to calculate the elongation, toughness and strength of a sample. Elastomers are amorphous polymers with a low glass transition temperature. Therefore, they are soft and rubbery at room temperature. Stretching an elastomer induces order as molecules align in the pulling direction. On a molecular level, the polymer becomes ordered and eventually crystallises. Strain induced crystallisation is seen as an upturn in the shape of an elastomer stress-strain plot. Brittle materials lack this ability to re-arrange on a molecular level. Therefore, plots are linear. When the applied force is removed, entropy drives the polymer to return to the disordered state. The elastic limit of the polymer is the point at which permanent deformation occurs. Elastomers can deform

substantially before breaking. This causes them to have increased toughness. Adding CNTs inhibits the motion of the elastomer and makes it more resistant to elongation (figure 15). As a result the composite is more brittle. The composite toughness is therefore decreased and less energy can be absorbed by deformation before breaking (figure 16).

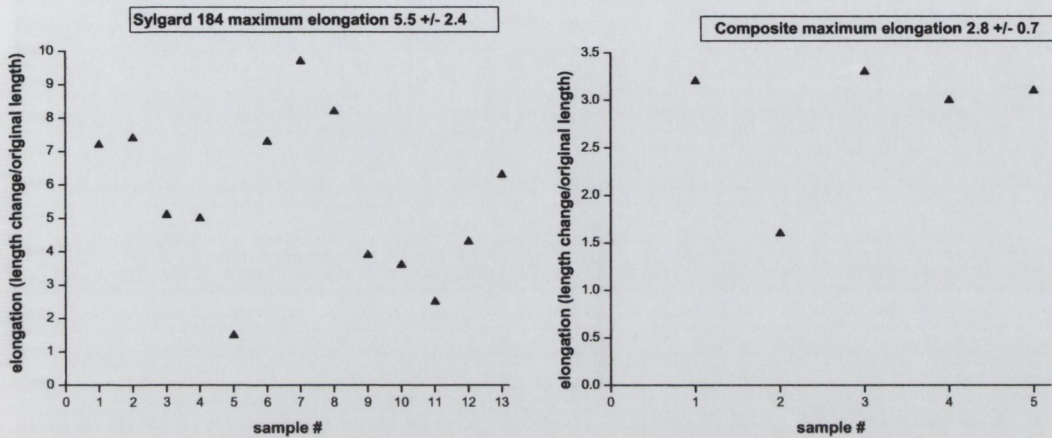


Figure 15: Maximum elongation at break measured from stress-strain plots.

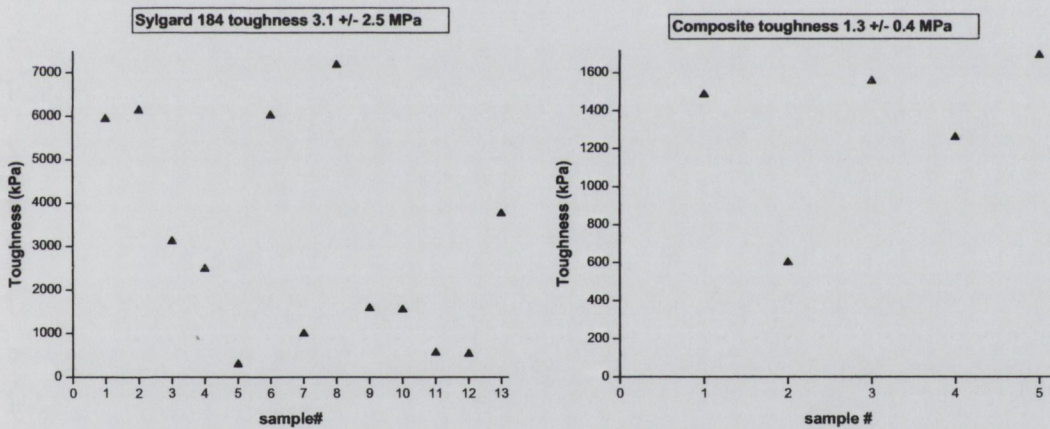


Figure 16: Toughness values are obtained from the integral of stress-strain plots.

CNTs are expected to induce strength [9]. We calculated average values of 1.3 ± 0.6 MPa for the elastomer and 844 ± 174 kPa for the composite. However, there is significant overlap in strength values for the composite and the elastomer. Many values for the elastomer strength lie close to 800kPa whereas many values for the composite lie above 900kPa (figure 17). The stress-strain plot shown in figure 12 illustrates a composite strength of 1,117 kPa and elastomer strength of 977 kPa. Therefore, our strength calculations are inconclusive.

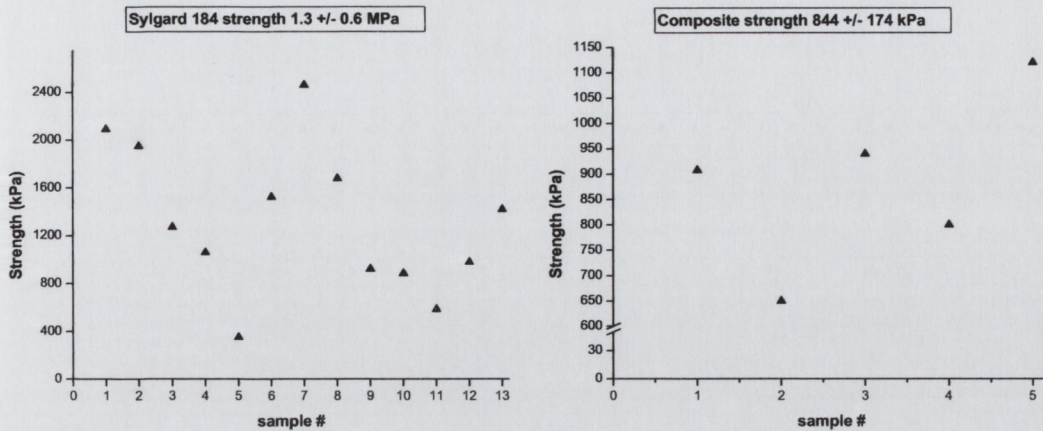


Figure 17: Strength values are obtained from the stress at sample fracture on stress-strain plots.

A bar chart of average composite and elastomer properties relative to each other was plotted (figure 18). This chart clearly indicates a Y increase for the composite. It shows a definite reduction in elongation and toughness and suggests a decrease in the strength of the composite with respect to the elastomer. The reduction in elongation and toughness are clear and expected. A reduction in strength however is not expected. We suggest that the low level of reinforcement is because full load transfer is not occurring at the polymer-CNT interface [10]. This may be due to the specific details of the van der Waals interaction between the silicone elastomer and the nanotubes. It is known that the extent of load transfer is dependent on the local polymer morphology at the polymer nanotube interface [5]. Load transfer is maximised when the interfacial polymer forms a crystalline shell around the nanotubes [11]. However when the interfacial polymer remains amorphous, load transfer can be very low. The nature of the polymer was investigated using differential scanning calorimetry.

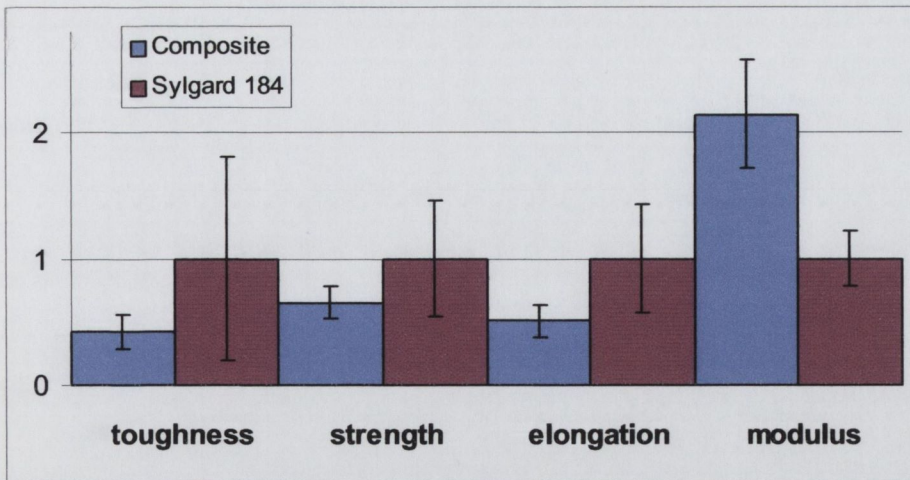


Figure 18: Elastomer properties are taken to be unity and relative values for the composite are adjusted accordingly. Error bars indicate the range of values obtained.

7.5 Differential Scanning Calorimetry

Differential scanning calorimetry (DSC) is used to monitor thermal transitions in a polymer. The polymer sample is placed in an aluminium pan and heated at a constant rate. There is no mass change involved with the heating only a change in enthalpy of the polymer. An identical, but empty, reference pan is simultaneously heated at the same rate. The pan containing the polymer sample will require more heat to keep the temperature increasing at the same rate. The difference in heat flow to the pans is plotted against temperature. Peaks and dips in the plot correspond to thermal transitions (figure 19).

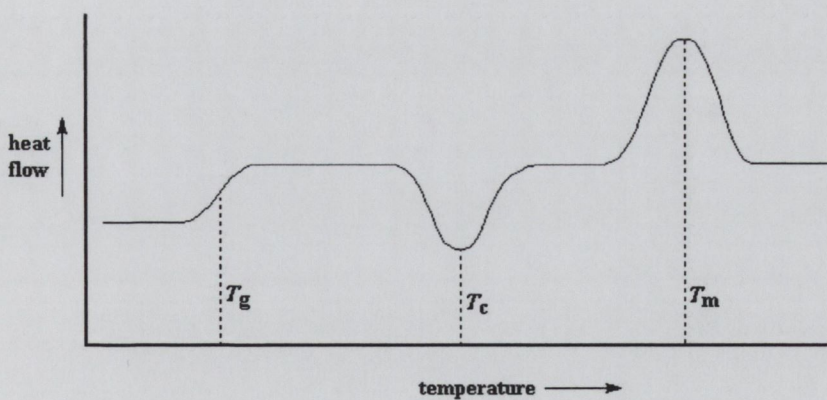


Figure 19: A typical DSC plot of heat flow against temperature. Peaks correspond to the glass transition and melt peak. The dip corresponds to the crystallisation temperature.

The first transition observed is a second order transition called the glass transition temperature (T_g). This is an endothermic reaction which results in an increase in the motion of the polymer molecules. They evolve from a glassy state into a rubbery state. As the temperature continues to increase the polymer molecules are in motion. When they reach a certain temperature, they have enough energy to adopt ordered arrangements. This is the crystallisation temperature (T_c) which is an exothermic peak. This corresponds to a first order transition, as there is a phase change involved. The area of the peak allows us to calculate the latent heat of crystallisation and the percentage crystallinity of the polymer.

As the polymer is heated further to the melt temperature (T_m), it undergoes another phase change. Melting is an endothermic first order transition. Polymer chains lose their crystallinity and are free to move about in random motion. The latent heat of melting can be calculated from the area of this peak.

Amorphous polymers do not display either a crystallisation or a melt peak. They are disordered systems and do not become crystalline on heating.

7.5.1 DSC Analysis

DSC was used to determine the effect of the nanotubes on the polymer morphology in a composite. The DSC scan for the Sylgard 184 revealed it to be a completely amorphous material with a glass transition temperature at -122.6°C (figure 20). This transition temperature is similar to values quoted by others [12]. No crystallinity or melt peaks were observed. The glass transition of the composite showed a negligible shift to -123.8°C , with crystallinity and melt peaks also absent. This shows that the presence of CNTs has not induced any crystallinity or morphology changes within the polymer. This means that the interfacial polymer is amorphous which is consistent with poor load transfer, which explains the lack of strength enhancement as CNTs are incorporated into the polymer.

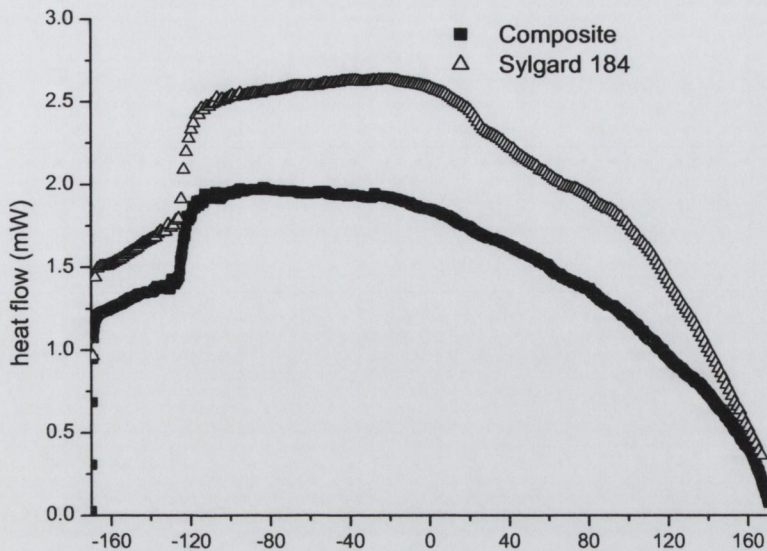


Figure 20: DSC curves showing the amorphous nature of both the silicone elastomer and the NT composite. The glass transition temperatures are -122.6°C ($\Delta C_p = 0.257 \text{ J/gK}$) and -123.8°C ($\Delta C_p = 0.281 \text{ J/gK}$) respectively.

In general interfacial stress transfer can be improved by functionalisation of the nanotubes [13]. It may however be easier to improve load transfer by exchanging the matrix for a more crystalline polymer.

7.6 Thermal Gravimetric Analysis

Thermal gravimetric analysis (TGA) of Sylgard 184 shows the elastomer to be stable up to 300°C . As the temperature is increased further the polymer begins to decompose and weight loss occurs. The weight finally stabilises again at 537°C , where 65wt% remains. This agrees well with previously published TGA data for Sylgard [14]. We attribute the remaining mass to the formation of silicon dioxide, a product of the silicone ($-\text{Si-O}-$) polymer backbone. This takes the form of a white chalky powder which remains in the aluminium pan after heating.

The TGA curve of the elastomer was compared with that of a composite made by embedding carbon nanotubes in Sylgard 184 (figure 21). The composite is also stable up to 300°C . However, a greater weight loss occurs above this temperature. The weight stabilises at 540°C where 46% of the composite remains. Carbon nanotube are known to have a high thermal conductivity [15]. Therefore, it is possible that they provide a

mechanism for more uniform heat distribution through the (insulating) silicone. This could facilitate greater decomposition of the elastomer.

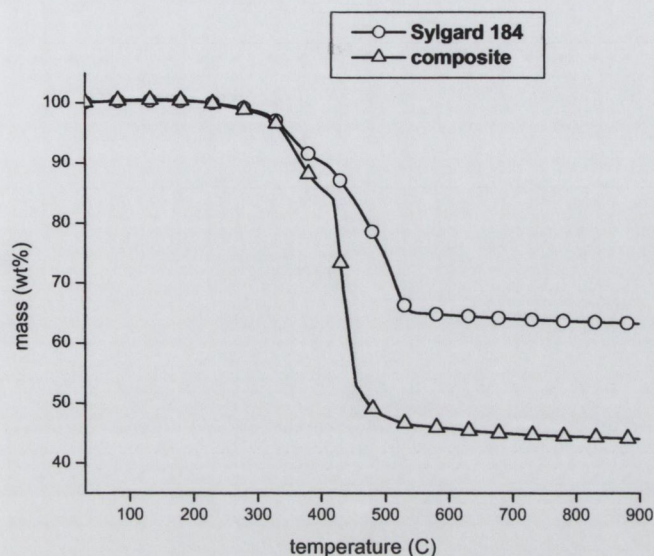


Figure 21: TGA plot of Sylgard 184 compared with a nanotube-containing composite.

Taking the derivative of the TGA plots allows decomposition peaks to be seen more clearly. In both the composite and Sylgard 184 derivative TGA plots, there are two main decomposition peaks. The position of the first peak is the same for both materials and lies at 352°C for the elastomer and 354°C for the composite. The position of the second peak shifts from 510°C for the silicone to 434°C for the composite (figure 22). This decomposition peak is considerably sharper for the composite. Again the high thermal conductivity of nanotubes allows heat to be dispersed more efficiently within the composite system. This facilitates decomposition over a more narrow temperature range.

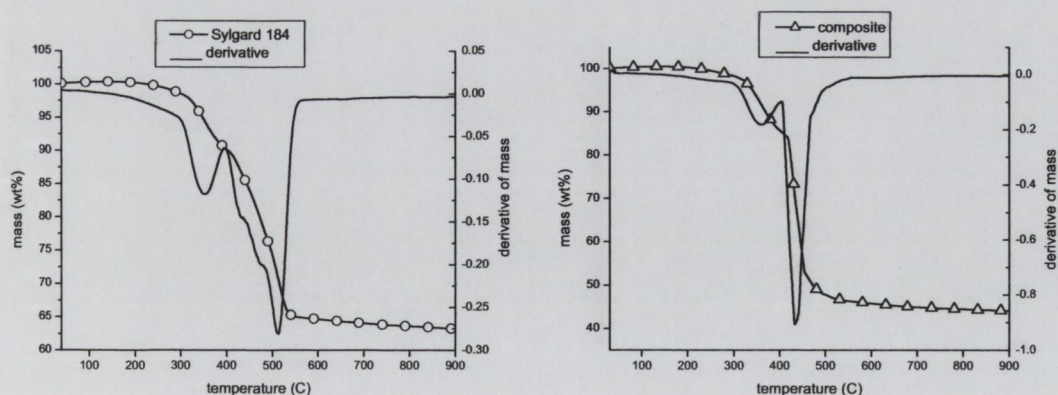


Figure 22: A TGA plot of Sylgard 184 shown with its derivative, and a TGA plot of the composite also shown with its derivative.

By subtracting the derivative curves, $(dm/dT)_{\text{composite}} - (dm/dT)_{\text{polymer}}$, we can clearly see peaks which are characteristic of the composite. Inverting this plot shows decomposition as peaks. This can then be plotted on a log scale to highlight small peaks which otherwise are not obvious (figure 23).

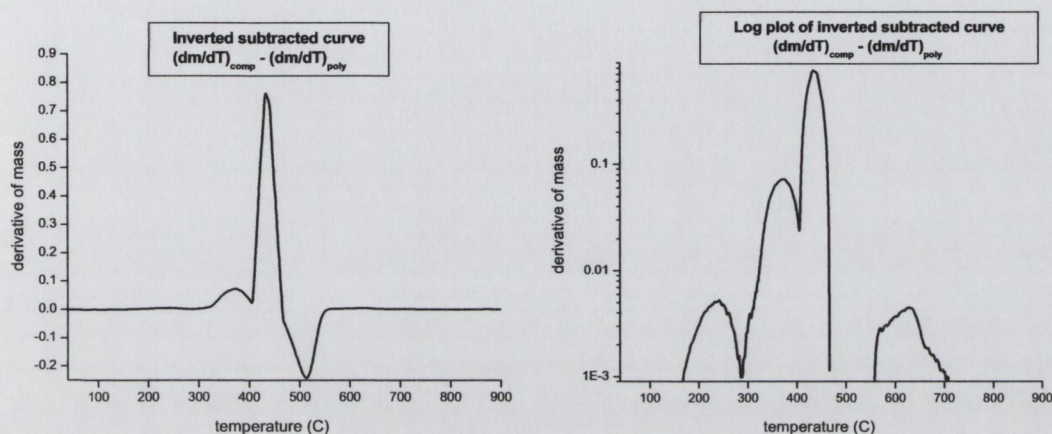


Figure 23: An inverted plot of the curve obtained from subtracting the elastomer derivative peaks from the composite derivative peaks. The second graph shows the same data plotted on a log scale for clarity.

Composite decomposition peaks can be compared to the derivative TGA peaks for a carbon nanotube sample. Carbon nanotubes were grown from a silicon oxide wafer using a poly(styrene-vinylferrocene) catalyst and the CVD conditions described earlier (section 5.4). A small substrate ($\sim 5\text{mm}^2$) was placed in the TGA. Only a very small weight drop was observed (0.1wt%). This is due to the decomposition of nanotubes. The remaining weight is the mass of the substrate. This can therefore be subtracted from the TGA curve. The resulting plot has many noise peaks due to the small mass of the CNT sample. However, after differentiating two distinct peaks emerge. One at 322°C and the second at 585°C (figure 24).

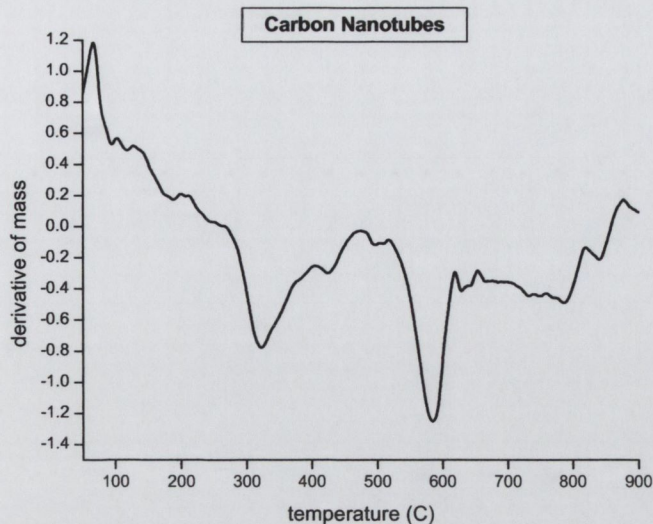


Figure 24: Derivative of a TGA plot obtained for carbon nanotubes.

The peak at 585°C is outside the range of Sylgard 184 decomposition. If we look at the curve obtained by subtracting the elastomer derivative peaks from the composite derivative peaks on a log scale, we can see a peak from 555 °C -709 °C (figure 23). We can attribute this to carbon nanotube decomposition. Integration of this peak allows us to estimate the nanotube content of the composites to be 0.41 wt%.

7.7 Conclusion

We have shown that by incorporating CNTs (~0.4wt%) into a silicone elastomer matrix the insulating system can be transformed into a conducting polymer. The surface conductivity increased by six orders of magnitude to reach $(2.4 \pm 3.2) \times 10^{-6}$ S/□. The bulk conductivity increased by eight orders of magnitude to reach $(4.4 \pm 4.7) \times 10^{-4}$ S/m. The mechanical enhancement provided by the CNTs was not quite so impressive. The Young's modulus increased from 195 ± 43 kPa to 418 ± 83 kPa. This corresponds to an increase by a factor of 2.1 ± 0.9 . Elongation and hence toughness decreased for the composite as expected. Surprisingly, we also found that the presence of CNTs provided no strength enhancement. DSC analysis showed the polymer at the CNT interface to be amorphous. This is consistent with poor load transfer. Due to their large Young's modulus and tensile strength, CNTs are expected to be the ultimate filler material for a polymer system [16]. However, to date no researchers have achieved the level of mechanical reinforcement expected.

7.8 References

- [1] HD Young, RA Freedman, University Physics, 9th Ed., (Addison Wesley), 1996
- [2] Keithley Applications Note Series, No. 2615
- [3] Data sheet, 'Information about high technology silicon materials', Dow Corning.
- [4] E Lahiff, R Leahy, JN Coleman, WJ Blau, Carbon, 44(8), 1525, 2006.
- [5] E Munoz, DS Suh, S Collins, M Selvidge, AB Dalton, BG Kim, JM Razal, G Ussery et al, Adv. Mater., 17(8), 1064, 2005.
- [6] M Kaempgen, GS Duesberg, S Roth, Appl. Surf. Sci., 252, 425, 2005
- [7] JP Salvetat, JM Bonard, NH Thomson, AJ Kulik, L Forro, W Benoit, L Zuppiroli, Appl. Phys. A, 69, 255, 1999
- [8] B Vigolo, A Penicaud, C Coulon, C Sauder, R Pailler, Science, 290, 1331, 2000
- [9] AB Dalton, S Collins, E Munoz, JM Razal, VH Ebron, JP Ferraris, JN Coleman, BG Kim, RH Baughman, Nature, 423, 703, 2003
- [10] PM Ajayan, L Schadler, C Giannaris, A Rubio, Adv. Mater., 12 (10), 750, 2000
- [11] M Cadek, JN Coleman, V Barron, K Hedicke, WJ Blau, Appl. Phys. Lett., 81 (27), 5123, 2002
- [12] WWY Chow, KF Lei, G Shi, WJ Li, Q Huang, Smart Mater. Struct., 15, S112, 2006
- [13] R Blake, YK Gun'ko, J Coleman, M Cadek, A Fonseca, JB Nagy, WJ Blau, J. Am. Chem. Soc., 126, 10226, 2004.
- [14] Dow Corning, Form No. 75-1021A-01, Highly Transparent Silicone Materials.
- [15] P Kim, L Shi, A Majumdar, PL McEuen, Phys. Rev. Lett., 87(21), 215502-1, 2001
- [16] L Forro, Europhys. News, 32(3), 2001

Chapter 8: Conclusions and Future Work

8.1 Conclusions

In this thesis a novel method of carbon nanotube composite production was introduced. Using this technique carbon nanotubes are grown in ordered arrays onto substrates. The tubes can then be directly incorporated from substrates into composites by spin coating a curable polymer onto the tubes. After curing the composite can be peeled away from the substrate to produce a freestanding thin film. This provides a method of controlling the position of carbon nanotubes, and hence conduction channels, through a polymer matrix [1].

Carbon nanotubes are tiny cylinders of rolled up graphene sheets. The bonding of carbon molecules in the tube walls is therefore analogous to that of in-plane graphite. This provides tubes with exceptional electric conductivity and mechanical strength. Therefore, we can envisage a wide range of applications for nanotubes including quantum wires, transistors and field emitters [2-5]. Much attention has been given to the potential of carbon nanotubes. In 2004 alone 49 papers were published in the prestigious journal *Science* in connection with carbon nanotubes. The US Patent Office has 1,248 patents relating to carbon nanotubes listed in their on-line database.

The commercialisation of carbon nanotubes is limited by a number of factors. The first one is the difficulty associated with large-scale production. This drives up the cost of nanotubes making them unsuitable for many applications. The cost can be as high as \$2,000/g for superpurified HiPco[®] tubes from Carbon Nanotechnologies Incorporated (CNI). The cost reduces to \$375/g for as-produced unpurified tubes from CNI. As prepared arc-discharge tubes are available at the lower cost of \$60/g from Carbolex. In November 2005 Bayer announced that they could produce large volumes of low cost carbon nanotubes using a new manufacturing process. Tubes are reportedly >99% pure with a mean diameter of 50nm. They plan to market the product under the name Baytubes[®]. Lowering the cost of production increases the viability of CNTs.

Another problem with the production of CNTs is that many synthesis techniques result in a fluctuation in the quality of tubes produced. While batches of nanotubes may have similar properties (such as diameter and crystallinity) they are never identical. In chapter 2 we

discussed how as-produced nanotubes are a mixture of semiconducting and conducting tubes. For electronic applications such as quantum wires and transistors this is a serious issue, as conductivity cannot accurately be predicted.

In this thesis we focus on carbon nanotubes as a filler material for polymer systems. In 1977 intrinsically conducting polymers (ICP) were discovered [6]. ICPs generated much interest as they suggested the possibility of flexible electronics which could be processed with the ease of a polymer. However, most ICPs are unstable under atmospheric conditions. Therefore, their potential has not yet been fully realised. Another way to introduce conductivity to a polymer system is to add a conductive filler material. While introducing conductivity to an insulating matrix, filler particles also mechanically reinforce the system. Ideally the filler should be a low-density material which can achieve percolation at low loading levels. Adding large amounts of filler particles to a polymer affects its surface roughness, viscosity and processability. To achieve percolation at low loading levels a filler material must be highly conductive while simultaneously having a large aspect ratio. Carbon nanotubes satisfy both these requirements. Small amounts of CNTs can be added to a polymer to significantly increase its conductivity without noticeably altering the viscosity.

The first carbon nanotube-polymer composite was made by Ajayan et al in 1994 [7]. Nanotubes were dispersed in an epoxy resin by mechanical mixing. Despite continued mixing, they noticed that nanotubes aggregated together resulting in a composite with non-uniform consistency. Nanotubes always have a tendency to bundle together. This is due to van der Waal forces between tubes. Approaches to address this issue, such as sonication and treatment with a surfactant, can be time consuming. Sonication can also damage the nanotube structure. In this thesis we introduce a new method of dispersing nanotubes within a polymer matrix. By incorporating CVD grown nanotubes directly from a substrate into a polymer, we eliminate the need for a dispersion step during composite synthesis. By precise patterning of catalyst particles onto the substrate prior to CVD we simultaneously have a mechanism of pre-determining the position of nanotubes within a polymer matrix.

During this thesis we also demonstrated control over the morphology of nanotubes produced by CVD. We observed that the diameter of tubes is a function of temperature. Using the catalyst poly(styrene-vinylferrocene), the diameter of tubes grown at 700°C was 20nm compared to 70nm for tubes grown at 800°C. We also noticed that the homogeneity

of carbon nanotube growth is sensitive to the composition of the catalyst used. Using poly(styrene-vinylferrocene) we obtained more uniform nanotube growth than that obtained using the homopolymer poly(vinylferrocene). We succeeded in growing clean nanotubes with very little amorphous carbon production. We found amorphous carbon deposition to occur for a high partial pressure of acetylene during CVD. We also noticed that for longer deposition times (30 minutes) a layer of amorphous carbon begins to form over nanotubes grown from the substrate. The fact that we can produce clean nanotubes eliminates the need for post-production purification. Purification is often necessary especially for tubes grown by arc-discharge. It can be a lengthy process during which quantities of tubes are lost. That we can eliminate the need for this processing step is advantageous for commercial applications. Therefore by monitoring the temperature, catalyst, acetylene partial pressure and deposition time we can control, to an extent, the morphology of nanotubes produced.

Another important property is the density of nanotubes grown onto substrates, and hence subsequently embedded in polymer systems. Density can be very simply controlled by varying the concentration of catalyst solution patterned onto substrates prior to CVD. Control over density is important if nanotubes are to be used in applications such as field emission. Also by manipulating the nanotube density it should be possible to precisely determine the onset of percolation in carbon nanotube-polymer composites.

We were successfully able to grow a variety of nanotube array geometries. Line, dot and grid patterns were all demonstrated. We were limited in that we were unable to produce these arrays over large areas. Patterning was done using soft lithography [8]. A drop of catalyst solution was deposited onto substrates and a pre-patterned elastomer was then brought into contact with the substrate. Using an index finger, stamps were gently pressed against substrate to ensure good contact. This is rather a crude mechanism of applying pressure and it is certain that the pressure applied is not uniform across the entire stamp. This is one possible reason for the difficulties encountered with large-scale array production. Others have addressed this issue and developed a technique known as wave-printing whereby a rigid back plate is applied to the elastomer. The back plate is connected to a pressure supply which allows controlled contact between the stamp and substrate [9].

Carbon nanotube composites made by our technique were tested to quantify the level of reinforcement provided by the embedded tubes [10]. Entangled CNT films were

incorporated into elastomer thin films. We measured a significant increase in conductivity. The surface conductivity increased by 10^6 and the volume conductivity increased by 10^8 . This pushes conductivity values for the composite films to within the range required for electrostatic discharge applications. The mechanical reinforcement of the polymer was less impressive. Average values for the Young's modulus were calculated to be 195 ± 43 kPa for the elastomer and 418 ± 83 kPa for the composite. CNTs are expected to induce strength. We calculated average values of 1.3 ± 0.6 MPa for the strength of the elastomer and 844 ± 174 kPa for the composite. We attribute the poor mechanical enhancement to a weak polymer-nanotube interface.

8.2 Future Work

It should be possible to increase conductivity values further still by using an alternative polymer matrix to Sylgard 184. For example, the electrical conductivity of nanotube based composite fibres was increased by one hundred times when the matrix poly(vinylalcohol) was replaced with the ionomer poly(ethyleneimine) [11]. Conductivity values could also be increased by using more crystalline, or perhaps single-walled, nanotubes. This could push conductivity values into the region required for touch screen displays (10^{-3} S/ \square), flat panel devices (10^{-2} S/ \square) and possibly even electromagnetic interface shielding (10^{-2} S/ \square).

We suggest that the mechanical properties of the composite could be improved by replacing the amorphous polymer matrix with a semi-crystalline polymer. It has been reported that nanotubes nucleate crystallinity and that stress transfer can occur through this mechanism [12]. Functionalisation of the tubes could also be an issue to explore for mechanical enhancement. This would improve stress transfer from the matrix to the nanotubes. The level of functionalisation must be carefully controlled to avoid disruption of electrical conductivity along graphitic sidewalls of the nanotubes.

It would also be interesting to do a systematic study on the effect which nanotube morphology has on the properties of the composite. Tubes of increasing diameter could be studied. The effects of nanotube density could also be studied to determine the percolation threshold. It would also be interesting to study composites, made by this technique but, reinforced using single- rather than multi-walled tubes. These values could perhaps be compared with composites made using an impure nanotube sample containing a certain level of amorphous carbon.

Optimising the various issues arising from this thesis should result in a controlled, economical and convenient method of carbon nanotube-polymer composite production. Composites would be useful in applications such as flexible electronics where it is desirable that the position of conduction channels be controlled.

8.3 References

- [1] E Lahiff, CY Ryu, S Curran, AI Minett, WJ Blau, PM Ajayan, *Nano Letters*, 3, (10), 1333, 2003
- [2] SJ Tans, MH Devoret, H Dai, A Thess, RE Smalley, , LJ Geerligs, C Dekker *Nature*, 386, 474, 1997
- [3] SJ Tans, ARM Verschueren, C Dekker, *Nature*, 393, 49, 1998
- [4] WB Choi, DS Chung, JH Kang, HY Kim, YW Jin et al, *Appl. Phys. Lett.*, 75(20), 3129, 1999
- [5] S Fan, MG Chapline, NR Franklin, TW Tomblor, AM Cassell, H Dai, *Science*, 283, 512, 1999
- [6] H. Shirakawa, E.J. Lewis, A.G. MacDiarmid, C.K. Chiang, A.J. Heeger, *J. Chem. Soc. Chem. Commun.* 578, 1977.
- [7] PM Ajayan, O Stephan, C Colliex, D Trauth, *Science*, 265, 1212, 1994.
- [8] Y Xia, GM Whitesides, *Angew. Chem. Int. Ed.*, 37, 550, 1998.
- [9] MMJ Decre, R Schneider, D Burdinski, J Schellekens, M Saalmink et al, *Mat. Res. Soc. Symp. Proc.*, Vol. EXS-2, M4.9.1
- [10] E Lahiff, R Leahy, JN Coleman, WJ Blau, *Carbon*, 44(8), 1525, 2006.
- [11] Munoz E, Suh DS, Collins S, Selvidge M, Dalton AB, Kim BG, Razal JM, Ussery G, Rinzler AG, Martinez MT, Baughman RH, *Adv. Mater.*, 17(8), 1064, 2005
- [12] M Cadek, JN Coleman, V Barron, K Hedicke, WJ Blau, *Appl. Phys. Lett.*, 81(27), 5123, 2002.

Appendix A: Euler's Theorem

Euler's theorem relates the number of vertices (v), edges (e) and faces (f) of a polyhedron, according to equation 1.

$$v - e + f = 2 \quad \text{equation 1.}$$

In this case, carbon atoms represent the vertices and the edges are the covalent bonds. The number of faces (f) is the sum of the pentagons (p) and hexagons ($h = f - p$), which constitute the fullerene structure.

To calculate the number of pentagons:

There are five edges on a pentagon and six on a hexagon. Each edge belongs to two faces,
 $\Rightarrow 2e = 5p + 6(f - p)$

Also, three adjacent faces share each trivalent carbon,
 $\Rightarrow 3v = 5p + 6(f - p)$.

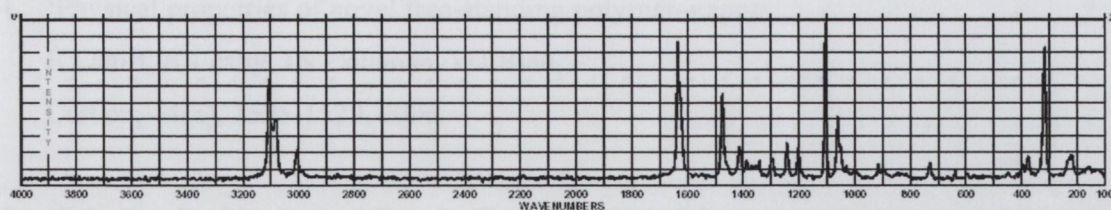
Substituting these values for e and v into equation 1 gives,

$$\begin{aligned} & \frac{1}{3} \{5p + 6(f - p)\} - \frac{1}{2} \{5p + 6(f - p)\} + f = 2 \\ \Rightarrow & 10p + 12(f - p) - 15p - 18(f - p) + 6f = 12 \\ \Rightarrow & \mathbf{p = 12} \end{aligned}$$

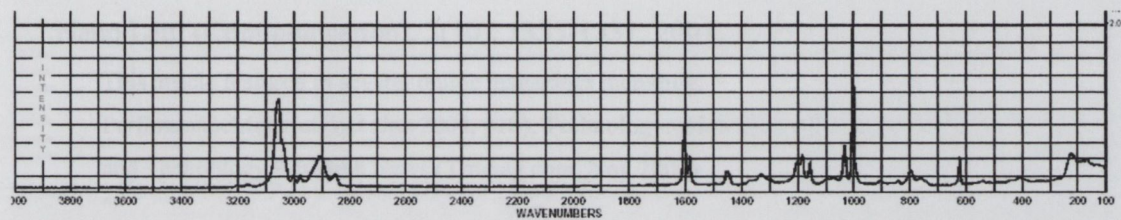
This value for p is independent of the number of hexagonal faces. Therefore all defect-less fullerenes (including carbon nanotubes) must both contain exactly 12 pentagons.

Appendix B: Reference Raman Spectra

Vinylferrocene (Aldrich)



Polystyrene (Aldrich)



1. "Controlling the Position and Morphology of Nanotubes"

F. Lahti & Leidy, *AI Mater. W. Blau*,

AIIP Conference Proceedings Vol. 734(1) 548-549, 2004

4. "Controlling the Position and Morphology of Nanotubes"

E. Lahti, *AI Mater. S. Carna, GY Ryo, WJ Blau, PM Ajayan*

Mat. Res. Soc. Symp. Proc., Vol. 782, A3.11.1, 2003

5. "Manipulation and Direction of Carbon Nanotubes"

manipulation and direction of carbon nanotubes

E. Lahti, *AI Mater. WJ Blau*,

Int. Conf. Synth. Met. Proc., 2004 (ISBN: 1741280613)

6. "Controlled Growth of Arrays of Straight and Branched Carbon Nanotubes"

R.W. Leidy, E. Lahti, A.J. Minett, W.J. Blau

SPIE Proc. Vol. 5824, Opto-Infrared 2005: Nanotechnology

7. "Efficient Charge Transport in Organic Photovoltaic Devices"

Carbon Nanotube Composites

G. Wallace, P. Fournier, C. McNeill, P. Demoor, E. Lahti, A.

Coleman, W. Blau,

Int. Conf. Synth. Met. Proc., 2004 (ISBN: 1741280613)